MECHANICAL CHARACTERIZATION AND CONSTITUTIVE MODELING OF RATE-DEPENDENT VISCOELASTIC BRAIN TISSUE UNDER HIGH RATE LOADINGS

A Dissertation
Submitted to the Graduate Faculty
of the
North Dakota State University
of Agriculture and Applied Science

By

Mohammad Hosseini Farid

In Partial Fulfillment of the Requirements
for the Degree of
DOCTOR OF PHILOSOPHY

Major Department:
Mechanical Engineering

May 2019

Fargo, North Dakota

North Dakota State University
Graduate School

Title

Mechanical Characterization and Constitutive Modeling of Rate-Dependent Viscoelastic Brain Tissue Under High Rate Loadings

By

Mohammad Hosseini Farid

The Supervisory Committee certifies that this ***disquisition*** complies with North Dakota State University's regulations and meets the accepted standards for the degree of

DOCTOR OF PHILOSOPHY

SUPERVISORY COMMITTEE:

Dr. Ghodrat Karami
Chair

Dr. Mariusz Ziejewski

Dr. Chad Ulven

Dr. Ravi Kiran Yellavajalla

Dr. Kambiz Farahmand

Approved:

6/10/2019
Date

Dr. Alan R. Kallmeyer
Department Chair

ABSTRACT

In this dissertation, theoretical, computational, and experimental methodologies are introduced to determine the rate-dependent material properties of the brain tissue. Experiments have shown that the brain tissue is significantly rate-dependent. To examine the range of strain rates at which trauma might happen, a validated finite element (FE) human head model was initially employed to examine the biomechanics and dynamic behavior of the head and brain under impact and blast loads. The strain rates to cause traumatic brain injury (TBI) were found to be in the range of 36 to 241 s^{-1}, under these types of loadings. These findings provided a good estimation prior to exploring the required experiments for characterizing the brain tissue.

The brain samples were tested by employing unconfined compression tests at three different deformation rates of 10 (n= 10 brain samples), 100 (n=8), and 1000 mm/sec (n=12). It was found that the tissue exhibited a significant rate-dependent behavior with various compression rates. Two different material characterization approaches were proposed to evaluate the rate-dependent mechanical responses of the brain. In the first approach, based on the parallel rheological framework, a single-phase viscoelastic model which captures the key aspects of the rate-dependency in large strain behavior was introduced. The extracted material parameters showed an excellent constitutive representation of tissue response in comparison with the experimental test results (R^2=0.999). The obtained material parameters were employed in the FE simulations of the brain tissue and successfully verified by the experimental results. In the second approach, the brain tissue is modeled as a biphasic continuum, consisting of a compressible solid matrix fully saturated with an incompressible interstitial fluid. The governing equations based on conservation of mass and momentum are used to describe the solid-fluid interactions. This

viscoelastic biphasic model can effectively estimate the rate-dependent tissue deformations, the hydrostatic pressure as well as fluid diffusion through the tissue.

Although both single-phasic, as well as bi-phasic models, can successfully capture the key aspects of the rate-dependency in large strain deformation, it was shown the biphasic model can demystify more phenomenological behavior of this tissue that could not be perceived with yet established, single-phasic approaches.

ACKNOWLEDGEMENTS

Foremost, I express sincere gratitude to my advisor, Dr. Ghodrat Karami, for his guidance, understanding, motivation, and immense knowledge, and most importantly, for his sincere friendship and continuous support during my graduate studies at North Dakota State University.

Special thanks go to my committee member Dr. Mariusz Ziejewski for his guidance in research and friendship throughout my PhD program. I want to thank my committee member Dr. Chad Ulven, for his guidance and support in my research. I am also grateful to Dr. Kambiz Farahmand from the Department of Industrial and Manufacturing Engineering and Dr. Ravi Kiran Yellavajalla from the Department of Civil and Environmental Engineering for agreeing to serve as a committee member.

Special thanks to the Department of Animal Science Department at North Dakota State University for providing the animal brain tissues. I also thank Dr. Ashkan Eslaminejad, and Mohammadreza Ramzanpour for their friendship and their technical assistance in my research.

Last but not the least, I gratefully thank my wife, Maryam, for her continuous support, her patience, her tolerance, and for allowing me the opportunity to pursue my study and finish my research, and I thank my parents for their spiritual support.

DEDICATION

To my Parents

To my wife

To my children

Thank you for your unconditional love and encouragement.

TABLE OF CONTENTS

LIST OF TABLES

LIST OF FIGURES

LIST OF ABBREVIATIONS

FE.....Finite Element.

TBI.....Traumatic Brain Injury.

DAI.....Diffuse Axonal Injury.

MRI.....Magnetic Resonance Imaging.

CT.....Computed Tomography.

CSF.....Cerebrospinal Fluid.

ACH.....Advanced Combat Helmet.

TNT.....Trinitrotoluol.

HE.....High Explosive.

EOS.....Equation of State.

JWL.....Jones–Wilkins–Lee.

ICP.....Intracranial Pressure.

Max.....Maximum.

NFL.....National Football League.

FEM.....Finite Element Method.

PBS.....Phosphate-Buffered Saline.

SD.....Standard Deviation.

ANOVA.....Analysis of Variance.

PRF.....Parallel Rheological Framework.

N.A.....Not Applicable.

Err.....Error.

BG.....Basal Ganglia.

C.....Cortex.

CC.....Corpus Callosum.

CR .....Corona Radiata.

CHAPTER 1. INTRODUCTION

1.1. Motivation

Intracranial head organs have been known to be the most sensitive organs involved in life-threatening injuries caused by impact incidents and blast waves [1, 2]. It was shown that intracranial brain deformation induced by severe rotations of the skull will result in rapid angular accelerations and shear strains which may lead to TBI [3]. Most TBIs are caused from falls, traffic, or sport accidents. They can, however, also occur from blunt impacts leading into an acute subdural hematoma, diffuse axonal injury (DAI), death and other serious disabilities around the world [4-6]. Due to the complex mechanical and physical reactions of the head and brain under impact and explosion waves, the mechanism of TBI is not well understood [7].

To study in vivo intracranial behavior under TBI conditions, FE models have been introduced to predict the brain deformation for different applied loads [4, 8-14]. FE simulations provide a convincing framework for determining biomechanical responses of the head exposed to those high rated loads [15]. These developed numerical models predict brain deformation for different applied loads and study the intracranial organs behavior under TBI conditions [5, 6, 8, 9, 13]. In these analyses, while creating a computational model containing detailed anatomical geometries of the human head is necessary, it is also highly important to employ accurate material properties for the intracranial organs. The biofidelity of such computational simulations is strictly related on the accuracy of the material properties used to model these tissues. This is essential in understanding the mechanisms of the brain injury, and is also helpful in promoting the surgical instruments and procedures, as well as drug and oxygen transport in the brain [16].

A precise prediction of nonlinear behavior of human brain tissue under arbitrary load-boundary conditions paves the way to foresee the performance of such complex organ in injury,

health and disease applications. On this subject, a rigorous mechanical characterization of this material is the base for biomechanical studies of the tissue, such as traumatic brain injury [17-23], neurosurgery [24, 25], etiology of disease, and therapeutic drug delivery to the brain [26-30]. The extreme scale of potential applications reveals the reason why brain mechanics has become a particularly important subject and has seen advances over the last few decades [21, 31-33].

1.2. Background

For over a half century, several experimental and theoretical studies were done to assess the biomechanical response of the brain [34-43]. Like other soft biological materials, it was found that the rheological properties of brain as the inhomogeneous, anisotropic and age-dependent tissue is related to strain, loading rate, time, temperature, as well as regions and directions [44-50]. Ideally, constitutive model should take all the above-mentioned parameters into account. However, due to experimental and theoretical limitations the available models mostly consider one or few variables [25, 51-53].

Typically, the soft biological materials, such as those in the brain, present complex mechanical response, characterized by large strains, rate sensitivity and load history[54, 55]. Recent studies involving in vitro experiments have provided a comprehensive observation of brain behavior under different loading modes such uniaxial tension [56-58], compression [59-62], shear [38, 63-66], relaxation [61], and under cyclic loads [40]. In macroscopic view, the brain is an extremely soft solid and its mechanical behavior is greatly influenced by the fluid phase [14]. However, this tissue has been mostly treated as an isotropic, single solid-phase and mainly characterized into linear elastic [67], linear viscoelastic [36], hyperelastic [68], and hyper-viscoelastic [62, 69] material modeling.

Most common models for the brain tissue which have been proposed in the literature can be generally divided into: time-dependent and time-independent forms [70]. Linear elastic is the simplest time-independent model which is limited to small strain applications as low as 0.1% [71]. With an elastic modulus of 1~675 kPa, the brain tissue is known as the softest among all of the biological tissues [63, 67, 72-74]. It has been confirmed that the elastic response of the brain tissue is extremely nonlinear. Regarding this, time-independent hyperelastic models which can describe the nonlinearity, as well as the anisotropicity behavior [75-77], are utilized. Extensive research is still being developed to evaluate and calibrate various hyperelastic constitutive models for brain tissue [76, 78-83]. Additionally, to consider the viscous and porosity, several time-dependent constitutive relations, such as linear viscoelastic and hyper-viscoelastic models, have been developed to demonstrate the viscoelastic nature of brain tissue. Although experimental results prove that the mechanical response of the brain tissue is directly affected by the loading rate and the time, it has been considered as a time-independent substance in a great deal of the research. There is an overall agreement to enhance constitutive models, and more phenomenological concepts in brain tissue mechanics needs to be considered.

For a rate-dependent material such as the brain, it's necessary to pick the right material properties corresponding to the simulation rate, because modeling TBI is of a dynamic nature and the brain will undergo a variety of loading rates at different scenarios. It should be noticed, that the effective time durations in higher frequency load, such as impact-induced and blast-induced TBI, are respectively within the order of some and less than one millisecond [84]. In case of a surgical application, however, the time duration will be in the scope of few seconds. Distinct from strain values, severe brain injury, under blunt impact, normally occurs with the loading rate varied from 23 to 140 s^{-1} by an average of 84 s^{-1} [84-86]. Therefore, during studying impact-induced TBI

in FE modeling, it's recommended to use material constants obtained not outside the mentioned range of loading rates.

1.3. Research objectives and scope

The goal of this thesis is to advance the knowledge of brain tissue and to model the rate-dependent behavior of tissue facilitating diagnosis of brain injury and even in the neurosurgical analyses. This manuscript will concentrate on developing the rate-dependent constitutive representations of brain tissue, which is a prerequisite for the analysis of brain performance under dynamic loading. The project will introduce both single-phase and biphasic characterization technique that will be verified both computationally and experimentally. The rate-dependency of soft brain tissue will be measured experimentally and reflected in the constitutive formulations.

Before conducting the test, a reasonable range of strain rates for brain injury (caused by impact or blast scenarios) has to be estimated. These strain rates cannot be measured in-vivo, therefore a computational FE analysis of the human head will be conducted to predict the strain rates for loading scenarios associated with brain injury.

A set of experimental measurement for mechanical behavior of the brain tissue at high strain rates is designed and conducted. In the first step of material characterization, a single-phase rate-dependent formulation is employed to investigate the mechanical response of the tissue. Then in the next step, the tissue treated as a porous medium and represented by a biphasic model. In both single-phase and biphasic constitutive modeling, the suggested models are assigned to capture the nonlinear elastic and rate-dependent behavior of the brain tissue. A flowchart of the research objectives for the current manuscript are illustrated in Figure 1.

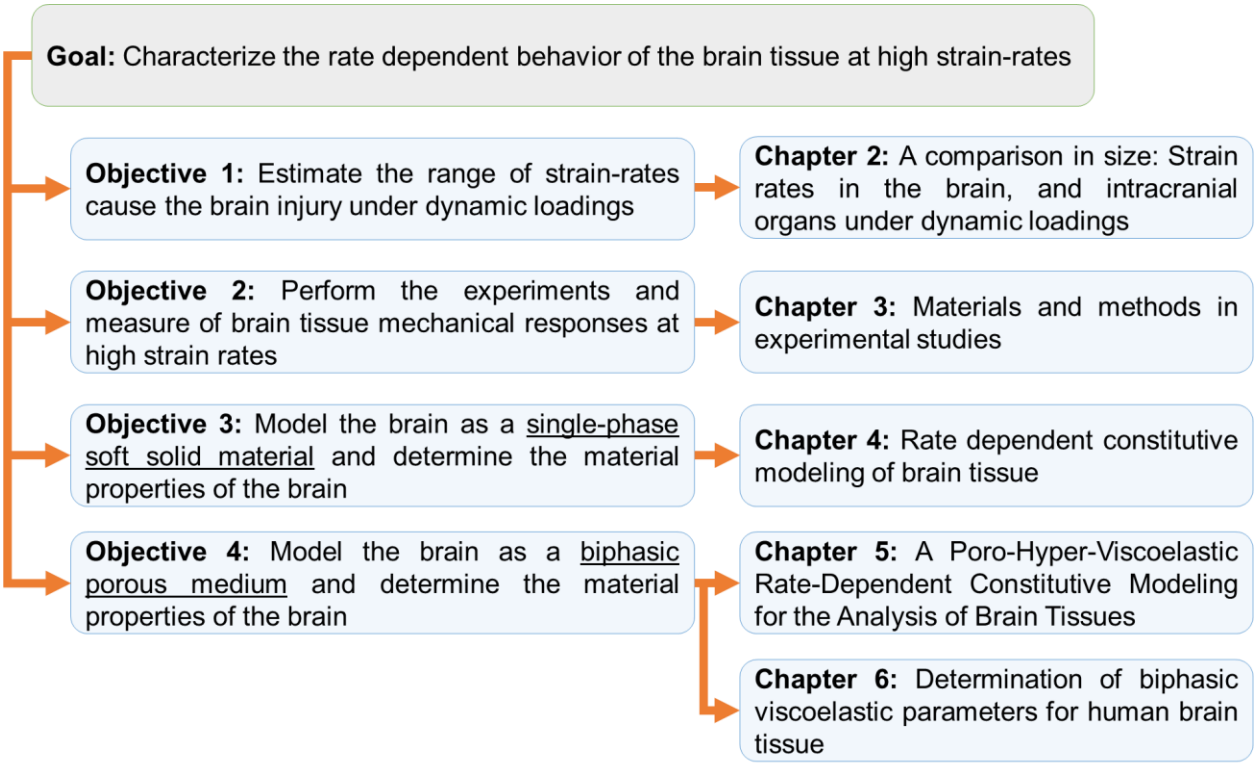

Figure 1. Thesis overview, and the summarized flowchart of the goal, objectives, and organization of the chapters.

1.4. Dissertation structure

The current thesis includes six chapters, and one appendix section to provide and to meet the required information on the aforementioned objectives. In the 1st Chapter, the introduction, backgrounds, and the general scope of this manuscript are provided. In Chapter 2, the procedure of getting primary estimation for the range of strain rates associated to brain injury is explained, and the result are provided. In Chapter 3, the experimental procedure for conducting the test on animal brain tissue are described, and the result are statistically analyzed and the effect of rates in the mechanical behavior of the tissue is demonstrated. In Chapter 4, the first constitutive model which accounts for the rate-dependency behavior and consider the brain as a mono-phase soft solid material is introduced. In Chapter 5, the brain tissue is considered as a porous medium consisted of solid and fluid phases and represented by a biphasic model. In Chapter 6, the material properties

of the human brain tissue is determined through the biphasic constitutive model. At the end, in the Chapter 7, the conclusions and suggestion for future works are provided.

CHAPTER 2. A COMPARISON IN SIZE: STRAIN RATES IN THE BRAIN, AND INTRACRANIAL ORGANS UNDER DYNAMIC LOADINGS[1]

2.1. Introduction

Mechanical properties of brain tissue are a fundamental subject of biomechanics and have been extensively studied in the last few decades [3, 19, 22, 87-94]. It was shown that the mechanical behavior of the brain is dominated by the loading rate and varies nonlinearly with any change in strain, as well as with its strain rate [62]. Typically, soft biological materials such as brain and brainstem present complex mechanical responses characterized by large strains, load history and rate sensitivity [54, 55, 62, 91, 95, 96]. Since brain and brainstem tissues are rate-dependent materials, great care should be taken for selecting proper material properties from corresponding strain rates in different scenarios.

Dura matter (a surrounding membrane of brain) and skull which hold and protect the brain, have significant roles in the analysis of the TBI incidents. Therefore, determining the material properties of the dura and cranial bone was the subject of earlier researches in biomechanics [36, 97]. Both theoretical and experimental studies have shown the dura and cranial bone present rate-dependent material properties [98-100]. Although linear and hyperelastic models can approximate the behavior of dura and skull very well at each rate [99, 101], they behave differently under various speeds of loading. For instance, Persson et al. [99] tested dura mater under uniaxial tension at three various strain rates of 0.01, 0.1, and 1.0 s^{-1}. They postulated the mechanical responses of dura is rate-dependent, however they fitted their results to the rate-independent hyperelastic Ogden model. Also, experimental tensile results indicated the Young's modulus of the cranial bone varies

[1]Hosseini-Farid, Mohammad, Ramzanpour, Mohammadreza, Ziejewski, Mariusz, and Karami, Ghodrat. Mohammad Hosseini-Farid had primary responsibility for this chapter, and the rest of co-authors help him to proof-read this chapter for being submitted as a journal paper titled as "Strain rates in the brain, and intracranial organs under dynamic loadings".

from 8 GPa to 19.5 GPa for quasi-static to dynamic rates [102]. Therefore, to have a correct result at each FE simulation, the right material properties corresponding to the rate of that application should be selected.

The majority of biomechanical characterizations for human head organs have been performed within experiments in relatively low strain rates. Recently, De Kegel et al. [101] have conducted some experiments for human dura specimens within strain rate of 1.0 s^{-1}. They have obtained highly nonlinear behavior for dura, and characterized its mechanical response using three different hyperelastic material models. Franceschini et al. [40] have experimentally studied the mechanical behavior of human brain tissue at strain rates ranging between 0.0055 and 0.0093 s^{-1}. Although, their results are valid to be employed for studies in quasi-static loading, those material properties have been used in many computational simulations of TBI at dynamic loads [103, 104]. It was confirmed [23, 62] that, besides selecting an appropriate constitutive model, using the material constants derived from a mismatched strain rate may considerably affect the validity of the results. Farid et al. [62] showed that the hyper viscoelastic material models, which are optimized for various low strain rates will consequence in considerable errors when predicting brain behavior at higher strain rates. Therefore, it is crucial to know the range of strain rates at dynamic loading conditions and characterize the material properties of head organs at those rates.

Finding the ranges of strain rate for brain, brainstem, dura, and skull in TBI resulted simulations can help in determining and using the material properties at the right rate. The strain rates of different incidents cannot be measured in-vivo, therefore a computational FE analysis of the human head will be conducted to predict the strain rates for loading scenarios associated with brain injury [94]. In this chapter, impact and blast assault simulations are conducted on a developed FE human head model to predict the range of strain rates. In this manuscript, it was assumed that

the brain will experience minor injuries by blunt impact [1] and an effective brain injury caused by blast [105]. This approach came from the fact that impact and blast load types are inherently different and cannot be directly compared to each other. The findings will provide a ground basis for determining more relevant material properties for the strain rates corresponding to impact and blast cases.

2.2. Material and methods

2.2.1. Finite element of head model

Using Computed Tomography scan technique and Magnetic Resonance Images, the geometry of the 50th percentile human head-neck model was developed by Horgan et al. [106]. The model contains all critical components of the head and the neck, including brain, cerebrospinal fluid (CSF), pia mater, dura mater, facial bone, neck bone, neck muscle, skull, and scalp. In this study, all head components have been modeled as linear elastic material (Table 2), except the brain and brainstem which are modeled as hyper viscoelastic (Table 2) and viscoelastic (Table) material [1], respectively. The Mooney-Rivlin strain energy coupled with linear viscoelastic function was used as the constitutive relation of the brain given by Equation (1). Also, the linear viscoelastic material model expressed by Equation (2), was employed to represent the shear characteristics of brainstem. A linear material model with 10 GPa of Young's modulus was considered for the skull. The developed head model was examined and validated [105] with respect to the experimental results of Nahum et al. [107].

$$W = \int_0^t \left\{ \left(1 - \sum_{k=1}^{M} g_k (1 - e^{-(t-\tau)/\tau_k}) \right) * \left(\frac{d}{d\tau} \left[\sum_{i+j=1}^{N} C_{ij} (I_1 - 3)^i (I_2 - 3)^j \right] \right) \right\} d\tau \quad (1)$$

$$G(t) = G_\infty + (G_0 - G_\infty) e^{-\beta t} \quad (2)$$

Table 1. Head model component properties and mechanical properties [1, 108].

Segment Name	Constitutive Model	FE Model	Density (kg/m^3)	Poisson's Ratio	Young's Modulus (MPa)	
Tentorium	Linear Elastic	Shell Element	1133	0.45	31.5	
Dura Matter	Linear Elastic	Shell Element	1133	0.45	31.5	
Pia Matter	Linear Elastic	Shell Element	1130	0.45	11.5	
Falx	Linear Elastic	Shell Element	1133	0.45	31.5	
Skull	Linear Elastic	Solid Element	1300	0.24	10000	
Neck-Bone	Linear Elastic	Solid Element	1300	0.24	10000	
Neck-Flesh	Linear Elastic	Solid Element	1130	0.45	0.1	
Face-Bone	Linear Elastic	Solid Element	1200	0.42	16.7	
Face-Skin	Linear Elastic	Solid Element	1200	0.42	16.7	
Scalp	Linear Elastic	Solid Element	1200	0.42	16.7	
Golf Ball	Linear Elastic	Solid Element	1100	0.49	300	
CSF	Linear Elastic (Fluid Opt.)	Solid Element	1040	Poisson's Ratio	Bulk Modulus	Viscosity Coefficient
				0.49	2190	0.2

Table 2. Mooney-Rivlin hyper viscoelastic constants of the brain used in FE modeling [1].

Density (kg/m^3)	C_{10} (Pa)	C_{01} (Pa)	g_1 (Pa)	g_2 (Pa)	β_1 (s^{-1})	β_2 (s^{-1})
1040	31	35	407	233	125	6.7

Table 3. Viscoelastic material parameters of the brainstem used in FE modeling [1].

Density (kg/m^3)	Bulk Modulus (GPa)	G_0 (kPa)	G_∞ (kPa)	β (s^{-1})
1060	2.19	22.5	4.5	80

2.2.1.1. Impact case

The injury caused by a golf ball impact, is one of the most leading causes of head injury in sports-related impacts [109]. The possibility of being hit by an occasional golf ball is common for both the players and the people who watch the game[110]. This case of impact was simulated to

evaluate the strain rate as an example of the general blunt impact applications. The simulations of a golf ball impact were done for a ball flying at speeds of 10, 15, and 20 m/s. As suggested by Lee, et al [108], these ball speeds were selected in such a way to avoid severe brain injury. Since the directionality has notable influences [87], the simulation was performed for three directions of back, frontal and lateral impact. Figure 2 presents the impact setup for two directions of frontal and lateral. Table 4 provides the summery of the simulated impact scenarios in this study. The neck is assumed to be fixed in the translational displacements [108].

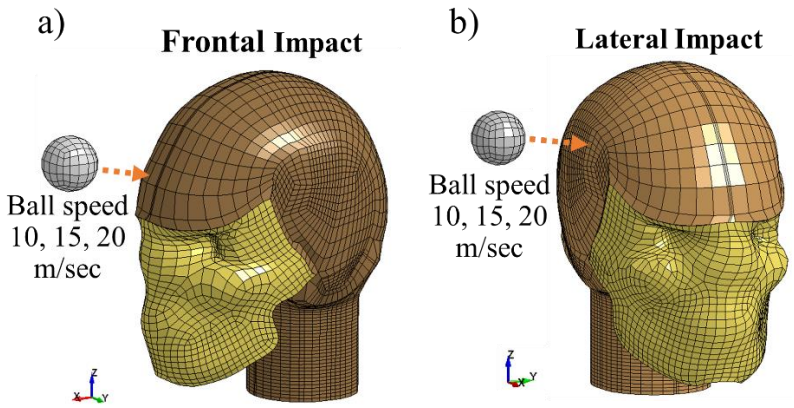

Figure 2. Setup of frontal and lateral impact by golf ball in FE head model.

Table 4. The summery of impact cases by golf ball applied in FE modeling for estimating the ranges of strain rates.

Case code	Impactor	Speed (m/s)	Direction
Impact# 1	Golf ball	10	Lateral
Impact# 2	Golf ball	15	Lateral
Impact# 3	Golf ball	20	Lateral
Impact# 4	Golf ball	10	Back
Impact# 5	Golf ball	15	Back
Impact# 6	Golf ball	20	Back
Impact# 7	Golf ball	10	Frontal
Impact# 8	Golf ball	15	Frontal
Impact# 9	Golf ball	20	Frontal

2.2.1.2. Blast case

High strength explosion waves are a possible source of TBI. In this work, the same head model was also being used for blast simulations. Protecting the head with a helmet can reduce the severity of the brain injury, but injury can still occur when the person is exposed to blast [111]. As illustrated in Figure 3, a three-dimensional model of an advanced combat helmet (ACH) is integrated with the head-neck model. In this study, the blast simulation was conducted for the protected and unprotected head in two back and lateral direction. The standoff distances are set to be one and two meters from the explosion site. In LS-Dyna the standard trinitrotoluols (TNT) is selected as the high explosive (HE) material. Because of a very short effective time on the blast (less than 1 ms) a free boundary condition was applied to the end of neck. Rezaei et al. [112] has shown the blast waves of 95 grams HE placed 750 mm far from the human head can cause a severe and fatal brain injury. In addition to this case (95 gr TNT), which will be referred to as "*heavy blast"* in this manuscript, eight other blast scenarios with 75 gr of HE mass were chosen and listed in Table 5.

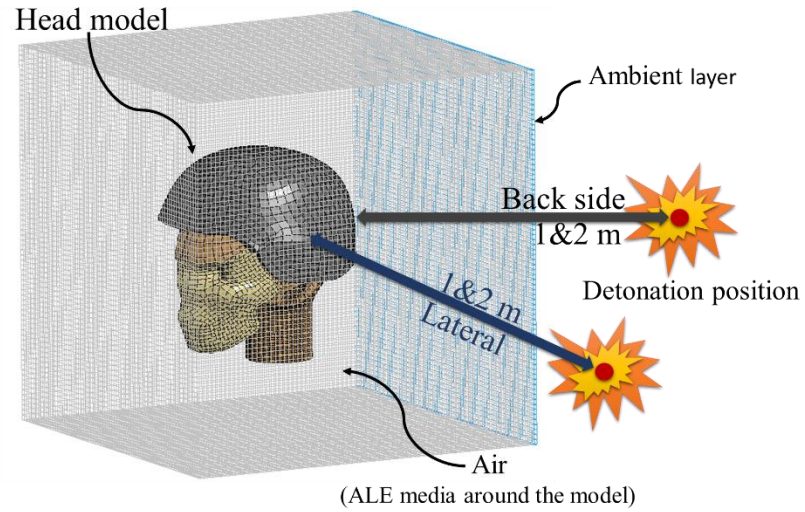

Figure 3. The position of the detonation at side and back of the protected head model.

Table 5. The summary of blast scenarios implemented in FE simulations to predict the ranges of strain rate associated to TBI.

Case code	Head condition	Explosive mass (gr)	Distance (m)	Direction
Blast# 1	Protected	75	1	Back
Blast# 2	Protected	75	2	Back
Blast# 3	Protected	75	1	Lateral
Blast# 4	Protected	75	2	Lateral
Blast# 5	Protected	95	0.75	Back
Blast# 6	Unprotected	75	1	Back
Blast# 7	Unprotected	75	2	Back
Blast# 8	Unprotected	75	1	Lateral
Blast# 9	Unprotected	75	2	Lateral
Blast# 10	Unprotected	95	0.75	Back

To determine the behavior of the explosive gas, the equation of state (EOS) must be defined. This Equation of state (EOS) explains pressure–volume–energy relationships of the gaseous form of detonation. The EOS regarding blast pressure wave generated by HE detonation can be expressed using the Jones–Wilkins–Lee (JWL) equation as [113]:

$$p = A\left(1 - \frac{\omega}{R_1 V}\right)e^{R_1 V} + B\left(1 - \frac{\omega}{R_2 V}\right)e^{R_2 V} + \frac{\omega E}{V} \quad (3)$$

where ω, A, B, R_1, and R_2 are constants that are defined by the user, E is the internal energy per initial volume, and V is the relative volume. The numerical data for these parameters are derived from the explosive handbook by Dobratz [114].

2.3. Results

FE simulations of the head impacted by a golf ball are performed for different impact directions and ball speeds as were stated in Table 4. Also, the mentioned blast scenarios presented in Table were implemented to the head model. The resultant linear acceleration of the human head for three cases of impact and four scenarios of blast are measured and shown in Figure 4 a, b.

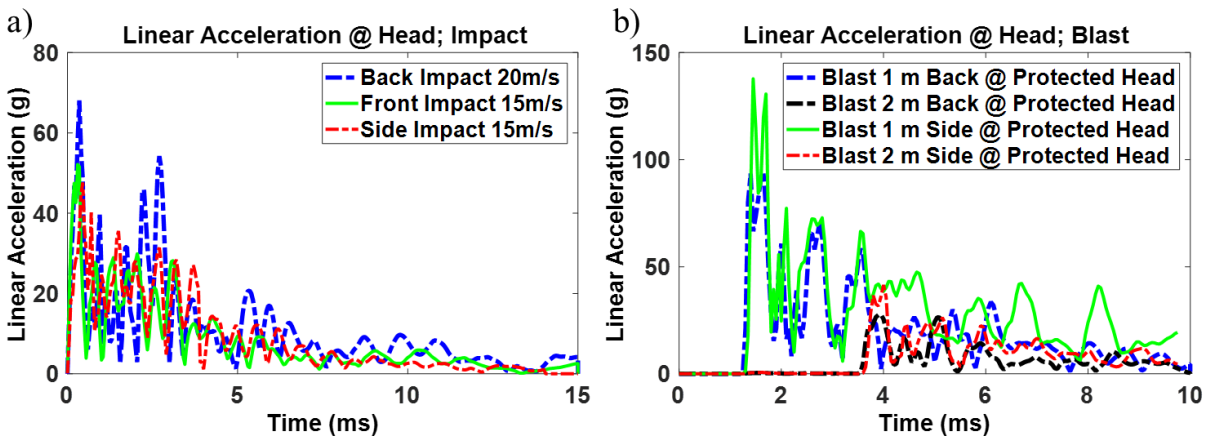

Figure 4. Resultant linear acceleration for the head at: a) impact in three directions, and b) four cases of blast.

Figure 5 presents the blast wave propagation and intracranial pressure (ICP) distribution in the brain which is necessary to predict the brain behavior during the blast. As it can be seen, for this case (backward *heavy blast*) the ICP in brain exceeds 300 kPa, therefore, a severe TBI should be expected [1]. Furthermore, in comparison to Rezaei et al. study [112], it proves that the selection of HE masses and its distance from the head was adequate to create such a condition.

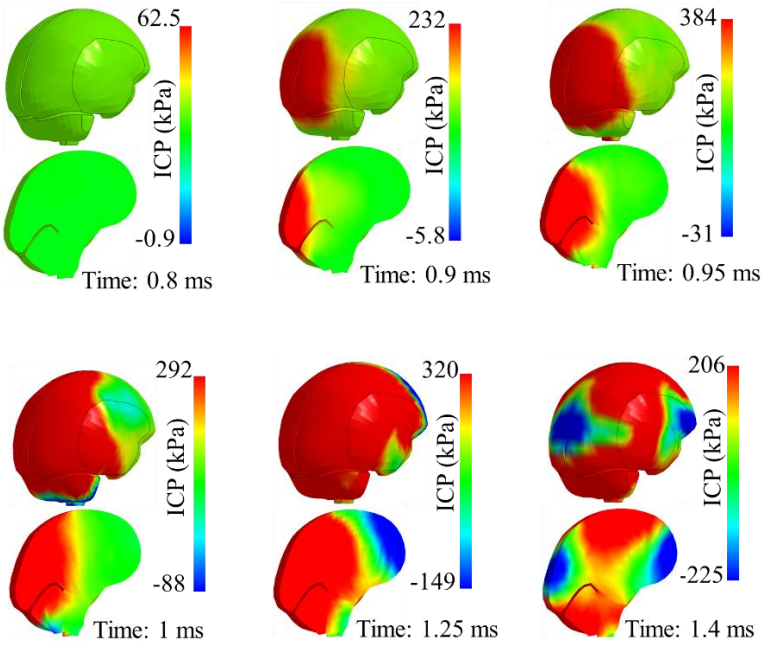

Figure 5. ICP (kPa) contours in the brain for the protected head in heavy blast for whole brain and also cross-sectional view.

The strain rate distribution for all elements in the brain, brainstem, skull and dura were examined. Like other mechanical features such as strain or stress, the strain-rate was found to has non-uniform distribution. For instance, in brain, the maximum strain rate occurs only in a relatively small zone (some elements) which takes place in different locations for each case, and the rest of the brain observes a moderate regime of rates. Figures 6 a, b illustrate the history of 1^{st} principal strain rate in three different locations of the brain for the head impacted by a golf ball. For the case where the ball hit the front of head with 15 m/s of speed, the maximum strain rate does not happen in coup nor contrecoup. However, it was found that for lateral impacts, the highest rate happens at coup zone. This shows the location of maximum rate can occur in every area of the brain and varies for several impact scenarios. Similarly, Figures 6 c, d depict the brain strain rates by the same criteria for the protected and unprotected heads under *heavy blast* conditions. For blunt impact cases, the elements of skull, which are located at impact side are observed to have the highest strain rates. Also, for all blast simulation (lateral and back side) the maximum rates occur at the temporal bone which has the lowest cranial thickness.

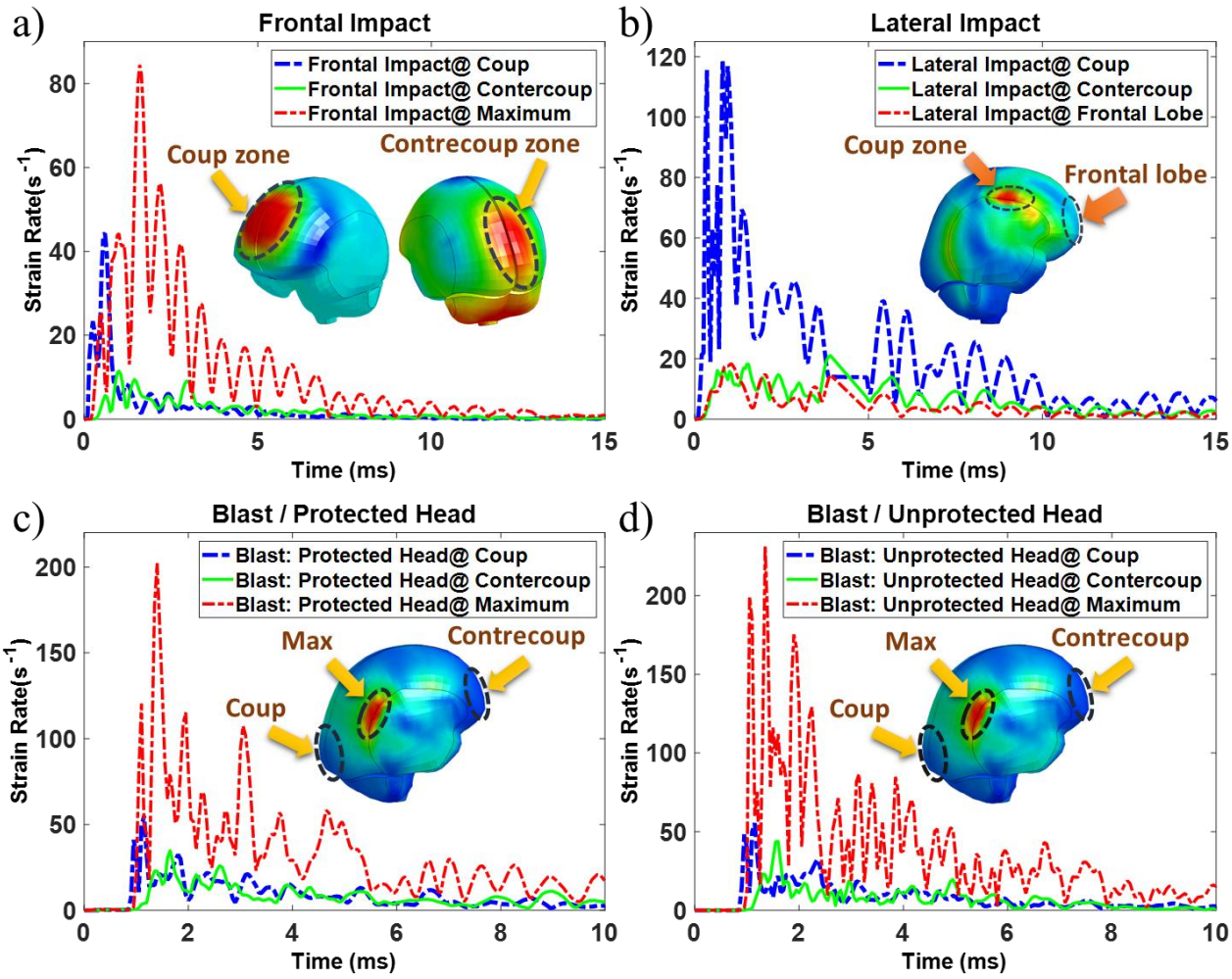

Figure 6. Histories of strain rate at three different regions of the brain under: a) frontal and b) lateral impact by golf ball, and heavy blast scenarios for c) protected and d) unprotected head.

In this study the maximum shear strain rate was determined for brainstem since it has been shown the dominant cause of injury at brainstem occurred due to shear strain [111]. Figures 7 a-d demonstrate the histories of the strain rate at regions with highest values of rate in brain, brainstem, skull and dura under three directions of impact. In addition, the computed strain rates at points with maximum rates in these head parts under four scenarios of blast are plotted and shown in Figures 8 a-d. Finally, the maximum linear acceleration of the head and highest calculated strain rate in the brain, brainstem, skull and dura for all impact and blast cases are demonstrated in Table and Table 7, respectively. Since, the values of the acceleration in all impact scenarios are less than

90 g [1], the damage level can be considered minor or close to the mild TBI. Head accelerations in some blast cases exceed 90 g, so severe brain injuries are expected under those circumstances.

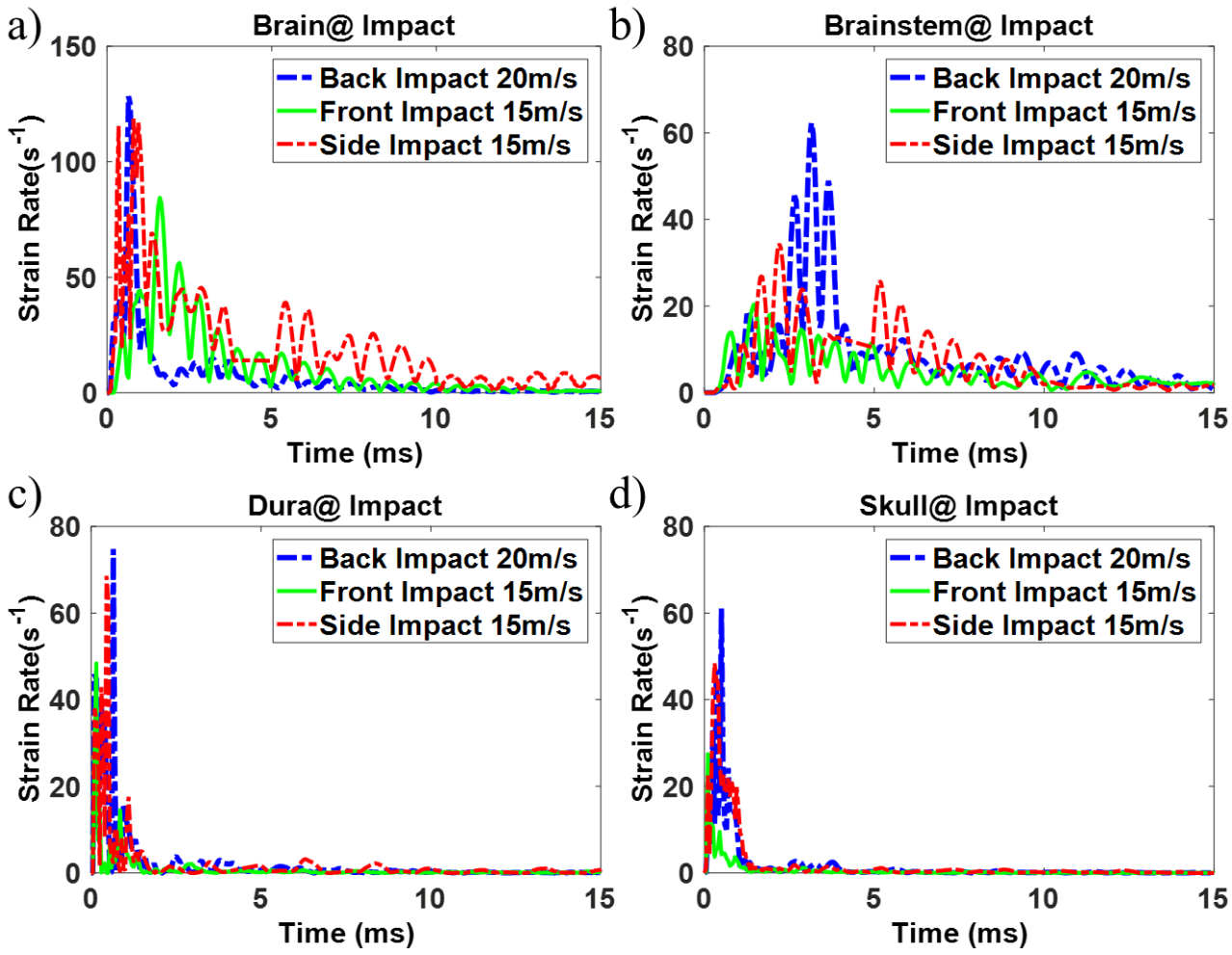

Figure 7. History of highest calculated strain rate under three blunt impact cases for: a) brain, b) brainstem, c) dura, and d) skull.

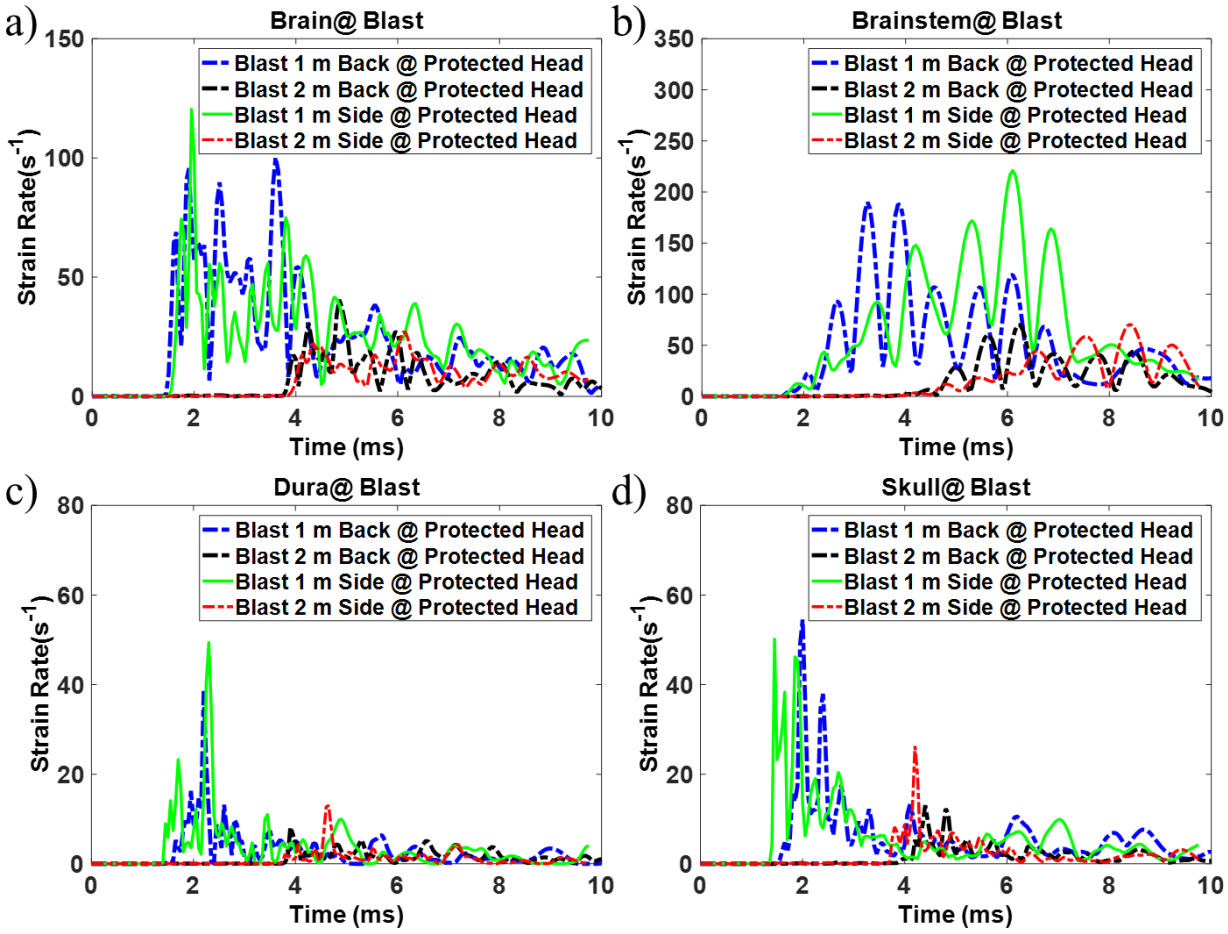

Figure 8. History of highest calculated strain rate during four blast scenarios for: a) brain, b) brainstem, c) dura, and d) skull.

Table 6. The estimated maximum linear acceleration of skull, and strain-rate of the brain, brainstem, skull and dura at different impact scenarios.

Case code	Max. skull acceleration (g)	Max. strain-rate in brain (s^{-1})	Max. strain-rate in brainstem (s^{-1})	Max. strain-rate in Dura (s^{-1})	Max. strain-rate in skull (s^{-1})
Impact# 1	33	85	24	49	35
Impact# 2	47	105	35	68	45
Impact# 3	82	180	68	103	48
Impact# 4	23	42	21	38	22
Impact# 5	61	67	43	62	37
Impact# 6	68	132	60	75	61
Impact# 7	34	56	15	43	16
Impact# 8	52	81	24	54	31
Impact# 9	70	142	35	76	42

Table 7. The predicted maximum linear acceleration of skull, and strain-rate of the brain, brainstem, skull and dura at different blast scenarios.

Case code	Max. skull acceleration (g)	Max. strain-rate in brain (s^{-1})	Max. strain-rate in brainstem (s^{-1})	Max. strain-rate in Dura (s^{-1})	Max. strain-rate in skull (s^{-1})
Blast# 1	93	100	165	39	55
Blast# 2	30	40	70	8	14
Blast# 3	140	120	228	55	51
Blast# 4	41	36	71	13	26
Blast# 5	226	205	338	144	122
Blast# 6	180	115	214	62	64
Blast# 7	38	48	62	15	20
Blast# 8	205	180	151	122	66
Blast# 9	63	73	47	32	28
Blast# 10	432	241	412	149	182

2.4. Discussion

Evaluating mechanical properties of the human head organs is fundamental in understanding intracranial brain deformation under different loading conditions. It is known that the brain has rate-dependent behavior and gets stiffer by increasing the loading rate [62]. That's why, in literature, it is common to conduct the in-vitro tests with certain strain rates to capture the wider properties of brain [69]. Similar approaches have been applied to identify the material parameters of brainstem, dura, and other rate-dependent biological tissue [57, 99]. Cranial bone was found to behave differently at various rates [98]. It was reported that the bone tissue for the skull at high rates (150 s^{-1}) can respond up to 200% stiffer as skull in quasi-static rates [102]. Therefore, for simulating these rate-dependent materials in dynamical studies such as TBI cases, the validated properties over the desired range of strain rates must be employed. In this regard, the findings of this chapter proposing a measure for the range of the rates needed for conducting the in-vitro test and also selecting material properties from the right strain rates.

The time duration of a general head impacts is in the order of milliseconds, while in the case of a high-speed load such as blast wave is less than one millisecond. Regardless of the strain value, it was found the brain injury caused by impact happens with the brain strain rate of 23 to 140 s^{-1} with an average of 84 s^{-1} [84, 85]. Using a validated FE head model is a very feasible approach for determining the strain rates of the brain and skull under loading. Clinical studies of reconstructed head impact simulations which led to mild TBI for 58 football players, proposed a range of 35-97 s^{-1} for the brain strain rate [10]. Viano et al. [15] analyzed 28 cases of NFL impacts involving 22 concussions by FEM and they found the brain strain rate for those incidents were in the range of 19-162 s^{-1}. To the best of the authors' knowledge, there is no reported study in the literature pointing out the range of the strain rate from experimental measurement of in-vivo or cadaver test.

In this chapter some impact and blast scenarios were modeled on a validated head model. Results (Table 6, Table 7) showed that under these dynamic loads the response of brain and brainstem were in the range of 36 to 241 and 15 to 412 s^{-1}, respectively. Meanwhile, the estimated strain rates of the dura and skull during such impact and blast loads were respectively in the range of 8 to 149 and 14 to 182 s^{-1}. Significant correlations of strain rates with linear head acceleration for brain, brainstem, dura and skull were found and presented in Figures 9 a-d. These linear regressions were independent of the effects of direction and speed of impactor, as well as the HE mass, distance, direction and head condition (protection) under blast. They proposed the strain rates of brain, brainstem, dura and skull are respectively 1.9 ($R=0.8$, $P<0.01$), 0.7 ($R=0.9$, $P<0.01$), 1.18 ($R=0.9$, $P<0.001$) and 0.7 ($R=0.6$, $P<0.01$) times of resulted head acceleration by impact. In addition, under blast incidents, the brain, brainstem, dura and skull behaved with the strain rate of 0.86 ($R=0.96$, $P<0.001$), 1.25 ($R=0.9$, $P<0.001$), 0.52 ($R=0.95$, $P<0.001$) and 0.43 ($R=0.9$,

P<0.001) times of acceleration, respectively. Figure 9 shows that for the equivalent linear acceleration of head, the strain rates induced by impact for brain, dura and skull are higher in comparison to the blast one.

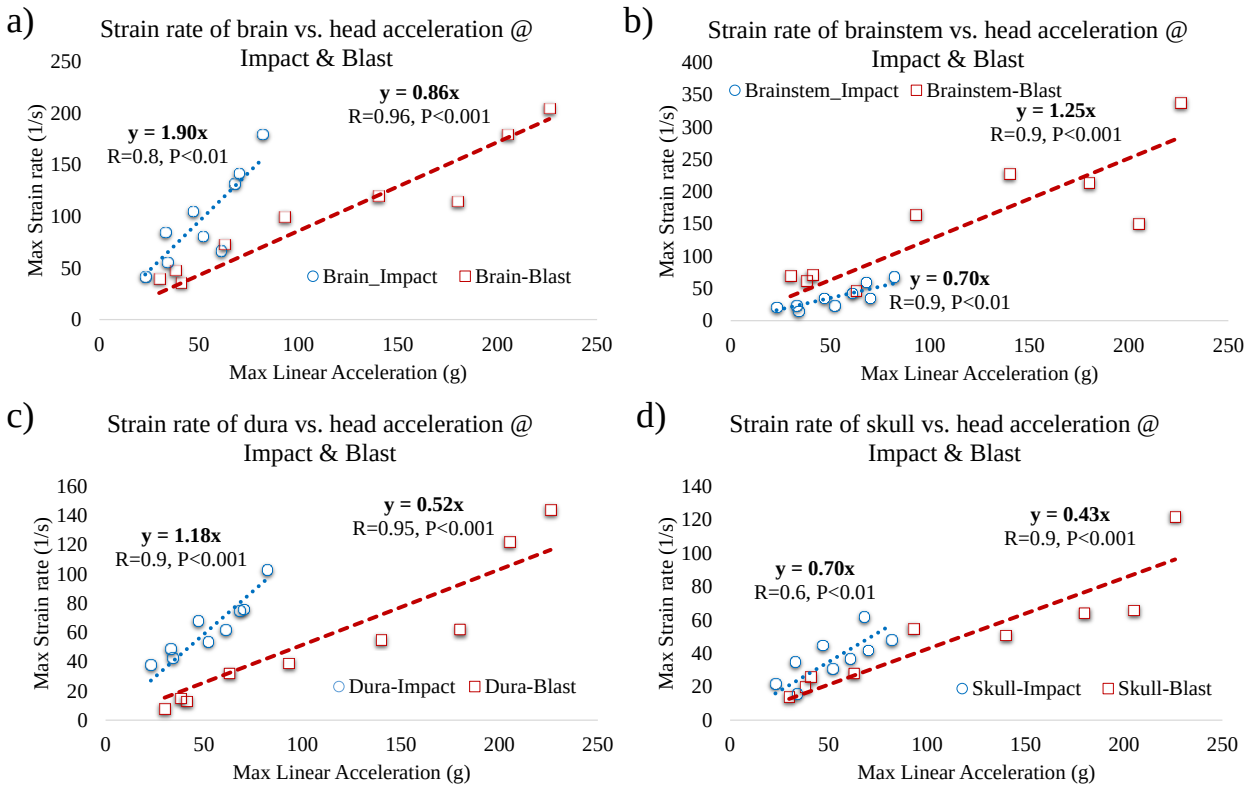

Figure 9. Linear regression of highest evaluated strain-rate versus maximum acceleration of head under impact and blast cases for: a) brain, b) brainstem, c) dura, and d) skull.

As a first limitation of this study, the result was not based on a general impact or blast conditions. Numerous cases of other simulations for various scenarios of blunt impact and blast are required instead of the chosen limited representative cases. Therefore, it should be mentioned the estimated range of rates are more likely to happen for a blunt impact causing mild TBI, and a blast lead to concussion or brain injury [1, 84]. As another limitation, the FE simulations were done with one set of material properties. Among material properties available in literature, those which were determined at highest dynamic rates were selected. However, the findings of this study still recommend that there is a necessity to characterize those material properties at even higher

ranges. Thus, the results of this thesis can be considered as the first step in having the true estimation of selecting the right material properties in dynamical simulations.

2.5. Conclusions

Cranial bone, and particularly brain, brainstem, and dura are highly rate-dependent materials and will behave differently in various strain rates. In order to study the biomechanics of TBI through FE methods, it is necessary to implement correct properties associated with anticipated application rates. However, to calculate the material properties of brain, brainstem, dura, and skull related to TBI cases, we need to know for which range of strain rates they are required to be examined. In this study, FE simulation was performed to estimate the strain rate ranges in impact and blast. It was found the brain and skull experience strain rates in the range of 36 to 241 s^{-1} and 14 to 182 s^{-1} for impact and blast incidents respectively. Also, in such dynamical simulations, the brainstem and dura behave at strain rates of 15 to 412 s^{-1} and 8 to 149 s^{-1}, respectively. Knowing these ranges provides a good measurement for more accurate characterization of these materials. Additionally, representing the rates based on head acceleration helps to get a better idea of selecting material properties in advance. It was shown in the impact incidents, the strain rates of brain, brainstem, dura, and skull were approximately 1.9, 0.7, 1.18 and 0.7 times the head acceleration. Also, under blast loadings, the strain rates for those head organs were around 0.86, 1.25, 0.52- and 0.43-times of head acceleration.

CHAPTER 3. MATERIALS AND METHODS IN EXPERIMENTAL STUDIES FOR BRAIN TISSUE

3.1. Materials and methods

3.1.1. Experiments

In this study, due to limited access to human brain, the experiments are conducted on the animal brains. While the methods and modeling will be calibrated and verified for animal brains, they can be applied to human brains with good approximations. Experiments have shown that their behaviors can simulate the human brain with good approximations [69]. The samples will be prepared according to reported protocols [58, 59, 86]. IRB and IACUC regulations will be observed during whole the study process.

In order to prepare the brain samples, four fresh bovine brains were obtained from the Animal Science Department facilities at North Dakota State University. The animals were 24 months old, and all were healthy. The brains were carefully taken out from the cranium and put immediately into a phosphate-buffered saline (PBS) solution to prevent dehydration. All the in-vitro tests were conducted within three to eight hours after the slaughtering. The brain samples were cut from the frontal and parietal lobes of each hemisphere. The procedure followed the experimental protocol by Miller and Chinzei [115] designed to prepare samples for uniaxial unconfined compression tests. Using surgical scalpels and a cutting tool made from steel pipe with sharp edges, the cylindrical shape specimens from different regions of brain were cut with a diameter of 25 mm and 15 mm height (Figure 10). The actual measured diameter and height of samples before conducting the experiment were 24.8 ± 0.3 mm and 15.0 ± 0.3 mm (mean ± SD). All the extracted brain specimens were consisted from a mixture of gray and white matter.

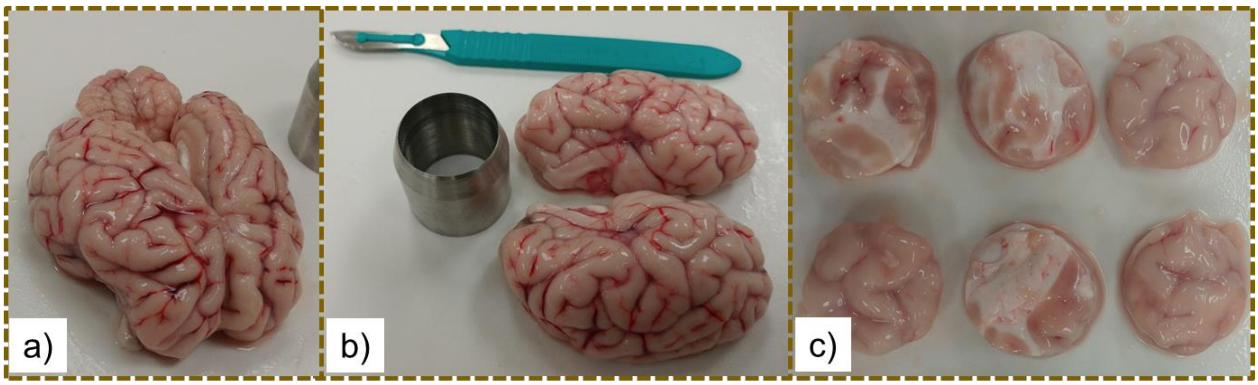

Figure 10. Sample preparation and experimental setup for an in-vitro unconfined compression test: (a) fresh animal brain and the cutting tool, (b) separating two hemispheres for cutting, (c) circular cutting tool used to extract cylindrical brain samples.

The unconfined compression experiments were conducted on the mixed gray and white matter specimens up to 30% strain of each sample height (λ=0.7). Tests were performed at room temperature (~22 ˚C) using a BOSE 3200 Electroforce machine (BOSE Corporation, Bloomington MN, USA) designed for testing soft tissue materials [116]. Figure 11 shows the test setup of the conducted unconfined compression experiments. To establish unconfined compression conditions, the top and lower platens surfaces were completely treated with a surgical lubricant (Surgilube, Fougera Pharmaceuticals Inc.) at the beginning of each test. This process is essential to diminish the frictional effects and to provide a uniform expansion in radial directions. Samples were then carefully placed between the two platens. To keep the tissue hydrated throughout the entire test procedure, the outer surface of each brain specimen was carefully humidified with phosphate-buffered saline solution. After hydration, the upper platen was cautiously moved downward until it touched the sample. Then, all forces and references displacement were set to zero. The experiments were performed at three different deformation rates of 10 mm/sec (n=10 brain samples), 100 mm/sec (n=8), 1000 mm/sec (n=12) which correspond to the approximate nominal strain rates of 0.67, 6.67, and 66.7 s^{-1}, respectively. The Electroforce machine used for the testing is shown Figure 11. Also, the radial expansion of cylindrical specimens was captured by a high-

speed camera (NanoSense MKIII, DantecDynamics) at different instants (Figure 11), confirming that the deformation was approximately homogeneous. It proves that employing the surgical lubricant was effective in minimizing the frictional effects between sample and the platens. Additionally, the high speed recorded videos helped us to make sure that no dehydration or drainage happened during the experiment procedure.

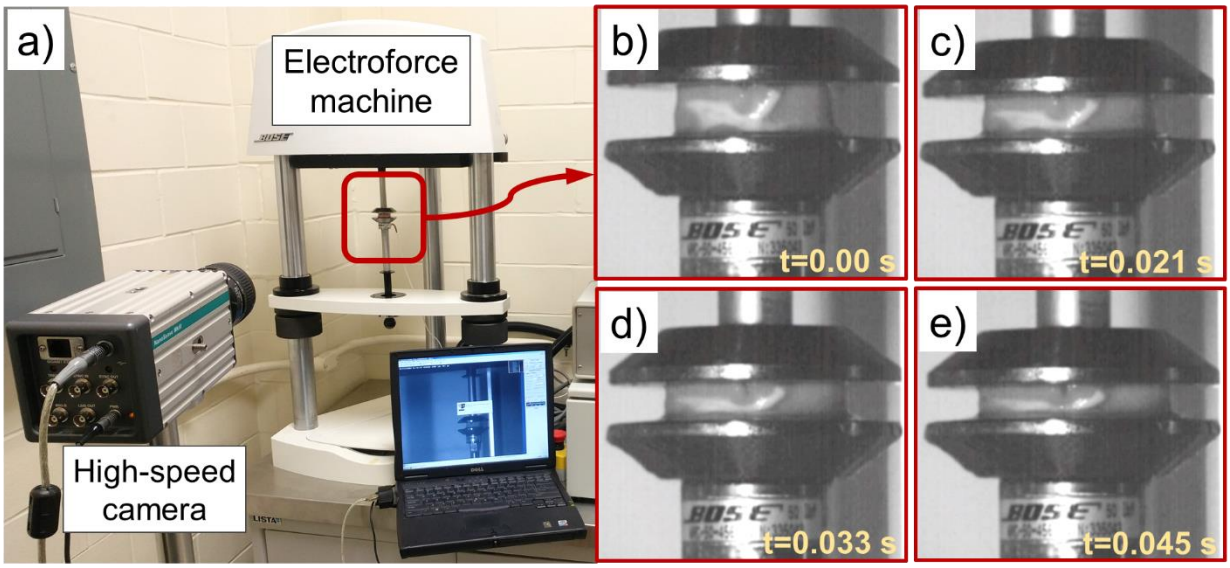

Figure 11. a) Electroforce machine ready for the in-vitro unconfined compression test while a high-speed camera records samples deformation, and the deformation steps of brain specimen with speed of 100 mm/sec in terms of time at b) t=0.00, c) t=0.021, d) t=0.033, and, e) t=0.045 sec, corresponding to compressive strain of 0, -0.14, -0.21, and -0.3, respectively.

3.2. Mechanical response of brain tissue

Based on force and displacement signals obtained directly from the testing machine, the stress histories versus the compressive strains were determined and presented in Figure 12. To attain the stress-strain behavior of bovine brain shown in Figure 12, the Lagrangian stresses were calculated by dividing the force over the initial cross-sectional area of sample at its reference configuration. The averaged nominal stress-strain curves were determined up to 30% of compressive strain, showing an inherent nonlinear mechanical behavior of tissue at each

deformation rate. The brain tissue showed stiffer response when the compression rate increased, indicating that the stress is not only a function of strain value but also depends on the loading rate.

The researchers of the study presented here could not find any studies with perfectly similar deformation rates of the bovine brain tissue to compare with their results. Good agreement was found, however, between results of the study presented here and the results provided by Laksari et al. [61]. In that study, an engineering stress of 10.3 kPa (at ε=-0.3) was reported for bovine brain sample under unconfined compression test at the nominal strain rate of 10 s^{-1}. Pervin and Chen [117] were able to examine the mechanical responses of bovine brain at high rates using a modified split Hopkinson pressure bar. They obtained insignificant anisotropy behavior for white matter and showed the compressive stress at 30% strain with nominal strain rate of 1000/s, was 60 and 75 kPa for gray and white matter respectively. Although, Rashid et al. [59] have examined porcine brain tissue, they determined the compressive stresses as 8.8, 12.8, and 16 kPa (at ε=-0.3) corresponding to compression velocities of 150, 300, and 450 mm/sec, respectively. These varying ranges were typical in the results of experimental studies. These are likely due to the fact that the samples were obtained from different animal species and ages, and prepared in different shapes and dimensions, and tested with different protocols (e.g. lubrication, preloading, etc.) [45, 118].

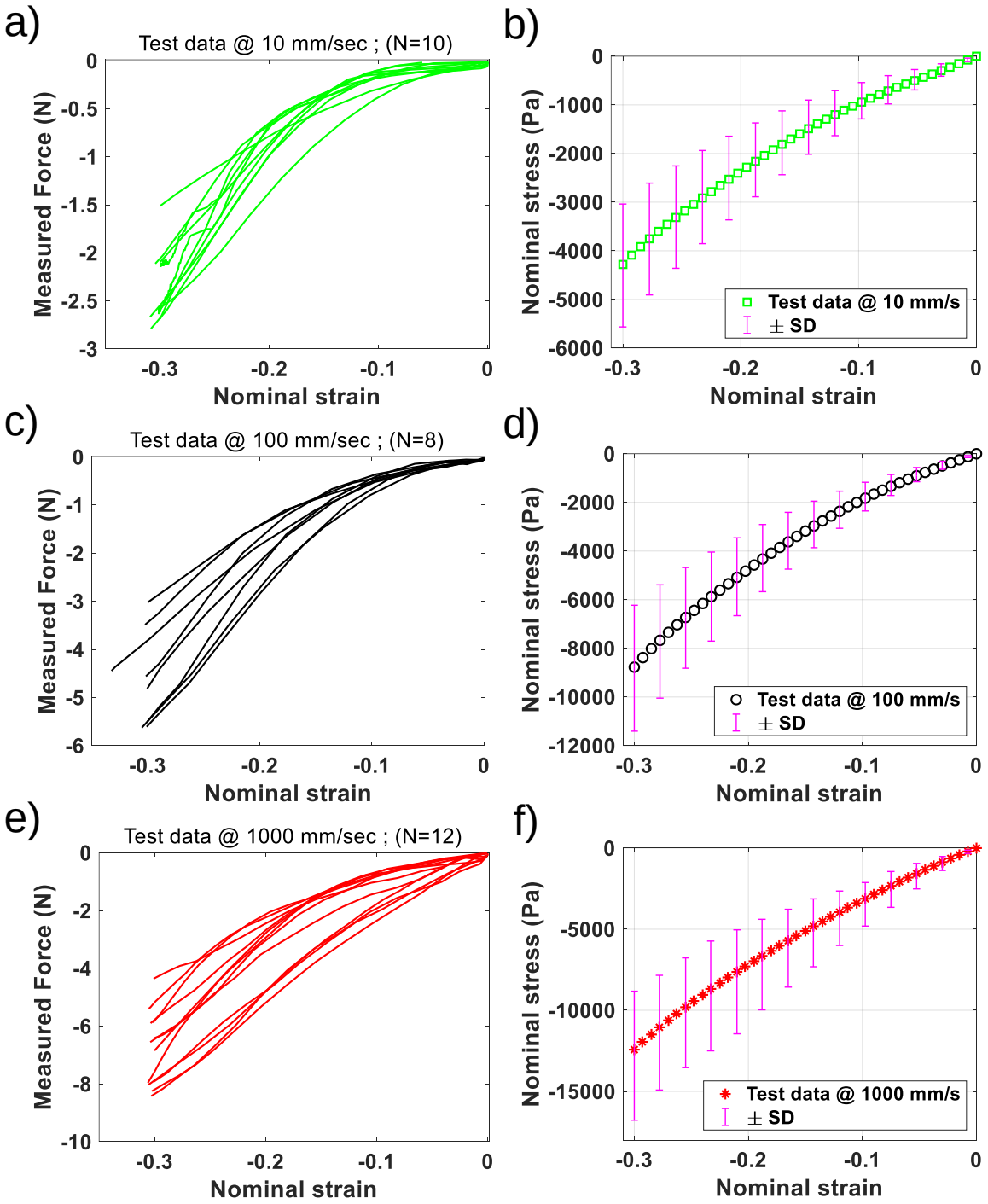

Figure 12. The experimentally recorded history of forces and the calculated nominal stresses (mean and standard deviation) vs. compressive strain for bovine brain specimens at different compression velocity of a, b) 10 mm/sec, c, d) 100 mm/sec, e, f) 1000 mm/sec.

3.3. Statistical analysis

The maximum nominal stresses at 30% compressive strain with the deformation rates of 10, 100 and 1000 mm/sec are -4.26 ± 1.26 kPa, -8.62 ± 2.58 kPa and -12.74.0 ± 3.97 kPa (mean ± SD), respectively. The mechanical response of brain tissue stiffened when the compression rate increased, indicating that the stress is not only a function of stretch ratio, but also depends on the loading rate (Figure 13). According to one-way ANOVA (OriginLab, Version 2018, OriginLab Corporation, Northampton, MA, USA) [119], the values of nominal stress at 30% strain showed significant statistically different (p < 0.01) over various deformation rates (Figure 14). The apparent elastic modulus (slope of stress-strain curve) at 5%, 10%, 15% and 20% strains for different compression velocities were determined and compared in Figure 14. A consistent rise in the elastic modulus was observed with increasing the strain levels and strain rates. As shown in Figure 14, this measure of mechanical stiffness demonstrated a statistically difference and significant rate-dependent behavior for brain tissue.

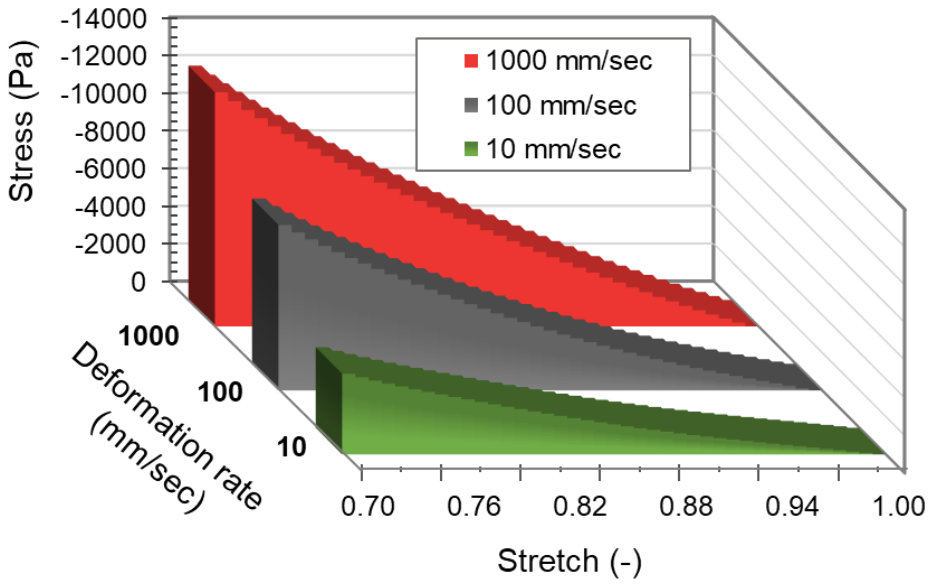

Figure 13. The comparison between mean nominal stresses (λ=1-ε) measured at three different compression velocities.

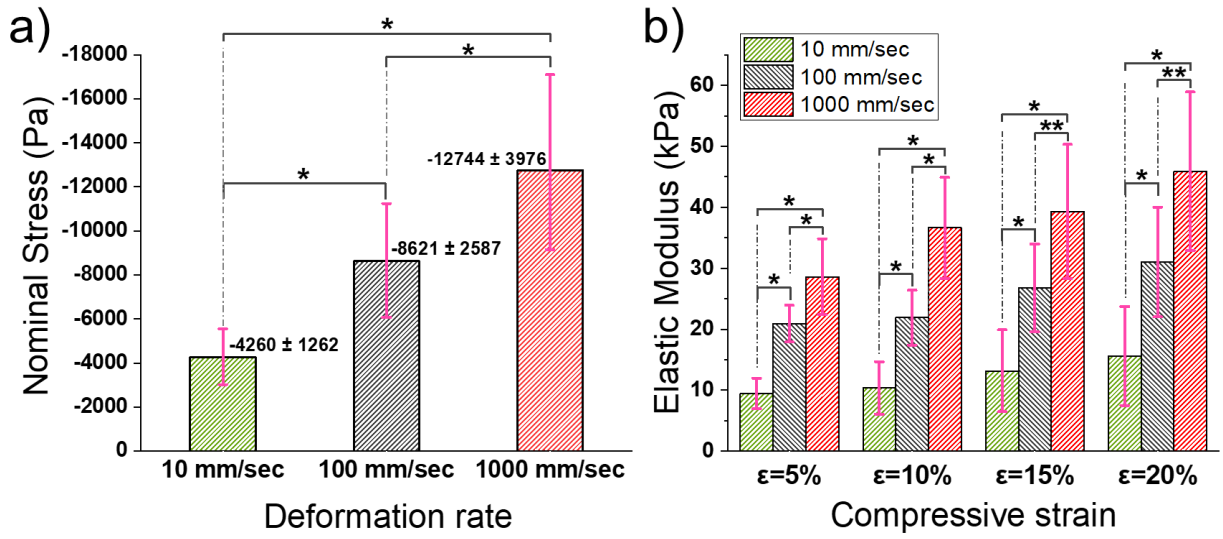

Figure 14. a) The maximum nominal stress (mean ± SD) determined at 30% compressive strain exhibits significant difference ($p < 0.01$) at various deformation rates. b) Also, the estimated elastic moduli as a measure of apparent stiffness increased by the rise in the strain level and the strain rate. * an ** represent statistical difference using ANOVA, with the significance level set at $p < 0.01$ and $p < 0.05$, respectively.

CHAPTER 4. RATE DEPENDENT CONSTITUTIVE MODELING OF BRAIN TISSUE[2]

4.1. Introduction

Accurate estimation and prediction of nonlinear behavior of human brain tissue lays the foundation to foresee the performance of such a complex organ in different health-related applications. This is specifically important in estimating the in-vivo intracranial behavior of this organ under TBI conditions. On this subject, a rigorous mechanical characterization of this soft biological tissue provides the groundwork for computational biomechanical studies in TBI analysis [20, 21, 120, 121]. For a rate-dependent material such as brain, it's necessary to select the right material properties matching the deformation rate in simulation [62], especially since TBI most often happens as a result of a highly dynamic load. It has been shown that for severe injury scenarios, brain will deform with high strain-rates up to 241 s^{-1} [19, 84]. Moreover, the effective time durations in higher frequency loads associated with TBI, are typically within the order of few milliseconds [84, 120]. Thus, for that very short-time span, the rate effect is a highly important feature to be considered in examining the behavior of brain.

It has been shown that severe brain injury, under blunt impact, normally occurs when the brain deforms with the strain-rate in range of 23 to 140 s^{-1} [84-86]. Farid et al [19] have simulated various impact and blast scenarios using FE analysis and have found that for mild to severe TBI the brain undergoes strain rates ranging from 36 to 241 s^{-1}. It should be noticed, that the effective time durations in higher frequency loads, such as impact-induced and blast-induced TBI, are respectively within the order of some and less than one millisecond [84, 120]. With such a short time duration, the rate effect is a key feature in studying the behavior of brain in TBI-related

[2]Hosseini-Farid, Mohammad, Ramzanpour, Mohammadreza, McLean, Jayse, Ziejewski, Mariusz, and Karami, Ghodrat. Mohammad Hosseini-Farid had primary responsibility for this chapter, and the rest of co-authors help him to proof-read this chapter for being submitted as a journal paper titled as "Rate dependent constitutive modeling of brain tissue".

loading. Substantial studies have focused on characterizing this viscoelastic behavior by using time dependent stress-strain relations [53, 122, 123]. Those studies employed the strain energy functions linearly coupled with time domain to implicitly address the strain rate effects at large strains [59]. Although this modeling provides an effective constitutive representation for short and long-term tissue behaviors, calibrating these linear viscoelastic models to test results from various rates is fairly challenging [62, 124]. In contrast, limited works in the literature have developed the nonlinear hyper-viscoelastic material models which were phenomenological in nature and have successfully reproduced the rate-dependent tissue responses over complex loading histories [53]. Although the hysteresis and dissipative characteristics were fully addressed by these models, their formulations are not supported in FE packages and are only useful if one is interested into self-developed numerical studies [125, 126].

The aim of this study is to elaborate some key features of characterizing the brain tissue at high strain rates paving the way for investigating the injury at the central nervous system under dynamical loads. Also, it is motivated to be a preliminary step in developing a predictive model for brain tissue over a large variety of strains and strain rates. In the experimental portion of this study, unconfined tests with compression velocities of 10, 100, 1000 mm/sec, were carried out on animal brain tissue for strain up to 30%. The nonlinear viscoelastic constitutive modeling is described and later the compatibility of this new model for being implemented in FE modeling have been examined. This study establishes an introductory step toward the development of a comprehensive experimental, theoretical, and computational procedure to enhance the FE analysis being employed in variety of biomechanical studies for traumatic brain injury.

4.2. Material and method

4.2.1. Constitutive modeling

4.2.1.1. Preliminaries

The parallel rheological framework allows the introduction of a nonlinear viscoelastic material model consisting of multifold networks connected in parallel [127]. As shown in Figure 15, the mechanical response of brain tissue can be decomposed into two parallel networks: hyperelastic equilibrium network (spring), specified as network A, and a rate-dependent viscoelastic behavior (spring-dashpot) defined as network B.

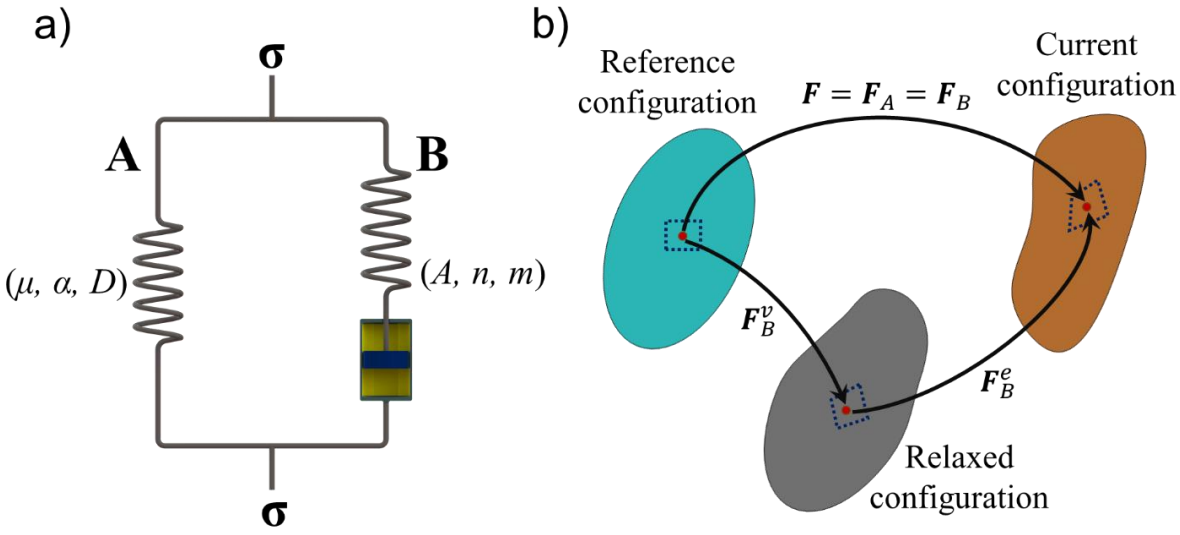

Figure 15. (a) Schematic representation of the proposed nonlinear viscoelastic model with two parallel networks consisted of an equilibrium network A and a viscoelastic network B, (b) and the multiplicative decomposition of the deformation for the rheological components of this model.

Considering the parallel continuity, for each network the deformation gradient tensor can be considered to be equal:

$$\boldsymbol{F} = \boldsymbol{F}_A = \boldsymbol{F}_B \tag{4}$$

where the deformation gradient $\boldsymbol{F}$ correlates the position of a point at deformed rate-dependent configuration $\boldsymbol{x}$ to its position at undeformed state $\boldsymbol{X}$ as:

$$\boldsymbol{F} = \frac{\partial \boldsymbol{x}}{\partial \boldsymbol{X}} = \nabla \otimes \boldsymbol{x} \tag{5}$$

The deformation gradient tensor introduces the right Cauchy-Green tensor $\boldsymbol{C}$ as $\boldsymbol{C} = \boldsymbol{F}^T.\boldsymbol{F}$. For the kinematic of characterization, in this study, the right Cauchy-Green tensor ($\boldsymbol{C}$) as well as the deformation gradient $\boldsymbol{F}$, are generally decomposed into volumetric contribution, characterized through the volume change (J) and a deviatoric (isochoric), volume-preserving contribution [61, 70]. In this regard $\overline{\boldsymbol{C}}$ and $\overline{\boldsymbol{F}}$ denote the deviatoric part of deformation and can be written in the form of,

$$\overline{\boldsymbol{C}} = J^{\frac{-2}{3}}\boldsymbol{C} \quad , \quad \overline{\boldsymbol{F}} = J^{\frac{-1}{3}}\boldsymbol{F} \tag{6}$$

where J, the Jacobian tensor, represents the change in volume between the deformed and undeformed state, introduced as $J = \det(\boldsymbol{F}) = \lambda^{1-2\nu}$, with λ being the stretch ratio. The large deformation of brain tissue and other soft biological tissues can be better characterized in terms of stretches ($\lambda=L/L_0$) instead of strains. In tension and compression, the stretch will be $\lambda=1+\varepsilon$ and $\lambda=1-\varepsilon$, respectively [128].

4.2.1.2. Elastic behavior

It is assumed that the equilibrium network response is purely elastic. Any form of strain energy function for expressing the behavior of soft materials can be employed to model the elastic (spring) response in each network. It is assumed that both networks have the same hyperelastic model [127], and the total strain energy, U_T, is obtained from the weighted summation of the energies of two networks

$$U_T = s_1 U(\boldsymbol{C}_A^e) + s_2 U(\boldsymbol{C}_B^e) \tag{7}$$

where $\boldsymbol{C}_A^e$ and $\boldsymbol{C}_B^e$ are the elastic right Cauchy-Green tensor in network A, and B. The stiffness ratio of networks, s_i, is a dimensionless material parameter indicating the ratio of shear modulus of network A and B and must satisfy s_1+s_2=1.

The total Cauchy stress response, $\boldsymbol{\sigma_T}$, of the system can be derived from the strain energy function as follows:

$$\boldsymbol{\sigma_T} = \boldsymbol{\sigma_A} + \boldsymbol{\sigma_B} = -pI + s_1 \left\{ 2\boldsymbol{F_A^e}.\frac{\partial U(\boldsymbol{C}_A^e)}{\partial \boldsymbol{C}_A^e}.(\boldsymbol{F_A^e})^T \right\} + s_2 \left\{ 2\boldsymbol{F_B^e}.\frac{\partial U(\boldsymbol{C}_B^e)}{\partial \boldsymbol{C}_B^e}.(\boldsymbol{F_B^e})^T \right\} \tag{8}$$

where p is the hydrostatic pressure that is determined by boundary conditions. In this manuscript, the *Ogden* strain energy function is used to evaluate the elastic response of both networks [129, 130]. The general (compressible) form of the *Ogden* strain energy function is:

$$U_{Ogden} = \sum_{i=1}^{N} \frac{2\mu_i}{\alpha_i^2}\left(\bar{\lambda}_1^{-\alpha_i} + \bar{\lambda}_2^{-\alpha_i} + \bar{\lambda}_3^{-\alpha_i} - 3\right)^i + \sum_{i=1}^{N} \frac{1}{D_i}(J-1)^{2i} \tag{9}$$

where $\bar{\lambda}_i$ is the deviatoric principal stretch introduced as $\bar{\lambda}_i = J^{\frac{-1}{3}}\lambda_i$, N is the material parameter number and μ_i, α_i, and D_i are material parameters. The initial shear modulus and bulk modulus for the *Ogden* model are given by $\mu_0 = \sum_{i=1}^{N} \mu_i$, and $K_0 = \frac{2}{D_1}$. In this study, the compressible form of *Ogden* hyperelastic model is employed to consider the compressibility effect. A pressure-volume test can be performed to calculate material compressibility data. This test characterizes the compressibility and volumetric deformation of the material by measuring the change in volume of the test sample due to a change in hydrostatic stress. For this study the pressure-volume data was

not available, therefore, the volumetric parameter (D_1) was assessed by using the calculated initial shear modulus, μ_0, and Poisson's ratio, v, as:

$$D = \frac{2}{K} = \frac{3(1-2v)}{\mu_0(1+v)} \tag{10}$$

According to Equation (10), the value for Poisson's ratio (v) is needed in order to determine the parameter D [69]. The value of v =0.49, which has been reported in substantial number of studies as the Poisson's ratio for the brain [1, 25], was applied to calculate the compressibility parameter of hyperelastic model.

4.2.2.3. Viscous behavior

The whole viscous behavior is taken into account by network B, which is modeled by assuming the multiplicative split of the deformation gradient into both elastic and viscous (inelastic) deformation (Figure 15):

$$\boldsymbol{F}_B = \boldsymbol{F}_B^e . \boldsymbol{F}_B^v \tag{11}$$

where the viscous part of the deformation, $\boldsymbol{F}_B^v$, represents the stress-free intermediate configuration of the network B [131]. The elastic component of deformation gradient, $\boldsymbol{F}_B^e$, is evaluated using its classical form, and $\boldsymbol{F}_B^v$ is calculated via time integration of the rate of creep deformation gradient in the viscoelastic network, $\dot{\boldsymbol{F}}_B^v$. In this regard, the velocity gradient in network B is given by

$$\boldsymbol{L}_B = \dot{\boldsymbol{F}}_B \boldsymbol{F}_B^{-1} \tag{12}$$

is similarly decomposed into the elastic and inelastic components given as:

$$\boldsymbol{L}_B = \left[\frac{d}{dt}(\boldsymbol{F}_B^e . \boldsymbol{F}_B^v)\right](\boldsymbol{F}_B^e . \boldsymbol{F}_B^v)^{-1} = \left[\dot{\boldsymbol{F}}_B^e . \boldsymbol{F}_B^v + \boldsymbol{F}_B^e . \dot{\boldsymbol{F}}_B^v\right](\boldsymbol{F}_B^v)^{-1}(\boldsymbol{F}_B^e)^{-1} \tag{13}$$

which can be written as

$$\boldsymbol{L}_B = \dot{\boldsymbol{F}}_B^e(\boldsymbol{F}_B^e)^{-1} + \boldsymbol{F}_B^e.\dot{\boldsymbol{F}}_B^v(\boldsymbol{F}_B^v)^{-1}(\boldsymbol{F}_B^e)^{-1} \tag{14}$$

and with respect to Equation (12), Equation (14) will be written in form of

$$\boldsymbol{L}_B = \boldsymbol{L}_B^e + \boldsymbol{F}_B^e.\boldsymbol{L}_B^v.(\boldsymbol{F}_B^e)^{-1} = \boldsymbol{L}_B^e + \tilde{\boldsymbol{L}}_B^v \tag{15}$$

Where

$$\boldsymbol{L}_B^v = \boldsymbol{D}_B^v + \boldsymbol{W}_B^v \text{ and } \tilde{\boldsymbol{L}}_B^v = \widetilde{\boldsymbol{D}}_B^v + \widetilde{\boldsymbol{W}}_B^v \tag{16}$$

It is assumed that the system possesses an unchanged rotation in the intermediate relaxed configuration regarding to the stress-free state (reference configuration) [132]. This assumption creates a unique unloading process, connecting the current configuration with the intermediate state and lead the viscous spin tensor to become zero, $\widetilde{\boldsymbol{W}}_B^v = 0$. So, the viscous rate of deformation in network B is constitutively represented by the symmetric part of the velocity gradient as $\tilde{\boldsymbol{L}}_B^v = \widetilde{\boldsymbol{D}}_B^v$. To describe the viscoelastic constitutive response of deformation gradient, the evolution of the creep part is considered ($\widetilde{\boldsymbol{D}}_B^v \equiv \boldsymbol{D}^{cr}$) [133]. Hence, through the multiplicative split of the deformation gradient for isotropic materials suggested by [134] the rate form of creep deformation gradient is re-written as [135, 136]:

$$\dot{\boldsymbol{F}}_B^v = (\boldsymbol{F}_B^e)^{-1}.\boldsymbol{D}^{cr}.\boldsymbol{F}_B^e.\boldsymbol{F}_B^v \tag{17}$$

where the $\boldsymbol{D}^{cr}$ is expressed based on creep potential $G^{cr} = G^{cr}(\boldsymbol{\sigma})$, proportionality factor, $\dot{\lambda}$, and the flow rule as:

$$\boldsymbol{D}^{cr} = \dot{\lambda}\frac{\partial G^{cr}(\boldsymbol{\sigma})}{\partial \boldsymbol{\sigma}} \tag{18}$$

In this model, we assume the creep potential is characterized by $\bar{\boldsymbol{q}}$**,** the equivalent deviatoric Cauchy stress, as $G^{cr} = \bar{\boldsymbol{q}}$, and also the proportionality factor is defined as $\dot{\lambda} = \dot{\bar{\varepsilon}}^{cr}$, where $\dot{\bar{\varepsilon}}^{cr}$ called the equivalent creep strain rate. Therefore, the flow rule will be given by

$$\boldsymbol{D}^{cr} = \frac{3}{2\bar{q}}\dot{\bar{\varepsilon}}^{cr}\bar{\boldsymbol{\sigma}} \quad \text{or} \quad \boldsymbol{D}^{cr} = \frac{3}{2\tilde{q}}\dot{\bar{\varepsilon}}^{cr}\bar{\boldsymbol{\tau}} \tag{19}$$

where $\bar{\boldsymbol{\sigma}}$ is the deviatoric Cauchy stress, $\boldsymbol{\tau} = J\boldsymbol{\sigma}$ is the Kirchhoff stress, $\bar{\boldsymbol{\tau}}$ is the deviatoric Kirchhoff stress, and $\tilde{q} = J\bar{q}$. The expression of equivalent creep strain rate, $\dot{\bar{\varepsilon}}^{cr}$, can be provided by models such as power-law [137], power-law strain hardening [138, 139], Hyperbolic-sine law [133], or either from Bergstrom-Boyce model [140]. In this manuscript, the $\dot{\bar{\varepsilon}}^{cr}$ is defined based on power-law strain hardening model in the form of

$$\dot{\bar{\varepsilon}}^{cr} = (A\tilde{q}^{\boldsymbol{n}}[(m+1)\bar{\varepsilon}^{cr}]^{m})^{\frac{1}{m+1}} \tag{20}$$

where $\bar{\varepsilon}^{cr}$ is the equivalent creep strain, and *A*, *m*, and *n* are the material parameters.

4.2.3. Parameter identification

All experimental data from three different loading rates of unconfined compression test for bovine brain tissue were simultaneously used for calibrating the material parameters. The nonlinear least-squares algorithm *lsqnonlin* in MATLAB was employed to identify the constitutive constants of proposed material model. To achieve a physically meaningful amount for material constants, the shear modulus μ_1, and *A* were constrained to have only a positive value. Also, the Equation (10) with the value of ν=0.49 stands as the constraints for determining the volumetric parameter, D_1. At each iteration this parameter was first calculated from estimated shear modulus

based on Equation (10), and then employed into optimization process. The objective function (χ^2) between calculated and measured stress was minimized as:

$$\chi^2 = \sum_{k=1}^{3} \sum_{i=1}^{N} \left(\sigma_i^{Exp} - \sigma_i^{Num}\right)^2 \tag{21}$$

where σ_i^{Num} and σ_i^{Exp} are the numerically predicted and experimentally measured true (Cauchy) stresses for three loading rates (k=1 to 3), and N is the number of data points.

To accelerate the parameter identification process, it is essential to assign a restricted range for each parameter value. Therefore, in this regards the parameters *m* and *n* was set to be calculated from range of [0.5,10] and [-1,0], respectively. Eventually, one set of material parameters which provided the best fit to the test results of brain at three measured rates were obtained.

4.2.4. Modeling parallel rheological framework in ABAQUS

Parallel rheological framework (PRF) is a finite-strain constitutive approach, which is referred to model non-linear viscoelasticity, Mullins effect and permanent set in polymers and elastomeric materials. The framework is made from the superposition of elastic or elastoplastic networks in parallel with one or multiple finite-strain viscoelastic network, N (Figure 16). This material model has been available in ABAQUS 6.13, and later versions (ABAQUS/Standard User's Manual, Version 6.13. Providence, RI). This framework can be consisted of arbitrary number of viscoelastic networks and is able to (1) use a hyperelastic material model to specify the elastic response; (2) be combined with Mullins effect to predict material softening; (3) incorporate nonlinear kinematic hardening with multiple back-stresses in the elastoplastic response; and (4) employ multiplicative split of the deformation gradient and a flow rule derived from a creep potential to specify the viscous behavior.

A variety of hyperelastic models (e.g. Mooney-Rivlin, Neo-Hookean, Ogden, Polynomial, Yeoh, etc.) in combination with various common creep laws (i.e. Power law, Strain hardening power law, Hyperbolic sine, Bergstrom-Boyce) or even with user-define creep model, led to introduce a diverse material models for representing the complex viscoelastic behavior for materials.

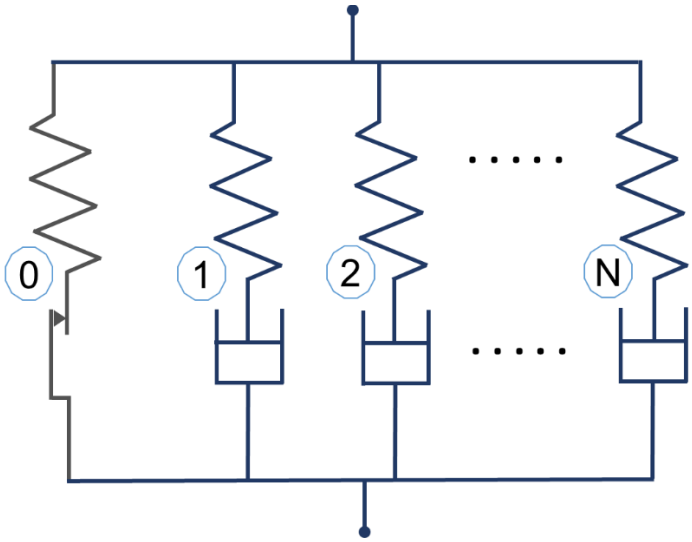

Figure 16. Schematic representation of the parallel rheological framework with N viscoelastic networks in parallel with an elastoplastic network.

4.2.4.1. Assign strain hardening power law model in ABAQUS

ABAQUS command ***Viscoelastic***, ***Nonlinear***, ***LAW=STRAIN*** was used to define the nonlinear viscoelastic model based on the strain hardening power law formulation. The strain hardening law is defined by specifying three material parameters: A, n, and m. To obtain physically reasonable behavior, A and n must be positive and $-1 < m \leq 0$. In this study, the calibrated material model is implemented as the form of the ABAQUS inp-file format that is shown in the following:

```
** MATERIALS
**
*Material, name=Ogden-10
*Hyperelastic, ogden
2941., 1.58,    1.37 e-5
**
*Viscoelastic, Nonlinear, NetworkId=1, SRatio=0.727, Law=strain
0.02429, 0.5875, -0.1828
```

4.3. Results

4.3.1. Determined rate-dependent material parameters

Table 8 presents the summary of determined material constants of proposed model for bovine brain tissue at three different rates. The calculated weighted factors (s_i) of hyperelastic stress in first and second networks were found to be 0.273 and 0.727, respectively. Both deviatoric (μ) and volumetric (D) constitutive parameters of *Ogden* hyperelastic model were evaluated. This nonlinear viscoelastic model provided an excellent constitutive representation in comparison with the test data for brain tissue (R^2=0.999). Figure 17 demonstrates the prediction of the proposed model for the mechanical response of brain tissue at three deformation rates of 10, 100, and 1000 mm/sec.

Table 8. Material parameters for the nonlinear viscoelastic model, calibrated for brain tissue at different deformation rates of 10, 100, and 1000 mm/sec.

Matter	Material Parameters							
	Hyperelastic Parameters			Rate Dependent Parameters				R^2_{Tot}
	μ_1 (Pa)	α_1	D_1 (Pa^{-1})	s	A ($Pa^{-n}s^{-m-1}$)	n	m	
Brain	2941	1.58	1.37 e-5	0.727	0.02429	0.5875	-0.1828	0.999

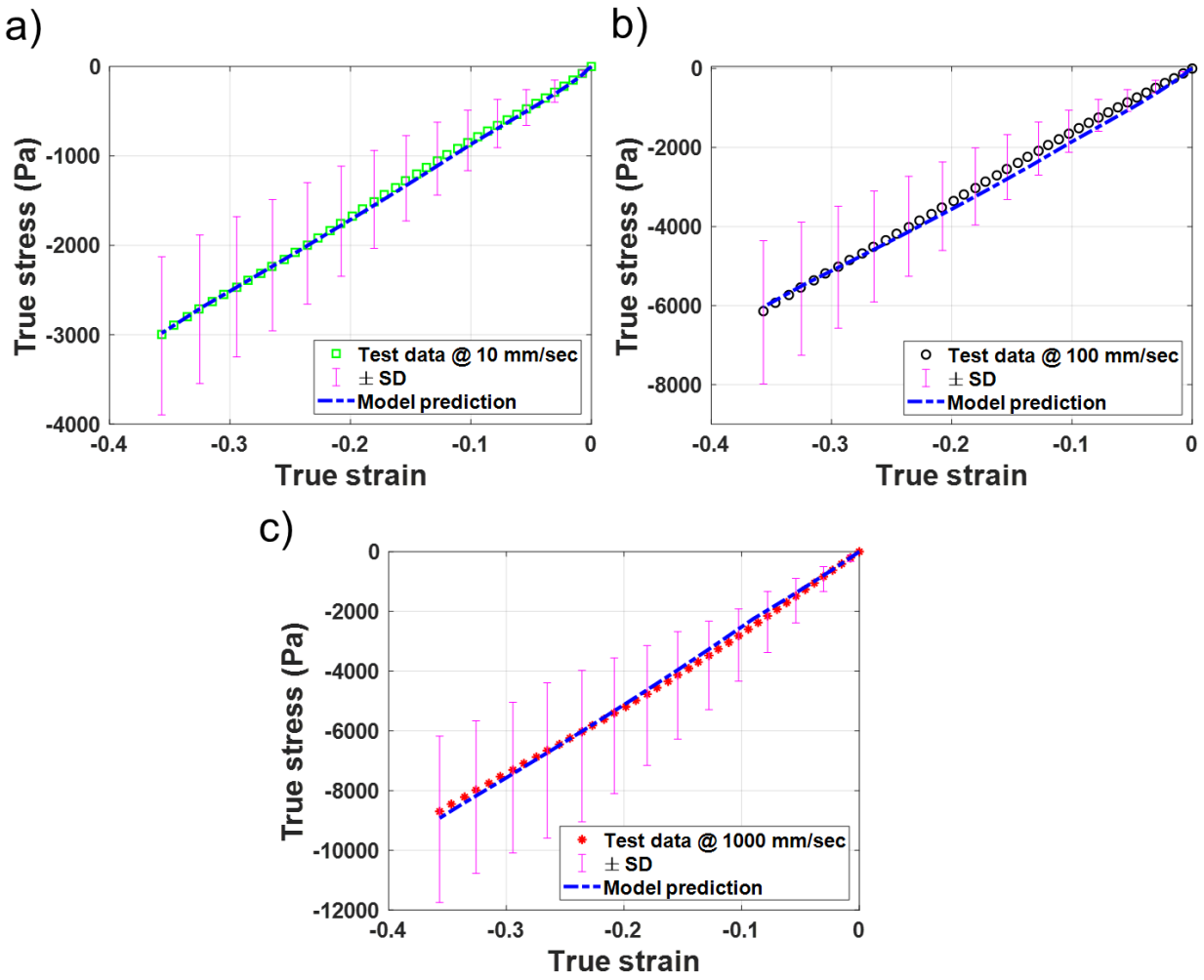

Figure 17. The comparison between experimental data and the determined mechanical response by nonlinear viscoelastic model for brain tissue at three different rates of: a) 10 mm/sec, b) 100 mm/sec, and c) 1000 mm/sec.

4.3.2. Model verification in finite element analysis

In order to check the validity of introduced model and the obtained material parameters for use in FE analysis, an inverse simulation of test procedure was carried out. Using ABAQUS/Standard 2016 code (ABAQUS Inc., Providence, RI), the same unconfined compression experiment was modeled by FE technique for a brain specimen. As shown in Figure 18-a, an axisymmetric geometry with a radius of 12.5 mm and height of 15 mm was generated resembling the brain specimen. A 4-node, axisymmetric quadrilateral, reduced integration, hybrid

element, which includes hourglass control was employed. On the left rotational axis, an axisymmetric boundary condition (U_1=0) was applied. A frictionless interaction was applied between platens and the top and bottom surfaces of brain sample. The constitutive constants presented in Table 8 were implemented as the material properties of tissue in the FE model. The upper platen was moved in vertical direction, compressing the specimen to 30% of its engineering strain with three deformation rates used in the experiments (i.e. 10, 100, 1000 mm/sec). A uniform uniaxial deformation along with homogenous radial expansion was observed for the brain sample as depicted in Figure 18-b. That leads to a fully uniaxial compression stress in vertical direction with insignificant transverse stress in radial direction (Figure 18-c).

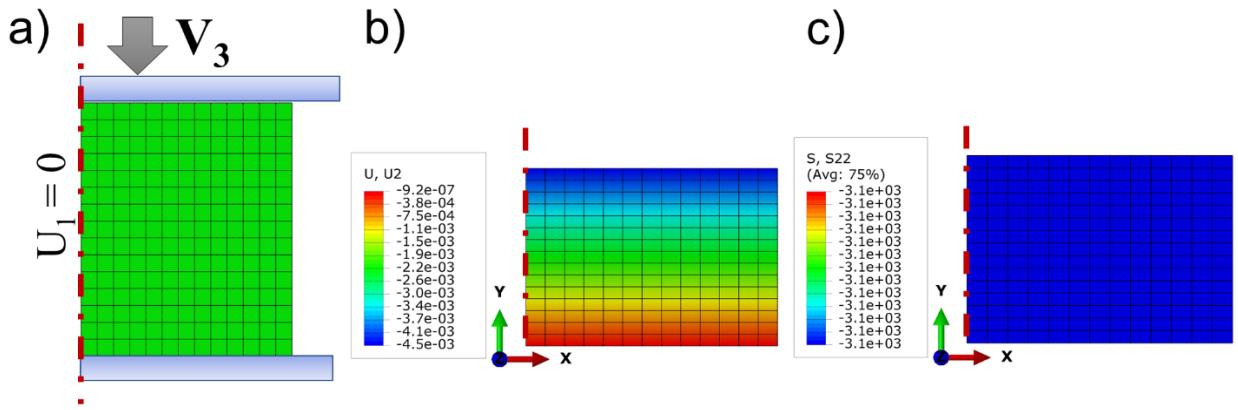

Figure 18. a) The developed FE model for unconfined compression test procedure of the brain specimen, b) the homogeneous deformation configuration of tissue at 30% of compressive strain, and c) the contour of Cauchy stress in "Y-Y" direction for the sample compressed up to ε=-0.3 strain with velocity of 10 mm/sec.

As depicted in Figure 19, very good agreements between experimentally measured stress-strain and FE computed results were achieved for brain sample at three different tested speeds. In order to obtain the nominal stresses in FE analysis shown in Figure 19, the calculated reaction force for upper platen was divided by the initial top area of brain sample. Also, additional simulations with velocities in the range of calibrated rates (10~1000 mm/sec) were chosen to further examine the validity of the model and determined material parameters. In this regard, the

FE simulations were performed for the compressive speeds of 50, 250, 500, and 750 mm/sec, and the computed tissue response for each rate is presented in Figure 19. This rate-dependent model gives proper predictions of the tissue response for other intermediate rates. The calculated mechanical responses in Figure 19, and the predicted deformed configuration in Figure 18, were in full agreement with experimental results, verifying the validity of the proposed material model to reproduce the tissue viscoelastic behavior.

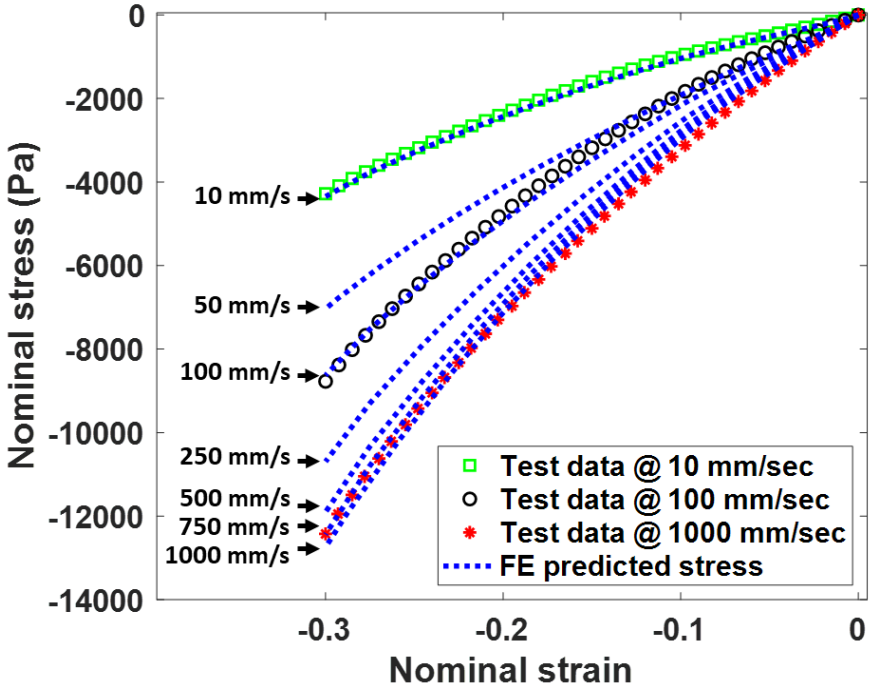

Figure 19. The predicted nominal stress by FE analysis of brain sample with different deformation rates using the material constants presented in Table 8.

4.4. Discussion

The main objective of this study was to verify and calibrate the rate-dependent model on animal brain, and further pave the path for determining the most accurate material properties of human brain. In this regard, the rate dependent mechanical behavior of bovine brain tissue has been investigated under unconfined compression test at intermediate to high rates. Besides the observation of the stress-rate dependency, we found the mechanical response varies nonlinearly

with the change in strains, as well as the strain rates. Figure 14 reveals how the peak stress and the apparent elastic modulus of the bovine brain varies as the rate changes. Based on parallel rheological framework approach, a single phase nonlinear viscoelastic model was developed and calibrated with the experimental result. The averaged experimental results at three different rates were employed to determine one set of material parameters. The excellent agreement between the numerically calculated and experimentally measured stresses (Figure 13) confirmed that the proposed constitutive model is fully capable to characterize the rate-dependent behavior of brain tissue under compression deformation.

In the literature of biomechanics of the brain, some studies have been devoted to characterizing the rate-dependent mechanical properties of this tissue. Pamidi and Advani [141] derived a nonlinear constitutive relation based on power energy function. They calibrated their model using the reported in-vitro test results of [36] and obtained a good numerical prediction of human brain tissue under compression. Mendis et al. [122] have developed a large-strain linear-viscoelastic model to be used in FE modeling of brain tissue. They incorporated the Prony series into the Mooney-Rivlin strain energy function and determined the time-dependent form of hyperelastic coefficient. Miller and Chinzei [115] implemented a similar hyper-viscoelastic model to characterize the viscoelastic behavior of porcine brain tissue. They introduced a unique procedure to calculate the material constants over three different low to medium rates. Hrapko et al. [142] captured the nonlinear mechanical response of brain under the shear response of tissue, using a new differential viscoelastic model that developed based on Mooney–Rivlin viscoelastic network and included 16 material parameters. In order to capture the rate-dependent behavior at finite viscosity and deviatoric and volumetric plasticity of the brain tisuue, El Sayed et al. [54] developed a nonlinear elastic-visco-plastic material model and verified their model with tissue

response under uniaxial compression and tension test up to 50% nominal strain. Also, Prevost et al. [125] have investigated the dynamic behavior of porcine brain tissue at nominal strain rates of 0.01, 0.1 and 1 s^{-1}. They developed a rheological based constitutive model to capture the effects of compressibility, hysteresis conditioning, the rate dependency, and short and long-term viscoelastic behaviors of the tissue. Although, their comprehensive model with eight parameters was proven to predict the behavior of tissue at tension, and relaxation modes as well, still it has a limited ability for being used in FE software packages. Recently, Haldar and Pal [126] developed a rate-dependent anisotropic constitutive relation and numerically modeled the brain tissue under large deformation. They have shown that their rigorous phenomenological model was able to account for the rate dependency, nonlinear viscoelasticity, anisotropy, and tension-compression asymmetry behavior of the tissue.

Although the model proposed in this study accounts for the compressibility effect of tissue deformation, it has fewer material constants to be determined in contrast to existing constitutive models. This feature led to a relatively faster model calibration process and less computational cost. Also, it was shown that the developed nonlinear viscoelastic model here, can be directly implemented in commercial FE code (e.g. ABAQUS, see Appendix A for more details) to perform the FE simulations with no need for a material subroutine. In this regard, the main features of this model in comparison with most common viscoelastic models used to characterize the rate dependent behavior for brain tissue, are presented in Table 9

Table 9. A summary of most well-known rate dependent constitutive models have been developed to characterize the brain viscoelastic behavior in comparison to the model proposed in this study.

Ref. study / Model	Key feature	# of Material constants	Compressibility	FE availability
Pamidi and Advani [141] / power energy function	Rate dependent	3	N.A.	N.A.
Mendis et al. [122] and Miller and Chinzei [115] / linear hyper viscoelastic	Time dependent	8	N.A.	Yes
Bergström and Boyce [140] / nonlinear hyper viscoelastic	Rate dependent	8	Yes	Yes
Hrapko et al. [142] / nonlinear viscoelastic	Rate dependent	16	N.A.	Yes*
El Sayed et al. [54] / nonlinear elastic-visco-pelastic	Rate dependent	13	Yes	Yes**
Prevost et al. [125] / nonlinear hyper viscoelastic	Rate dependent	8	Yes	N.A.
Haldar and Pal [126] / nonlinear hyper viscoelastic	Rate dependent	8	N.A.	N.A.
This study / nonlinear hyper viscoelastic	Rate dependent	7	Yes	Yes

* This model is available in the explicit Finite Element code MADYMO [143].

** It seems the model has not becoming available in commercial FE packages, yet [144].

The present study is an essential step towards the development of a constitutive model able to predict the tissue behavior during large deformation at arbitrary loading velocities. As the limitations of current study, it should be noted that the tissue was characterized for only uniaxial deformation (unconfined compression) over a range of intermediate to high rates. If the material parameters are determined for one particular deformation mode such as compression, it may not exhibit adequate behavior for other deformation modes such as tension, shear or other loading combinations. One other limitation of this study is the estimation of the material parameters from

a mixed white and gray matter of the brain tissue. The results, therefore, are only valid for such a composite and can be useful in approximate modeling of the brain [51, 59]. Also, we have assumed an isotropic structure and employed the average mechanical properties of the tissue in the determination of material parameters; however, this procedure is accepted in obtaining such parameters which are useful in evaluating an approximate behavior of the tissue. Moreover, in some studies it was postulated that the anatomical location [145, 146] and the direction [43, 117] of extracted brain samples had insignificant effect on the tissue response.

As a suggestion for future work, further model refinement is required to address the time dependent viscoelastic behavior associated with the biphasic inherent of brain tissue at intermediate to high deformation rate regime. This single-phase viscoelastic model provided here, was a first step towards achieving this goal, and it is needed to introduce a viscoelastic biphasic constitutive model to demystify more phenomenological behavior of brain tissue. It is suggested in the next step, that brain tissue is treated as a porous medium, composed of a solid matrix with interstitial fluid, and the significant role of fluid diffusion in the brain tissue is taken into account. On this subject, the future biphasic constitutive model should be able to capture the tissue rate-dependent behavior resulting from the coupled dynamical interactions between the mechanical response of the solid phase and fluid flow.

4.5. Conclusions

This study demonstrates the in-vitro results for bovine brain tissue in unconfined compression experiments up to 30% nominal strain over three orders of deformation rate magnitude (10 to 1000 mm/sec). The significant effects for rate-dependent behavior of this soft biological tissue was observed. It was shown that with an increase in deformation rate, the mechanical features i.e. the nominal stress and apparent elastic moduli were also increased. A rate

dependent constitutive relation was introduced and simultaneously calibrated with the measured data from three various deformation rates. The excellent correlations between the experimental, theoretical, and computational results has indicated that the proposed model is fully able to characterize brain tissue behavior and be employed in FE simulation. This study presented a promising constitutive model and a successful technique to capture the rate-dependent material properties, a complex inherent characteristic of brain at intermediate to high strain rates.

CHAPTER 5. A PORO-HYPER-VISCOELASTIC RATE-DEPENDENT CONSTITUTIVE MODELING FOR THE ANALYSIS OF BRAIN TISSUES[3]

5.1. Introduction

A realistic representation of the constitutive response for brain tissue under various loading-boundary conditions would be a prerequisite for performance prediction. In order to meticulously predict the mechanical behavior of this tissue, one needs mathematical models reflecting its multiphasic nature and working under large deformations assumption, e.g. under an induced anisotropic flow [147, 148] and regional and orientation-dependent stiffness, especially for white matter [44, 46, 48]. Moreover, several parameters make it cumbersome for precise prediction of the brain mechanical behavior. In general, the most important ones are the complex heterogeneity [149], an anisotropic structure [75, 76], the geometrical shape and being ultra-softness [150, 151], dispersion state of axons and blood capillaries [152-154], and the interfacial interaction between several tissue components [14, 155]. The single-phasic constitutive models fail to describe a profound understanding of interplay between tissue constituents, (e.g. cells, extracellular proteins, negatively charged molecules, extracellular or interstitial fluid, blood vessels, blood plasma, and etc.) which is essential in numerical analysis of medical treatments. To date, a limited number of multiphasic models have been devoted to studies of this porous medium, motivated us to delve into underlying modeling of this substance.

From the macroscopic point of view, the brain is an extremely soft solid material and its mechanical behavior is greatly influenced by the fluid phase [14]. Both the intracellular and extracellular fluid contents constitute up to 88 percent of the brain volume fraction [156, 157].

[3]Hosseini-Farid, Mohammad, Ramzanpour, Mohammadreza, McLean, Jayse, Ziejewski, Mariusz, and Karami, Ghodrat. Mohammad Hosseini-Farid had primary responsibility for this chapter, and the rest of co-authors help him to proof-read this chapter for being submitted as a journal paper titled as "A poro-hyper-viscoelastic rate-dependent constitutive modeling for the analysis of brain tissues".

This substantial liquid content would suggest modeling this soft biological tissue as a biphasic material, although many of its mechanical characteristics have been widely considered within the framework of monophasic continuum mechanics by ignoring the influences corresponding to the possible relative motion of the interstitial fluid through the solid tissue constituents [36, 53, 58, 67, 68]. In addition, the high bulk modulus of fluid (mainly water) implies very weak compressibility to the tissue, and this fact is frequently taken as a proof for tissue incompressibility. This widely assumed paradigm in many studies of brain, does not match the evidence of many experimental studies [40, 125]. Furthermore it does not mimic the exact behavior of confined brain in the skull [39], and is not involved in several applications introduced by the modern theory of porous media in biomechanics [158-160]. Therefore, it is necessary to introduce a continuum based constitutive model which accounts for the fluid diffusion and the intrinsic properties of the solid-fluid phases as well as their interaction.

In the microstructure view, the fluid phase surrounds the tissue cells and fills the interstices and void spaces of the brain tissue [155]. As is demonstrated in Figure 20, in the context of continuum biphasic modeling and theory of porous media, brain tissue is treated as a porous medium, composed of a solid matrix with interstitial fluid. This interstitial fluid (extracellular fluid) accounts for about 20% of the brain parenchymal volume, and its diffusion-based function assists nutrient transportation, and waste purging from the cells [161]. The fluid phase plays a prominent role in the deformability of this hydrated biological tissue and is mostly considered as cerebrospinal fluid with properties of close to water. The biphasic model provides a pronounced view into the coupled dynamical interactions between the mechanical response of the solid phase and fluid flow. Some phenomenological observation of this tissue can be interpreted and exhibited by this theory. Stracuzzi et al. [159] proposed that the ability of fluid to move through the

interstitial space and across the cellular network, facilitates the reversible volume changes of tissue through fluid exchange within the tissue cell network.

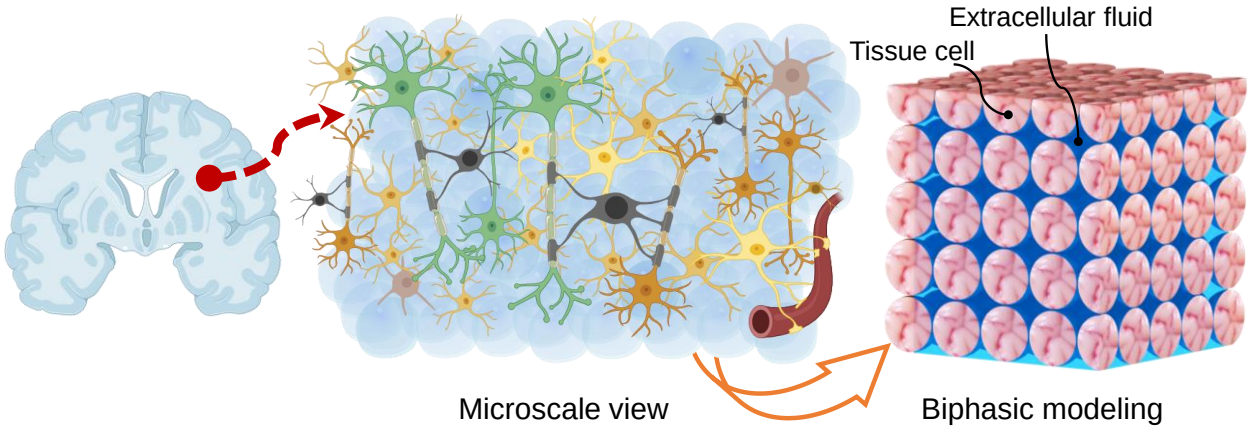

Figure 20. Schematic microscale view of brain tissue consisting of cells, extracellular or interstitial fluid, blood vessels, and etc., demonstrated as a soft porous matter expressed by a biphasic model including solid phase composed of the cell bodies, and interstitial fluid that filled up the void spaces.

Most biphasic studies proposed an isotropic linear [162-165] or hyperelastic [166] material for modeling the solid matrix of the brain. Wagner and Ehlers [167] introduced an anisotropic poro-hyperelastic, two-component model for monitoring the dispersion of therapeutic agents as a chemical solution within the interstitial fluid. Inclusion of interstitial hydrodynamic pressure for the brain subjected to neurosurgical loading conditions have been investigated in an experimental work by Miga et al. [168]. They employed a poro-elastic material model and reported a transient interstitial pressure gradient with brain deformation. Although they have claimed this type of suggested porous model can represent a lean primary time-dependent response under short-term regimes, the effects of viscoelasticity should have been considered in a more comprehensive material model. Inclusion of the viscous contributions at large deformation to account for a better representation of rate-dependent behavior for both solid and fluid phases has been the main motivation of the authors of this study to introduce a hyper-viscoelastic constitutive model.

The goal of the current contribution is twofold: (I) It provides the major aspects of the viscoelastic biphasic modeling used for characterizing brain tissue, as a necessary step towards developing the rate-dependent material properties required for studying the mechanical responses of brain tissue in transient analysis. (II) It thus widens our perception of the mechanical behavior for this multicomponent biological tissue in the global and local scales, and the microstructural interaction between solid-fluid phases. This can lead to more insight of fluid diffusion within the cellular network and eventually introduce a new feasible mechanism of damage in brain substructure caused by coupled tissue deformation and internal fluid flow.

5.2. Material and method

5.2.1. Biphasic formulation

The biphasic mechanical model for a saturated porous material originates from the continuity of the mass and the conservation of linear momentum. The continuity equations for the solid and fluid phases read [169]:

$$\frac{\partial(1-\phi)}{\partial t} + \nabla.[(1-\phi).v_s] = \dot{m} \tag{22}$$

$$\frac{\partial \phi}{\partial t} + \nabla.\left(\phi \boldsymbol{v}_f\right) = \dot{q} \tag{23}$$

where v_s and v_f are the velocities of solid and fluid phases, respectively. $\dot{m}$ and $\dot{q}$ are the rate of mass and fluid flux, and the material porosity denoted by ϕ, which indicates the volume fraction of pore space, is calculated by [166]:

$$\phi = 1 - \frac{1-\phi_0}{J} \tag{24}$$

where ϕ_0 is the initial porosity, and J is Jacobian of the deformation calculated as $J = \det(\boldsymbol{F})$. Equation (24) shows that the void space can change with the volume change and the variation of

fluid pressure. For the conservation of momentum in a porous medium, the intrinsic mass density (ρ_s, ρ_f), the external body force density ($\boldsymbol{b}_s$, $\boldsymbol{b}_f$), and the rate of linear momentum exchange ($\boldsymbol{R}_s$, $\boldsymbol{R}_f$) between two solid and fluid phases are described as [170]:

$$\frac{\partial[(1-\phi)\,\rho_s \boldsymbol{v}_s]}{\partial t} + \nabla.[(1-\phi)\,\rho_s \boldsymbol{v}_s \boldsymbol{v}_s] - \nabla.\boldsymbol{\sigma}_e - (1-\phi)\,\rho_s \boldsymbol{b}_s = \boldsymbol{R}_s \tag{25}$$

$$\frac{\partial[\phi\,\rho_f \boldsymbol{v}_f]}{\partial t} + \nabla.[\phi\,\rho_f \boldsymbol{v}_f \boldsymbol{v}_f] - \nabla.\boldsymbol{\sigma}_f - \phi\,\rho_f \boldsymbol{b}_f = \boldsymbol{R}_f \tag{26}$$

where $\boldsymbol{\sigma}_e$ and $\boldsymbol{\sigma}_f$ are the solid and fluid stress tensor. A closed mass system and the momentum balance between two compartments must read

$$\nabla.\Big((1-\phi)\boldsymbol{v}_s + \phi \boldsymbol{v}_f\Big) = \dot{m} + \dot{q} = 0 \tag{27}$$

$$\boldsymbol{R}_s + \boldsymbol{R}_f = \boldsymbol{0} \tag{28}$$

Darcy's law is then implemented to determine the fluid velocity based on pore pressure, *p*, and the hydraulic conductivity (permeability) of the interstitial space, *k*, as:

$$\phi\big(\boldsymbol{v}_f - \boldsymbol{v}_s\big) = -k\nabla p \;\; \Rightarrow \;\; \boldsymbol{v}_f = \frac{-k\nabla p}{\phi} + \boldsymbol{v}_s \tag{29}$$

The above equation shows the contribution of the solid matrix displacement ($\boldsymbol{v}_s = \partial \mathbf{u}/\partial t$) to the flow of interstitial fluid within pores spaces [27]. These relations clearly state that the fluid flow is a function of the velocity of solid network deformation, the pore pressure, and the physical properties of such porous matter, i.e. the porosity and hydraulic conductivity. The hydraulic conductivity, a key intrinsic property prescribing how easily the liquid phase can flow through the porous network, is itself a function of pore geometries and the fluid physical properties [171]. Additionally, the pore pressure varies with the changes of velocities, indicating the rate-dependent

nature of fluid phase. The theory of biphasic [172, 173] imposes the total stress tensor, $\boldsymbol{\sigma}_T$, for fully saturated soft tissue that is resulted by the summation of the stress tensor in fluid phase, $\boldsymbol{\sigma}_f = -p\boldsymbol{I}$ ($\boldsymbol{I}$ is the identity matrix), and the effective stress tensor in the solid matrix, $\boldsymbol{\sigma}_e$ [174]:

$$\nabla . \boldsymbol{\sigma}_T = 0 \quad \Rightarrow \nabla . (\boldsymbol{\sigma}_e - p\boldsymbol{I}) = 0 \tag{30}$$

where the effective stress in solid phase, $\boldsymbol{\sigma}_e$, is determined by strain energy function, W, deformation gradient, $\boldsymbol{F}$, and J as

$$\boldsymbol{\sigma}_e = \frac{1}{J}\boldsymbol{F}.\frac{\partial W}{\partial \boldsymbol{F}} \tag{31}$$

The fully saturated condition is assumed for the porous medium of brain tissue. That means all void and pore spaces are filled up with the fluid. The void ratio e of the porous material denotes the ratio of the void volume, V_V, to filled solid volume, V_S, is closely related to porosity:

$$e = \frac{V_V}{V_S} \quad \Rightarrow \quad e = \frac{\phi}{1-\phi} \tag{32}$$

As proposed by Nagashima et al. [175], the initial void ratio (e_0) was set to be 20%. Since the CSF is mostly composed of water [176], the fluid phase is treated as water with specific weight (γ) of 9.741 (kN/m^3) [69].

While we deal with an incompressible fluid phase, the solid matrix needs to be modeled as compressible material to exhibit a more realistic deformation. Therefore, to express the mechanical behavior of solid phase, the compressible Ogden constitutive model [129] was employed. This model has been widely used as a strain energy function to describe nonlinear mechanical behavior of soft biological tissue, including brain tissue [43, 58, 59]. Moreover, recent study has shown that among most common strain energy functions, only one-term Ogden model exhibited a promising

constitutive representation for the tissue at different loading modes [43]. The general compressible strain energy function of this model was previously presented in Equation (9), in Chapter 4.

To introduce a hyper viscoelastic model and correlate the rate-dependency behavior for the solid phase, a linear expression of time-dependent viscoelasticity is incorporated into the *Ogden* strain energy function. In this regard, the Prony series, the most extensively used mathematical form to demonstrate this behavior is employed as [53]:

$$G(t) = 1 - \sum_{k=1}^{M} g_k(1 - e^{-t/\tau_k}) \tag{33}$$

where $G(t)$ is the dimensionless shear relaxation modulus, g_k and τ_k are relaxation coefficients and characteristic times. Here the viscoelasticity of the solid phase is indicated as a viscous component that is linearly applied to the elastic constants in the energy function. Therefore, the constants in the strain energy function at Equation (9) for the mentioned hyperelastic model are rewritten as:

$$\mu_i^R(t) = \mu_i^0\left(1 - \sum_{k=1}^{M} g_k(1 - e^{-t/\tau_k})\right) \tag{34}$$

$$D_i^R(t) = D_i^0\left(1 - \sum_{k=1}^{M} g_k(1 - e^{-t/\tau_k})\right) \tag{35}$$

5.2.2. Parameter identification

5.2.2.1. Optimization procedure of material parameters

Typically, for determining the model parameters, the mathematical equation which describes the physical behavior of a material is fitted into the results of the experiment. Sometimes, the regular curve fitting might have consequence in numerical results for model parameters that are physically unsound, although they are mathematically correct. Recently, some researchers have

used the numerical analysis using FE methods of experimental testing to calibrate single-phasic hyperelastic material parameters [80, 177-179]. In this approach, the constitutive constants are determined by mimicking the complexity of the experimental protocol and are calibrated through an optimization technique. This technique provides a more accurate determination of the material parameters [180, 181]. There are some conditions that require to be checked for the obtained material constants. For instance, the Drucker stability condition can be used during the model calibration or as a post-processing step for evaluating the physical meaning of obtained constitutive parameters [182]. In the work presented here, the stability ranges of strain that satisfied this condition are reported for all regions of the brain.

The interphase's interaction is governed by Darcy's law (Equation (29)), hence, the contribution of both phases is involved in the mechanical response of the tissue [69, 183]. The calculated parameters from one rate, e.g. at 10 mm/sec may exhibit significant deviation in estimating material behavior at other rates such as, 100 or 1000 mm/sec, and vice-versa. So, the combined experimental results from three different rates must be employed simultaneously, for calibrating the rate-dependent material constants valid for the specified range of rates.

The hyper-viscoelastic model combined of one-term *Ogden* hyperelastic model along with two-term Prony series (g_1, τ_1, g_2, τ_2) were assigned to represent the behavior of solid phase (Equations 9, 34, 35). To find proper values of all those material parameters, FE simulations were carried out in the context of genetic algorithm optimization method with the input parameters of μ_1, α_1, D_1, g_1, τ_1, g_2, τ_2 , using ABAQUS/Standard 2016 code (ABAQUS Inc., Providence, RI). The Equation (10) with the value of ν=0.49 stands as the constraints in determining the volumetric parameter, D_1. At each iteration this parameter is first calculated from estimated shear modulus based on Equation (10), and then employed into optimization process. The genetic algorithm

optimization method minimizes the error (*Err*) between computed and measured force history given as:

$$Err = \sum_{k=1}^{3}\sum_{i=1}^{N}\left(\frac{F_i^{Exp} - F_i^{Comp}}{F_i^{Exp}}\right)^2 \tag{36}$$

where F_i^{Comp} and F_i^{Exp} are the computationally predicted and experimentally measured force at three different rates (k=1 to 3), and N is the number of data points. The flowchart of this procedure is shown in Figure 21. For each iteration (generation), the force-stretch curve is computed by FE simulation and compared with measured test data. The optimization procedure continues to create a generation that the change in objective function gets smaller than function tolerance level ($t=10^{-5}$).

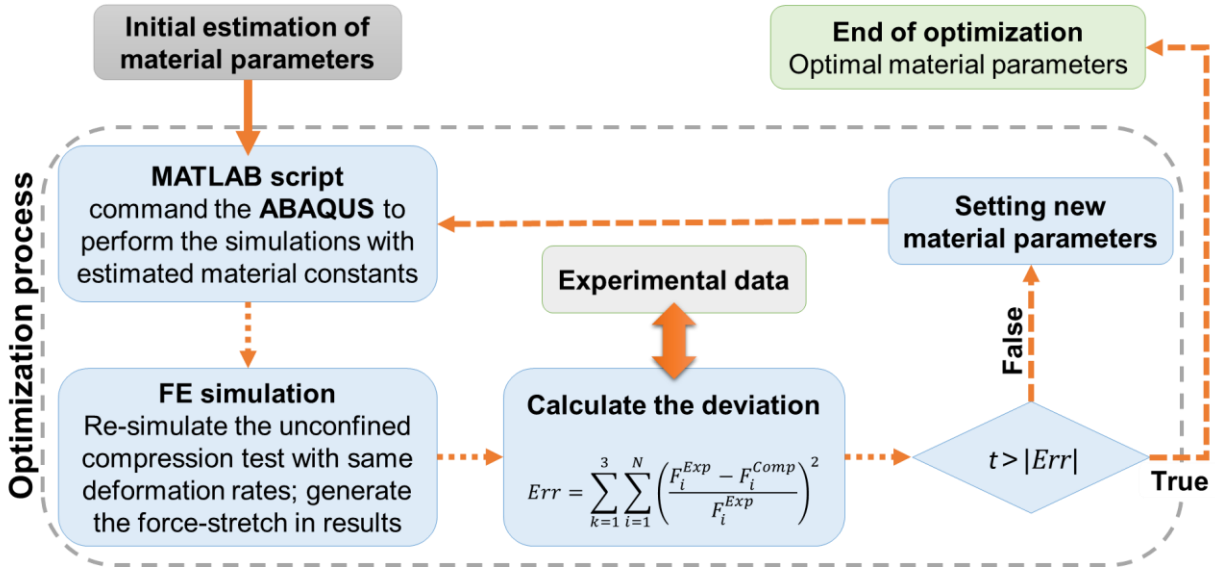

Figure 21. Flowchart of the optimization procedure for determining the optimum poro-hyper viscoelastic material properties for brain tissue at three rates.

5.2.2.2. Inverse finite element analysis

To determine the material constants, FE modelling was developed and set to minimize the objective function for the difference between simulation results and test data. In this approach, the

material constants were optimized through an iterative simulation and best fitted model parameters that represent the tissue response were identified. In this way the complexity of the problem physics has received more consideration than in simple numerical or analytical methods. A mesh study was performed, prior to embarking into poro-hyper-viscoelastic modelling. The geometry of brain samples was discretized into 11784 linear hexahedral elements of type C3D8PH (An 8-node brick, trilinear displacement, trilinear pore pressure, and hybrid). The frictionless interactions between loading platen faces and top and bottom surfaces of the brain sample are implemented resembling the unconfined condition. In the developed FE models, a free drainage boundary condition (pore pressure = 0) was implemented to the all outer surfaces allowing the fluid content to drain out of the brain specimen. The computational simulations of testing procedure for brain specimen were carried out by transient analysis at three different compression velocities. As depicted in Figure 22, at each velocity (i.e. v= 10, 100, 1000 mm/sec), the sample was compressed to 30% of its engineering strain (or λ=0.7).

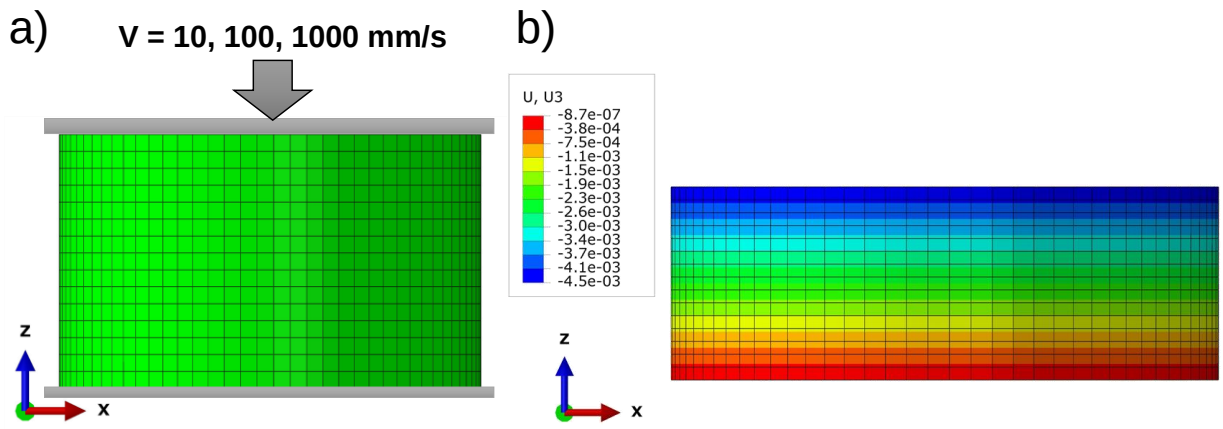

Figure 22. a) The discretized FE Model of brain specimen employed to re-simulate the uniaxial unconfined compression with same test velocities, and b) the deformed configuration of the tissue at compressive stretch of 0.7.

5.3. Results

5.3.1. Rate-dependent material parameters of the tissue

The procedure of determining material parameters of the proposed biphasic constitutive model, is described in Appendix A. Table 10 presents the summary of evaluated material constants for the proposed biphasic model for bovine brain tissue at three different rates. Since the pore spaces are occupied by an incompressible fluid, the solid matrix will be responsible for all the compressible deformations. Thus, both the deviatoric (μ) and volumetric (D) constitutive parameters of *Ogden* hyperelastic model were evaluated for the solid phase. This viscoelastic biphasic model provided a very good constitutive representation in comparison with the test data for brain tissue (R^2=0.96). Moreover, Figure 23 illustrates the prediction of the proposed model for the mechanical response of brain tissue at three deformation rates of 10, 100, and 1000 mm/sec. In this figure, the reaction forces were calculated by computational analysis of the unconfined compression for a sample, using the obtained material constants provided in Table 10.

Table 10. The viscoelastic biphasic material parameters, calibrated for bovine brain tissue at different deformation rates of 10, 100, and 1000 mm/sec.

Matter	Solid phase							Fluid phase			R^2_{Tot}
	Deviatoric Parameter		Volumetric Parameter	Time Dependent Parameter							
	μ_1 (Pa)	α_1	D_1 (Pa^{-1})	g_1	τ_1 (s^{-1})	g_2	τ_2 (s^{-1})	k (m/s)	γ (kN/m^3)	e_0	
Brain tissue	1810	2.5	$2.2\ 10^{-5}$	0.36	0.8	0.46	0.017	$1.57\ 10^{-8}$	9.741	0.2	0.96

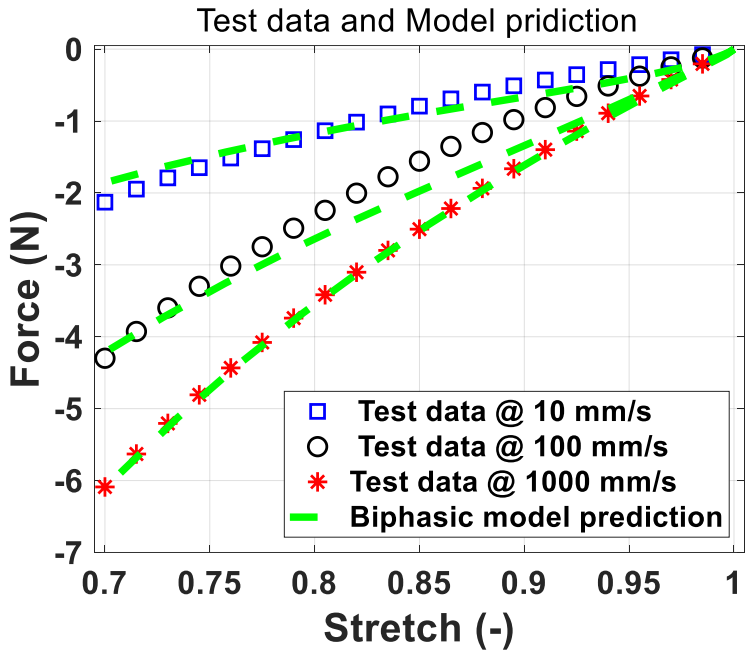

Figure 23. The comparison between experimental data and the predicted mechanical response by viscoelastic biphasic model for brain tissue at three different rates.

The variation of fluid hydrostatic pressures and stresses in the solid matrix at two locations (center and outer surface of sample), caused by applied compressive deformation with speed of 10 mm/sec, are depicted in Figure 24 a, b. This figure shows that for a compressed specimen, how the solid and fluid responses contributes to the global reaction of this soft porous tissue. It is worth emphasizing that pore pressure of interstitial fluids attained positive values under compression loading. As free drainage boundary condition was implemented on all the outer surfaces, the fluid contents drained out of the brain specimen and the pore pressure becomes zero ($p = 0$). This fact was noticeably reflected in the developed pore pressure gradients presented in the Figures 25.

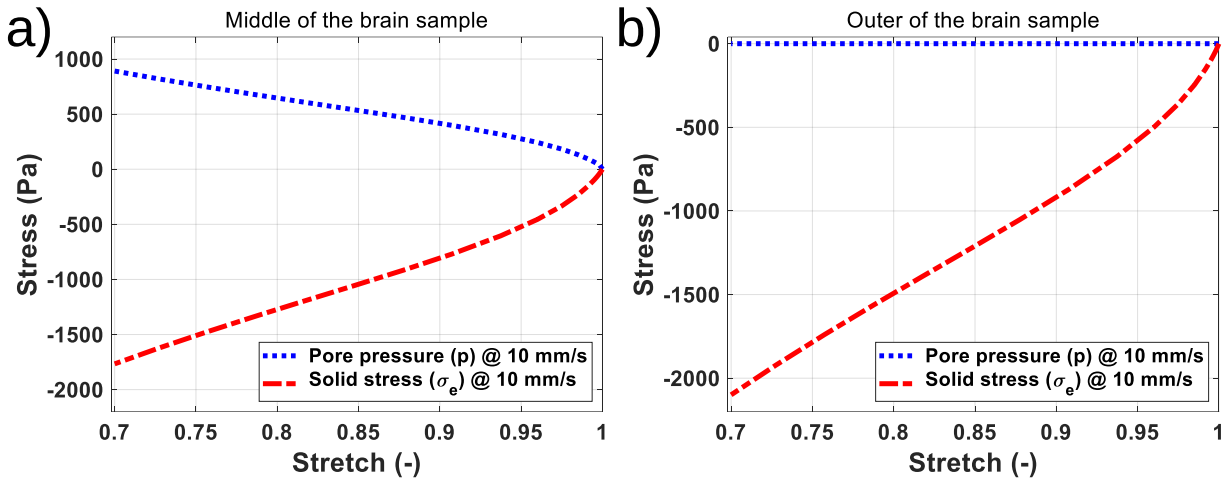

Figure 24. Contribution of pore pressure, p, and solid stress, σ_e, versus stretch, predicted for: a) middle, and b) outer surafce of brain sample under compressive deformation.

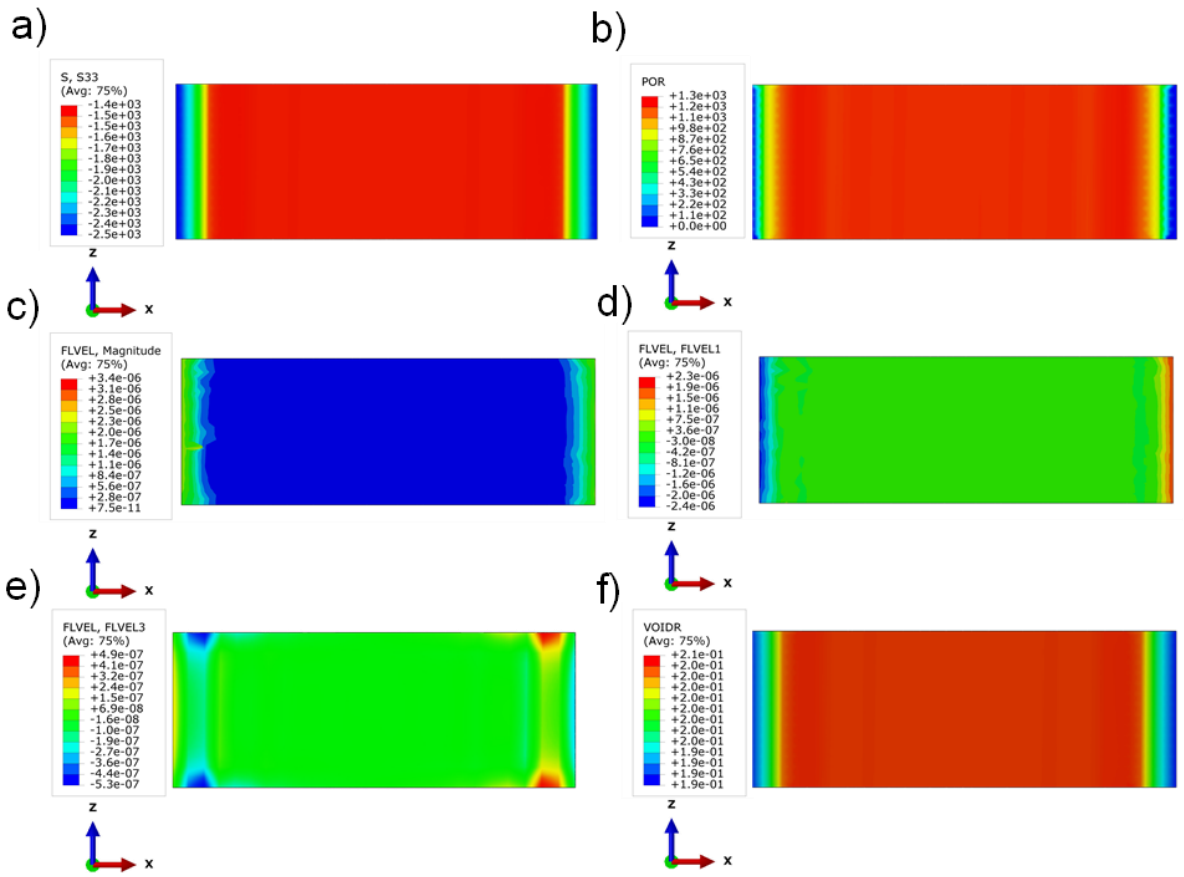

Figure 25. The predicted FE results using viscoelastic biphasic model for the brain specimen under unconfined compression test at 30% compressive strain. The simulation was performed at speed of 10 mm/sec and the results demonstrated the cross-sectional contour of: a) the solid stress in "Z-Z" direction, b) the hydrostatic pore pressure of fluid phase, c) the resultant velocity of liquid content, d) the fluid flow in "X-X" direction, e) the fluid flow in "Z-Z" direction, and f) the spatial variation of void ratio.

Moreover, this viscoelastic biphasic model was able to present the rate-dependency behavior for both phases. Figure 26 a-d provide a distinct demonstration of how the effective stress in the solid matrix, and pore pressure of the fluid phase vary for different loading velocities. The effective stress in solid phase ($\boldsymbol{\sigma}_e$), attained larger stresses at higher rates, indicating that the assigned hyper viscoelastic constitutive model to the solid network can successfully exhibit this viscoelastic feature for this phase. Also, the pore pressure of interstitial fluid raised with increase in the deformation speed, confirming the ability of this model to capture the rate-dependent behavior of fluid phase. Figure 26-d compares the evolution of the total stress ($\boldsymbol{\sigma}_T$), computed at the middle of sample, and the true stresses determined from tests at different rates of 10, 100, and 1000 mm/sec. The total stress is obtained by the summation of the stress tensors in fluid phase and solid matrix, and the global mechanical response showed a good agreement with test results at larger strains ($0.7 \leq \lambda \leq 0.8$).

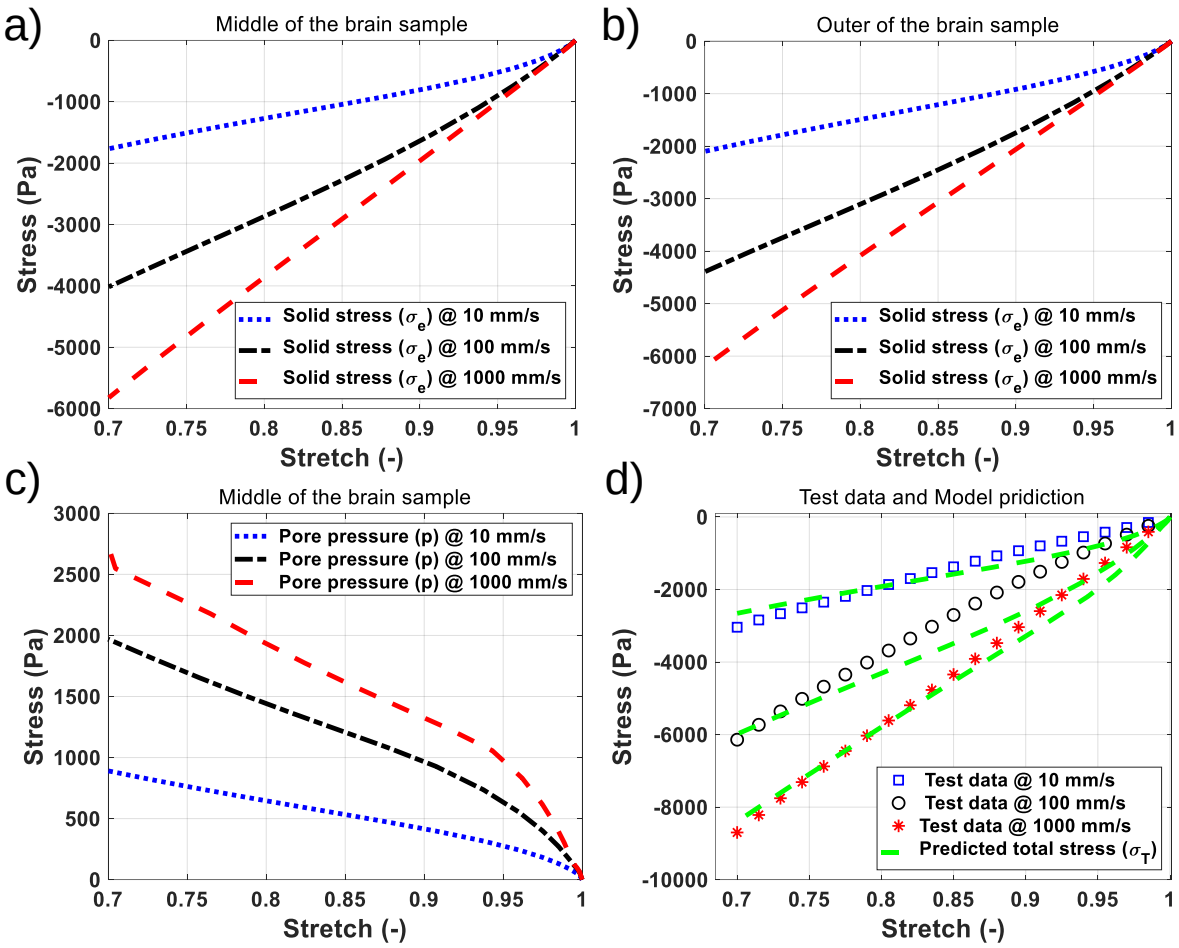

Figure 26. The rate-dependent decomposed contribution for the mechanical response of each phase; the evolution of stress in solid phase of the tissue among different loading velocities determined at: a) middle, and b) the outer surface of the brain, c) the rise of pore pressure based on the rate changes for a point at the middle of specimen, and d) the predicted total stresses in the middle of sample compared to the test data.

Figures 24 and 26-c implicitly imply that the higher values of pore pressure at the middle of the brain sample are due to the fact that the incompressible fluid contents are blocked inside the void spaces. Moreover, this phenomenon is distinctly represented in Figure 27. As it can be seen the predicted variation of void ratio was found to be insignificant (~0.01%) inside this porous media. These findings corresponded to the fully saturation assumption for this modeling. The void ratio at the outside of brain changes slightly under compressive deformation (~0.5%), which means insignificant fluid contents flowed out of the brain sample. These FE results are confirmed by our

experimental data since no dehydration and drainage was observed throughout the compression tests. Also, during the experiments the samples were kept hydrated, therefore it proves that the fully saturated condition in compression was an appropriate assumption for this study.

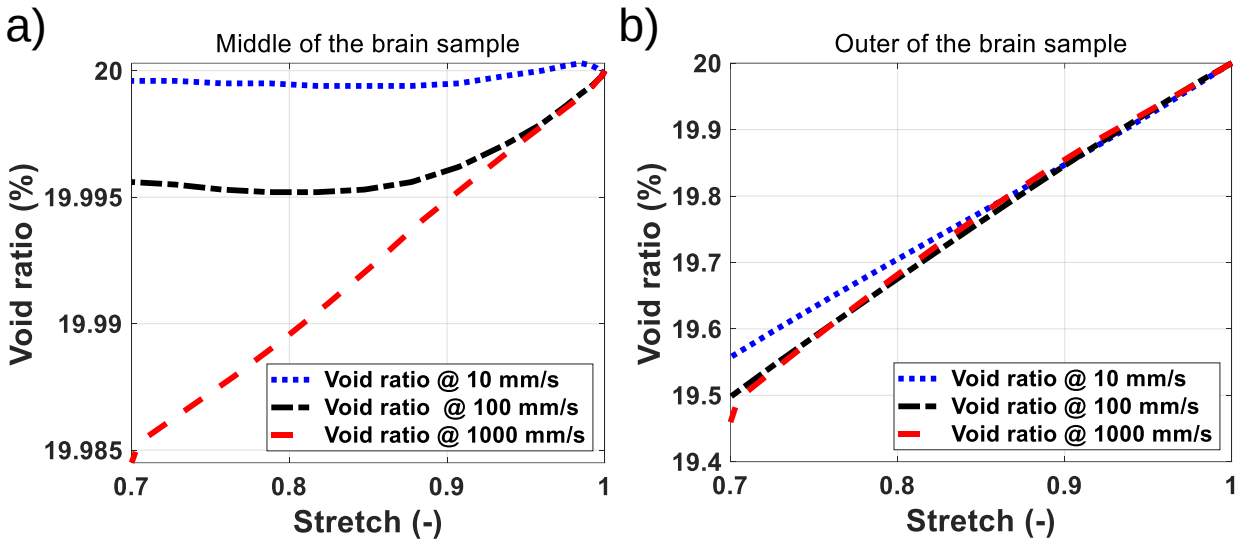

Figure 27. Variation of void ratio (%) vs. stretch ratio, calculated during three different compressive velocities at a) the middle and b) outer surface of brain specimen.

Figures 28 a~f and 29 a~k present the model prediction and the 3D representation of FE simulations of fluid flow for the brain sample under compressive deformation at rates of 10, 100, and 1000 mm/sec. As depicted in these figures, the liquid contents transfer nearly symmetrically in “X-X” and “Y-Y” directions, perpendicular to the direction of applied force. Also, in all directions the effective flow velocity in the middle is found to be significantly lower than effective velocity of a point placed at the outer surface of brain sample. These findings are in agreement with void ratio variations, showing the sample mainly possesses a constant fluid volume fraction in the middle, and very limited water contents leave the outer surfaces of the specimen. Overall, the liquid velocity in “Z-Z” direction was insignificant (≈0), and the transversal flows varied significantly for different compression velocities. These changes are better illustrated in Figure 30, in which the magnitudes of fluid velocities were increased with the rise in the deformation rates.

Figures 28 and 29, as well as Figure 30, provided a valuable perception for the spatial fluid diffusion through the brain tissue during compression and its rate-dependent behavior.

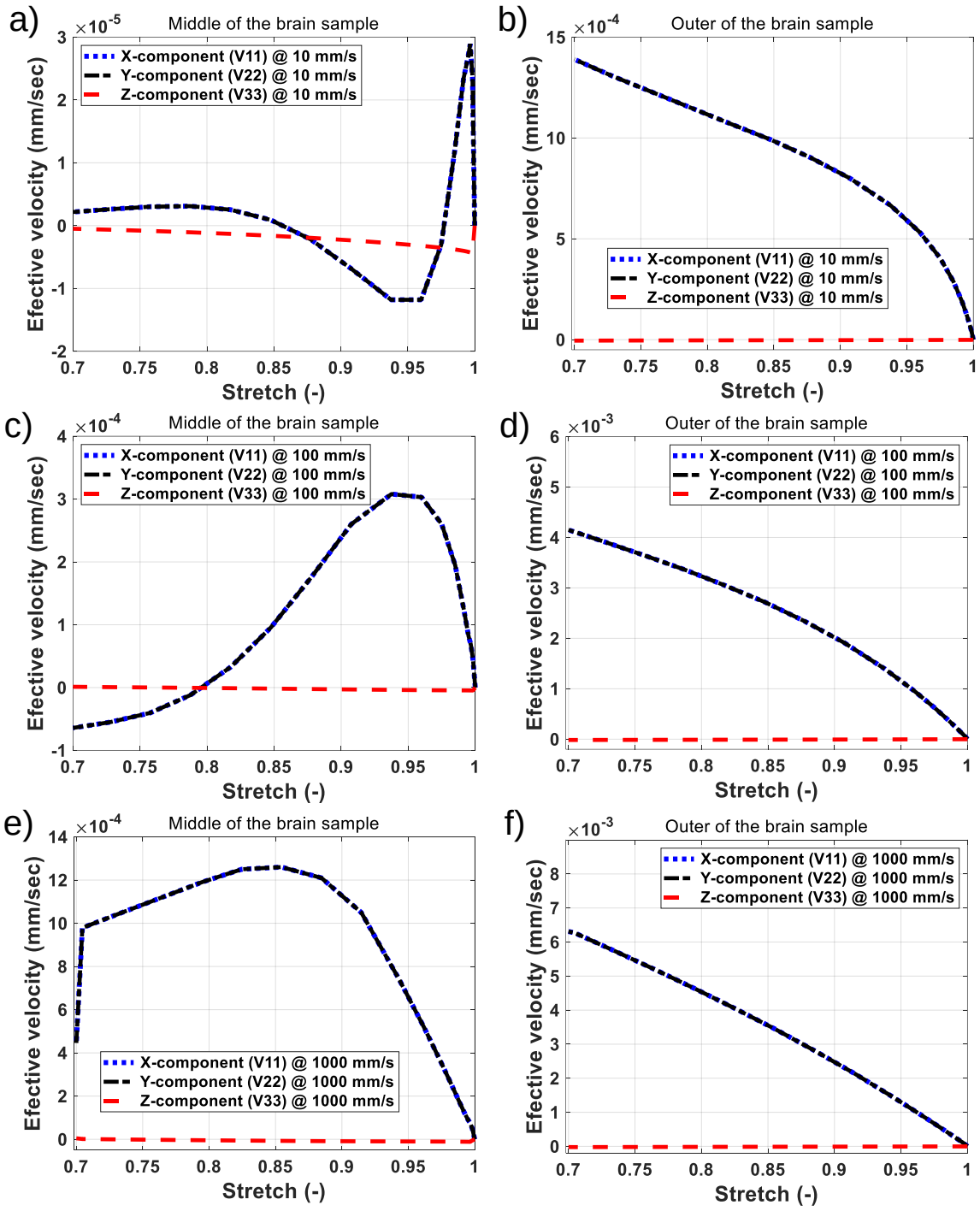

Figure 28. Variations of fluid velocity components versus stretch, in the middle and outer corner of brain specimen under compression velocities of: a, b) 10 mm/sec, c, d) 100 mm/sec, and d, e) 1000 mm/sec.

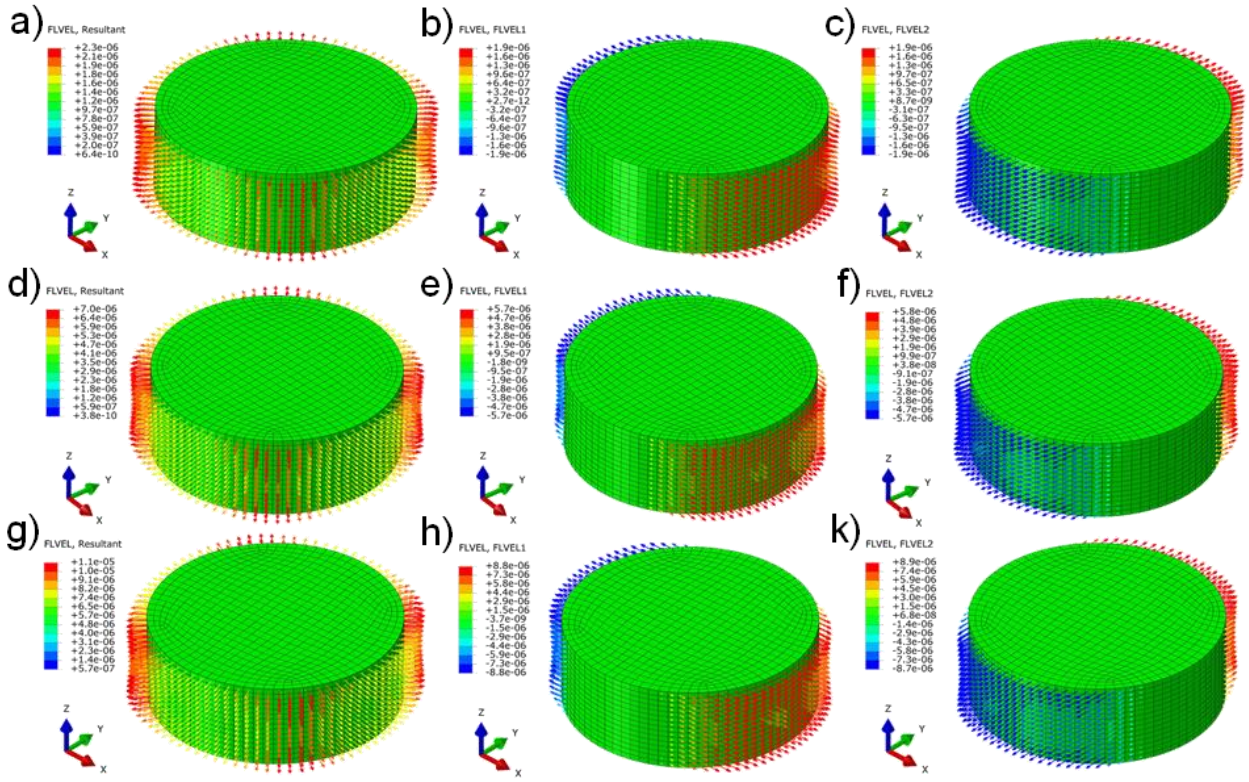

Figure 29. Demonstration of fluid velocities for brain sample, deformed under 30% compressive strain; present the overall magnitude and velocity distribution at "X-X" and "Y-Y" directions and at deformation rates of (a-c) 10 mm/sec, (d-f) 100 mm/sec, and (g-k) 1000 mm/sec. This biphasic model successfully shows that the fluid contents move faster under higher rates.

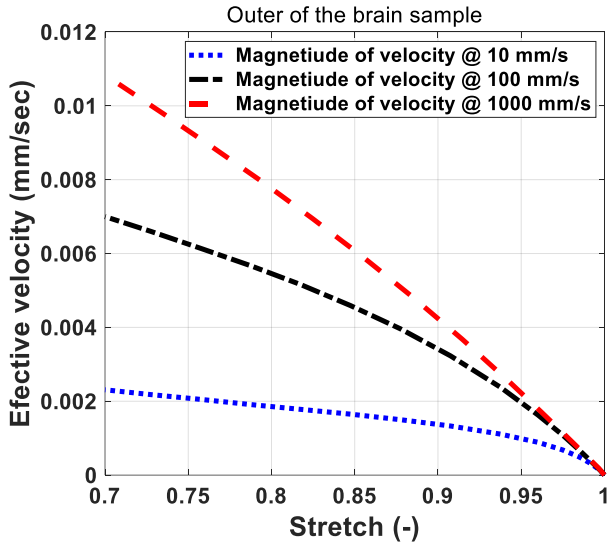

Figure 30. Changes of the resultant velocities for fluid phase vs. stretch, computed at three different loading rates.

5.4. Discussion

In order to accurately predict the mechanical behavior of brain tissue, one needs mathematical models reflecting its multiphasic nature and working under large deformations assumption and rate-dependent behavior. The single-phasic constitutive models fail to describe the interplay between tissue constituents, which is essential in numerical analysis of TBI, neurosurgery, and medical treatments. Also, the observations of volume changes on brain tissue [40, 125, 183], question the assumption of incompressibility in such monophasic material modeling neglects this tissue characteristic, and suggest that volume changes have to be considered through the biphasic theories beyond its typical viscoelastic nature. To date, a limited number of multiphasic models have been devoted to studies of this porous medium, motivating us to delve into examining the viscoelastic biphasic modeling of this substance. In this study, a set of unconfined compression tests were performed on the cylindrical brain specimens at deformation rates of 10, 100, and 1000 mm/sec. A poro-hyper viscoelastic model was introduced and calibrated with the experimental results. The computational results closely agreed with the experimentally measured forces (Figure 5), confirming that the proposed constitutive model is fully capable to characterize the rate-dependent behavior of brain tissue under compression deformation. The present work is an essential step concerning the development of a biphasic constitutive model able to predict the brain behavior during large deformation at arbitrary loading velocities.

The proposed biphasic model in current study, simply defined as the brain consisting of solid and fluid phases. This expression is more consistent with the microstructure and physical properties of brain cells and allows us to investigate the contribution of each phase separately. The general mechanical response of this porous tissue was decomposed into pore fluid pressure and the effective stress in the solid matrix. The rate-dependent nature of solid matrix was modeled by

a linear hyper viscoelastic constitutive relation. Also, the rate-dependent behavior for fluid phase was coupled with the velocity of solid network and governed by Darcy's law. The determined stresses in solid and fluid phases varied at different rates, and both constitute the variations in the mechanical responses of the tissue based on the loading speed. The majority of works in the literature of biomechanics of the brain, are devoted to modeling this soft porous tissue as a poro-elastic or poro-hyperelastic material [14, 164]. While those models are suitable to be used in such studies with small elastic deformation in a single strain rate, they failed to address the rate-dependent behavior of brain at large strains. As it was mentioned earlier, for studying the dynamic behavior of brain in transient analysis of TBI, it is crucial to develop a rate-dependent material model to capture the short-term response of the brain. However, the obtained constitutive parameters of the poro-hyper viscoelastic model presented in this study, were successfully evaluated for representing such particular behavior in the finite strain regime.

In addition, to examine the deformation of the solid phase, the biphasic model is able to determine the fluid diffusion throughout the solid network and the extracellular spaces as well. The interstitial fluid formed approximately 20% (varies between 15% and 30%) volume fraction of the brain's bulk structure [184]. Thus, understanding the pattern of fluid flow will result in an insightful study for each application, e.g. in predicting sub-structural failure caused by ECF flow from solid-fluid interaction [157, 185], or in estimating infused drug dispersion during convection enhanced drug delivery to brain tissue [28, 186]. Currently, with the limited experimental facilities, it's almost impossible to measure the fluid motion inside the pore spaces, so the validity of computed liquid contents distribution can be in general verified by the few physical evidences (e.g. drainage at outer surface). For instance, as depicted in Figures 25, the liquid phase velocity in the major portion of middle section of the specimen is not remarkable, confirming the earlier results.

This is due to the fact that under compressive deformation, the fluid contents are stuck in pores which consequently increases the hydrostatic pressure.

It should be emphasized that the fluid phase parameters are physical properties that need to be explicitly measured and cannot be obtained by fitting to the stress-stretch curves [187, 188]. For example, hydraulic conductivity is an independent property that describes the ease with which a fluid can move through pore spaces and should be measured directly by the permeability test [187]. In this study, we have employed the well-known value of this property from literature. Thus, the accuracy of the model is associated to such constant evaluated in previous studies. Kaczmarek et al. [176] proposed that the hydraulic conductivity of gray matter ($1.57\ 10^{-9}$) is considerably smaller than that of the white matter ($1.57\ 10^{-7}$). For this study, an average value of hydraulic conductivity ($1.57\ 10^{-8}$) is considered, since the brain samples were consisted of a mixed gray and white matter. Also, there are various values have been reported for this conductivity, with alternations of up to three orders of magnitude. Smillie et al. [189], Cheng and Bilston [60], and Franceschini et al. [40] have reported the value of 1.37×10^{-7}, 8.11×10^{-8}, and 2.42×10^{-10} for the hydraulic conductivity of brain tissue, respectively. Employing each of these values in the biphasic material model, results in different estimation for the behavior of fluid phase. Figure 31 demonstrates the variation in two fluid characteristics, i.e. the fluid velocity and pressure, evaluated based on different permeability constants from the literature. As clearly depicted in this figure, the higher value of permeability indicates the easier liquid passage through the cellular network, led to greater flow velocity and less hydrostatic pressure for this phase. On contrary, lower value of conductivity develops higher hydrostatic pressure and minor liquid diffusion velocity within the tissue.

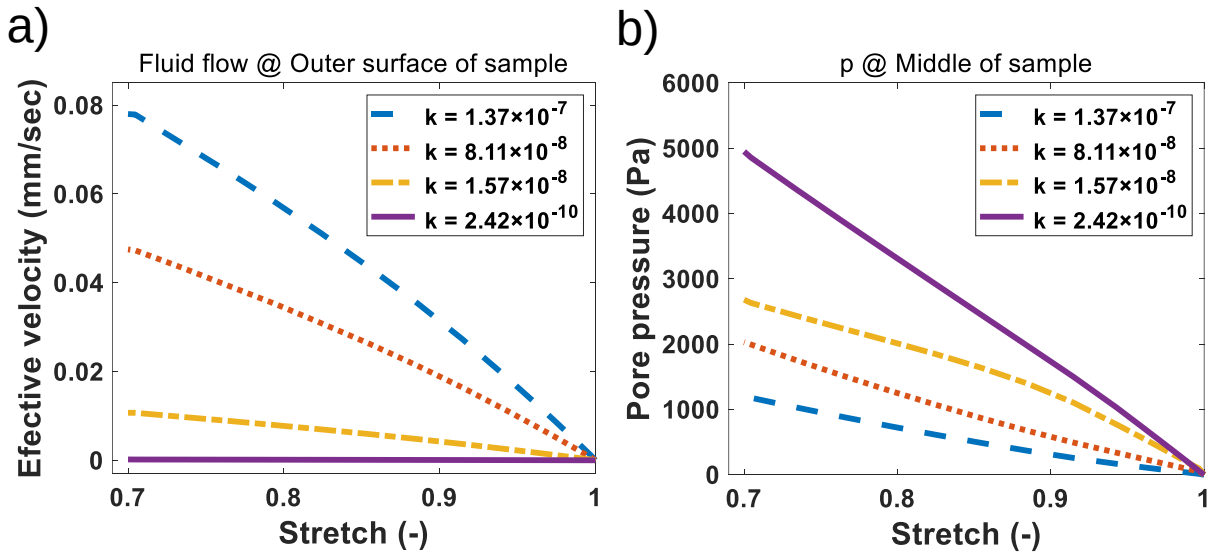

Figure 31. The alterations in a) fluid flow, and b) the pore pressure, determined based on various reported hydraulic conductivity (*k*) for a brain specimen compressed at speed of 1000 mm/sec.

The main observation from experimental data is that the brain tissue is a rate-dependent material which shows larger stress at higher strain-rates. This behavior has been reported in the literature and was known due to the effect of viscosity of existed fluid in the tissue [14]. It is a known behavior of incompressible fluid, that under confined condition resists to external compressive forces and produces more pressure at chock loads or for compression with high speeds. Correspondingly, for the fluid contents trapped in extracellular or in pore spaces of this porous tissue, their pressure is increased and show more stiffness under higher speed of compression. Haslach et al. [185] proposed that the perceived hardening of the stress–stretch curve of brain in unconfined compression test, is because the extracellular passageway volumes were restricted by compression deformation. The solid phase thus resists the fluid flow and led to increase in hydrostatic pressure. Moreover, in the high-speed deformation the liquid contents have very limited time to get distributed in the solid networks, and practically they cannot move and become blocked in their position. This phenomenon leads to less permeability value and is reflected into higher stiffness which consequence in more pressure measured out of tissue in the

experiments with higher speeds. This suggested reason of showing rate-dependent behavior for brain tissue is supported by the analytical result of biphasic model which clearly indicated that smaller value of hydraulic conductivity lead to higher pore pressure.

Similar to other engineering parameters, the developed strain-rates in the brain specimens can be calculated by FE analysis. The results of FE simulation show the brain has a uniform distribution of strain-rates. As it demonstrated in Figure 32 and under 30% of strain, and with the compression velocity of 10, 100, and 1000 mm/sec the vertical strain-rate (ER22) were found to be respectively -0.94, -9.4, and -94 s^{-1}. These values were negative, since they are related to compressive deformations and strains. The transversal strain-rate components in "X-X' and "Z-Z" directions (ER11 and ER33) were identical and with value of 46 s^{-1} at the speed of 1000 mm/sec. Although for a constant velocity it was expected to obtain the constant strain-rate, the calculated strain-rate showed some variation at different strain. These variation for both lateral and vertical strain-rates (ER11 and ER22) are demonstrated versus the compressive strains and depicted in Figure 32 c, d.

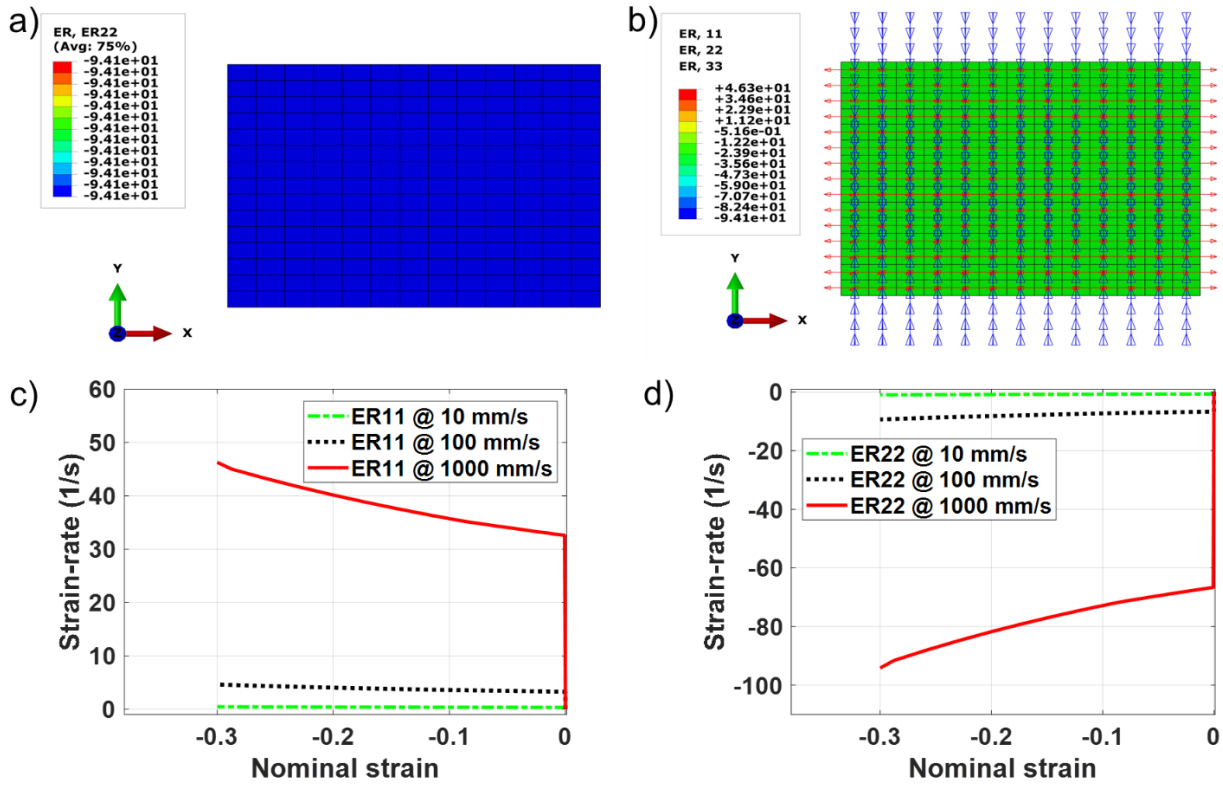

Figure 32. The demonstration of determined strain-rate: a) the strain-rate contour in the direction of "Y-Y" plotted for 30% of strain, b) symbol plot of strain-rate components at 3 directions plotted for 30% of strain, c) the variation of strain-rate in transversal direction vs. strain, d) the variation of strain-rate in vertical direction vs. strain.

As the limitations of present study, it should be mentioned that the tissue was characterized for only uniaxial compression deformation across a range of intermediate to high rates. If the constitutive constants are evaluated for one particular deformation mode such as compression, it may not exhibit the correct behavior for other deformation modes such as tension, shear or other combined loadings. Estimating the material parameters from a mixed white and gray matter for the brain tissue, was the other limitation of this work. The results, therefore, are only valid for such a composite and can be useful in an approximate modeling of the brain [51, 59]. The solid phase was assumed to have an isotropic structure, so the average mechanical properties of the tissue were employed in obtaining the material parameters; however, this procedure is accepted in determining such parameters which are functional to predict an approximate behavior of the brain. Moreover,

in some studies it was postulated that the anatomical location [145, 146] and the direction [43, 117] of extracted brain samples had insignificant effect on the tissue response.

5.5. Conclusion

This chapter introduced the key features of experimental, theoretical, and computational procedure for characterizing the rate-dependent behavior of brain tissue by the proposed viscoelastic biphasic constitutive model. In experimental components, in-vitro unconfined compression tests up to 30% nominal strain over three orders of deformation rate magnitude (10 to 1000 mm/sec) was performed on bovine brain tissue. The significant effects for rate-dependency behavior of this soft biological tissue were observed. It was shown that the changes in deformation rate, results in variation of the mechanical features i.e. the nominal stress and apparent elastic moduli. Based on the microstructure of brain, and starting from the theory of porous media, a theoretical-computational framework for the biphasic modeling of this soft biological tissue was presented. In addition to representing the rate-dependent mechanical response and deformation of the solid phase, this biphasic model demonstrates the flow and diffusion of the liquid through the tissue networks. The model can also express exclusive contribution of each phase concerning the general behavior of the tissue. The very good agreements between the experimental, and computational results has indicated that the proposed model is fully able to characterize and be employed in FE simulation of the brain tissue. This current study could therefore lay a groundwork for further studies of brain injury caused by such combined fluid diffusion and cellular distortion.

CHAPTER 6. DETERMINATION OF BIPHASIC VISCOELASTIC PARAMETERS FOR HUMAN BRAIN TISSUE[4]

6.1. Introduction

Recently, the mechanical behavior of human brain has been studied through a wide variety of shear, shear relaxation, compression, compression relaxation, and tension tests for four different regions of the brain, the cortex, basal ganglia, corona radiata, and corpus callosum [43, 190]. Budday et al. [43] have calibrated five incompressible single-phase hyperelastic models with their experimental data and have reported their material parameters in Table 7 of their paper. In addition, Budday et al. [190] have examined the brain viscoelastic behavior and provided the constitutive constants required to represent the tissue time-dependent response. The combination of hyper-elastic springs and viscoelastic dashpots were employed to model the time-dependent properties of tissue under arbitrary loading conditions [190, 191]. The reported viscoelastic material constants of those publications are not supported by commercial FE packages yet; therefore, further efforts are required in order to find suitable properties for computational simulations of the brain. Also, it seems in their model calibration, they derived the stress-stretch equations based on an assumption of uniaxial stress and applied such equations to the non-uniaxial test results. In this study we will demonstrate that those reported material parameters could not appropriately represent the tissue response in FE simulations.

The main aim behind presenting this chapter is to show a new poro-hyper viscoelastic model based on macroscopic continuum to motivate a deeper study for biomechanical analysis of this multiphase tissue. In constitutive modeling of this biphasic approach, the interstitial fluid is

[4]Hosseini-Farid, Mohammad, Ziejewski, Mariusz, and Karami, Ghodrat. Mohammad Hosseini-Farid had primary responsibility for this chapter, and the rest of co-authors help him to proof-read this chapter for being submitted as a journal paper titled as "Determination of biphasic viscoelastic parameters for human brain tissue".

assumed to be incompressible, while the solid phase is considered as a compressible material. For this work, the comprehensive test data published by Budday et al. [43, 190], have been trusted and employed as the experimental data to determine the biphasic material parameters for different regions of the human brain. They reported a single-phase model for the brain, so the biphasic model would improve upon their fitting. In the model calibration, the mechanical responses of brain under compression, tension and shear loadings are employed. To involve a full observation of long-term time dependency and viscoelastic behavior of the brain, the whole history for compression-relaxation test data is also considered. To obtain the constitutive parameters instead of the regular curve fitting, a FE model of the brain samples is developed simulating the physics of experiments in an iterative process. The results and the discussions are provided and subsequently conclusions are drawn.

6.2. Material and method

6.2.1. Experimental data

Recently, in the biomechanics literature of brain, Budday et al. [43, 190, 191] have performed a wide-ranging set of experiments on human brain tissue. They have conducted compression, compression relaxation, shear, shear relaxation, and tension for four different regions of the human parenchyma. For their experiments 5×5×5 mm tissue samples were extracted from the cortex, basal ganglia, corona radiata, and corpus callosum. The uniaxial and shear experiments have been performed with different testing protocols and in different directions with respect to the axonal fibers preferred orientation. In the uniaxial experiments, they conducted the compression and tension test up to 0.9 and 1.1 of stretch, respectively. For uniaxial tension and compression test, the samples were loaded at a quasi-static loading condition with the speed of v=2 mm/min. For simple shear test, the maximum displacement of 20% of specimen height is applied in both x-

and y-directions. Before they conducted the test, they carefully humidified the specimen with phosphate-buffered saline solution, and maintained the samples fully hydrated throughout the whole test procedure. Next, they conducted unconfined compression-relaxation test of 300 sec holding at constant compression level. Since no statistically significant anisotropic behavior of the tissue was observed, they presented regional dependent stress-stretch curves averaging all the tested directions in each region. Figure 33-a~d demonstrate the average experimental data of uniaxial tension, compression, relaxation and shear in four regions of the human brain (Basal Ganglia, Cortex, Corpus Callosum, Corona Radiata). This data, adapted from Figures 11 and 4 respectively of the publication [43] and [190], represents the mechanical behavior of tissue under instantaneous and the long-term conditions.

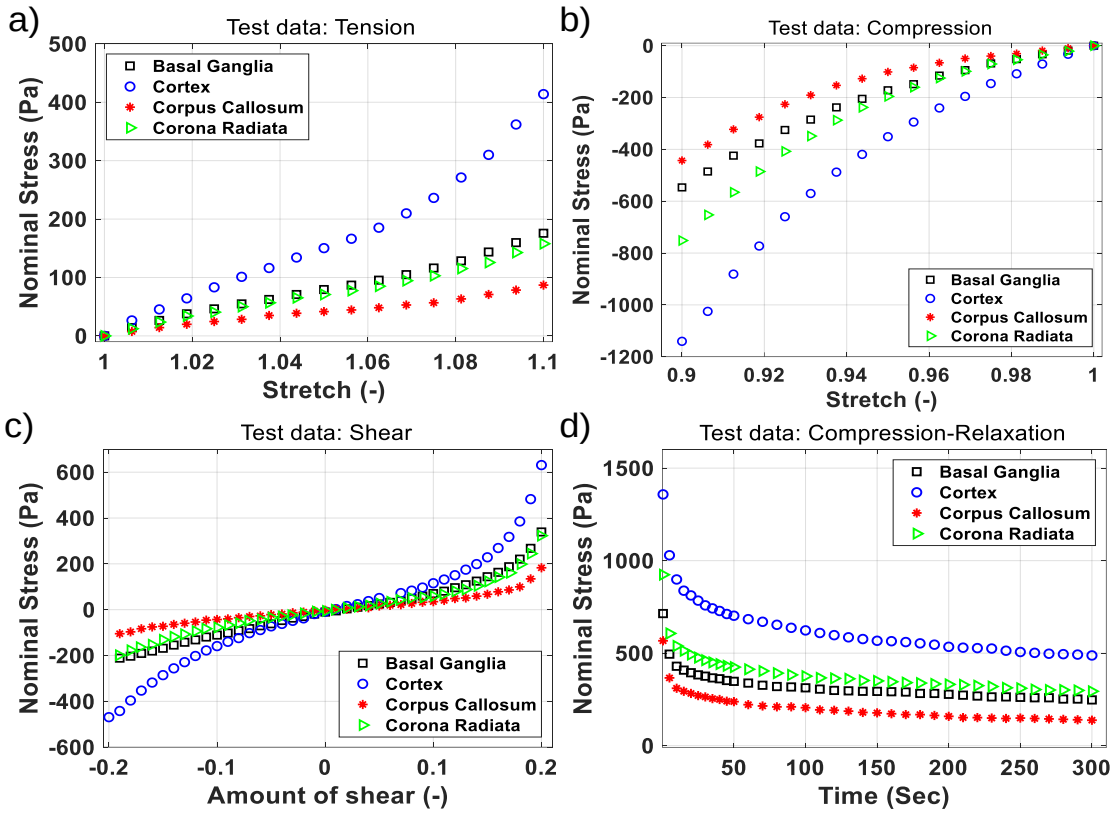

Figure 33. Averaged experimental data presenting the mechanical responses in four regions of human brain (Basal Ganglia, Cortex, Corpus Callosum, Corona Radiata) under 4 various loading modes: a) tension test, b) compression, c) simple shear, and d) compression relaxation tests, adapted from *[43, 190]*.

6.2.2. Material stability

Generally, the strain energy function is dependent on the deformation through the right Cauchy-Green deformation tensor ***C***, and a hyperelastic model should satisfy the Drucker stability criterion and thermodynamic restrictions [182, 192]. The Drucker stability condition for a compressible material requires that the stored energy be greater than zero. Hence, the small change in the stress, $d\boldsymbol{\sigma}$, accompanied by an infinitesimal change in the logarithmic strain, $d\boldsymbol{\varepsilon}$, should satisfy the inequality $d\boldsymbol{\sigma} : d\boldsymbol{\varepsilon} > 0$. Using material stiffness tensor, **C**, the relation between changes in the changes in the strain and stress, will be represented in the form of the matrix

$$\begin{Bmatrix} d\sigma_1 \\ d\sigma_2 \\ d\sigma_3 \end{Bmatrix} = \begin{bmatrix} C_{11} & C_{12} & C_{13} \\ C_{21} & C_{22} & C_{23} \\ C_{31} & C_{32} & C_{33} \end{bmatrix} \begin{Bmatrix} d\varepsilon_1 \\ d\varepsilon_2 \\ d\varepsilon_3 \end{Bmatrix} \tag{39}$$

The inequality then becomes $d\boldsymbol{\varepsilon} : \mathbf{C} : d\boldsymbol{\varepsilon} > 0$. That means the tangential material stiffness (**C**) must be positive definite. This restriction is called material stability and should be considered during the calibration of material constants to the experimental data. Ideally, no instability should occur. However, in some models and for some set of constitutive parameters, the instabilities might be observed at certain strain levels and that is likely to occur in the analysis as well [193]. Generally, the hyperelastic models with given positive material parameters demonstrate a fully stable behavior. On the other hand, those material models with one or more negative parameters will not attain the positive strain energy value at all range of tension and compression strains. For instance, it is possible that the constitutive model represents a negative stress value at a specific level of tensile strain. Therefore, it is strongly recommended that the strain levels of the material stability be carefully examined and reported for further application.

6.3. Results

6.3.1. Determination of the material parameters

Same biphasic model and calibration procedure explained in Chapter 5, was employed for the reported test data of human brain tissue. In this research, to obtain one set of material valid for different loading modes, a combined data of all testing modes (tension, compression, and shear) as well as whole history of relaxation experiments are utilized in material calibration. The computational process of compression-relaxation testing for four different regions of human brain was carried out by two transient analysis steps. In the first step, the instantaneous response was modeled; the samples were compressed to 10% of its engineering strain (or λ=0.9) with deformation speed of 2 mm/min. Then in the second step, to simulate relaxation behavior, the deformation was kept fixed at 10% strain within 300 seconds, so the model can get relaxed with its loading history. As it depicted in Figure 34 a,b and Figure 35 a~d, very good agreement ($R^2 \geq$ 0.93, where R^2 is the coefficient of determination) between calculated and experimental results was achieved for brain samples under different loading modes and during relaxation histories. In order to obtain the measured force shown in these figures, the Lagrangian stresses presented at original publication were multiplied by the initial top area of brain sample. Table 1 provide the summery of calculated poro-hyper-viscoelastic material parameters for brain samples. The Drucker stability condition as a post-processing step was checked for the obtained constitutive parameters, and the range of strains that satisfy the material stability are provided at Table 11. Practical stabilities were observed for this model at any range of tension and most of compression strains.

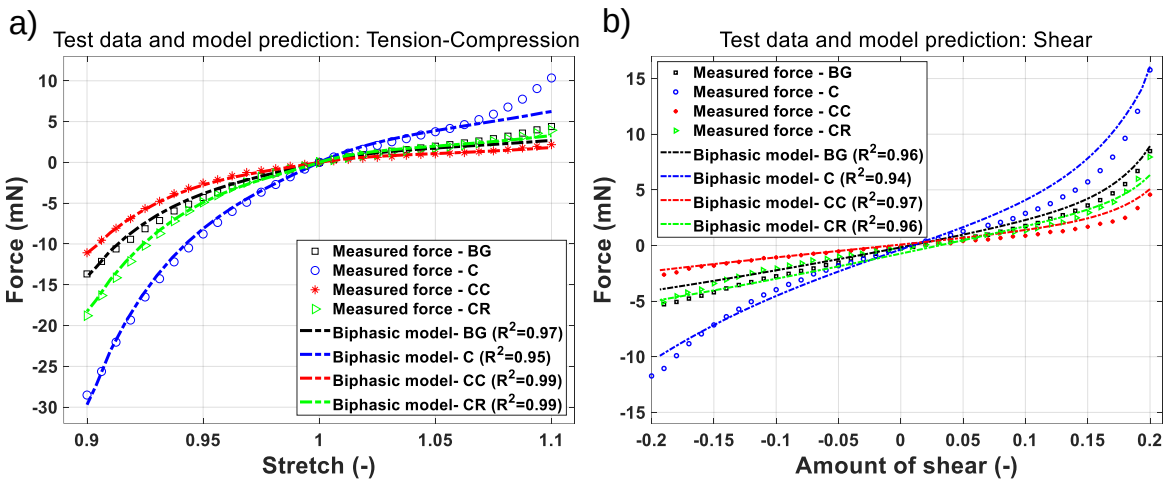

Figure 34. Experimentally measured force [43] and the predicted force based on FE simulations under a) tension, compression, and b) shear loading modes using material parameters of poro-hyper-viscoelastic model as shown in Table 11 in four regions of human brain: Basal Ganglia (BG), Cortex (C), Corpus Callosum (CC), and Corona Radiata (CR).

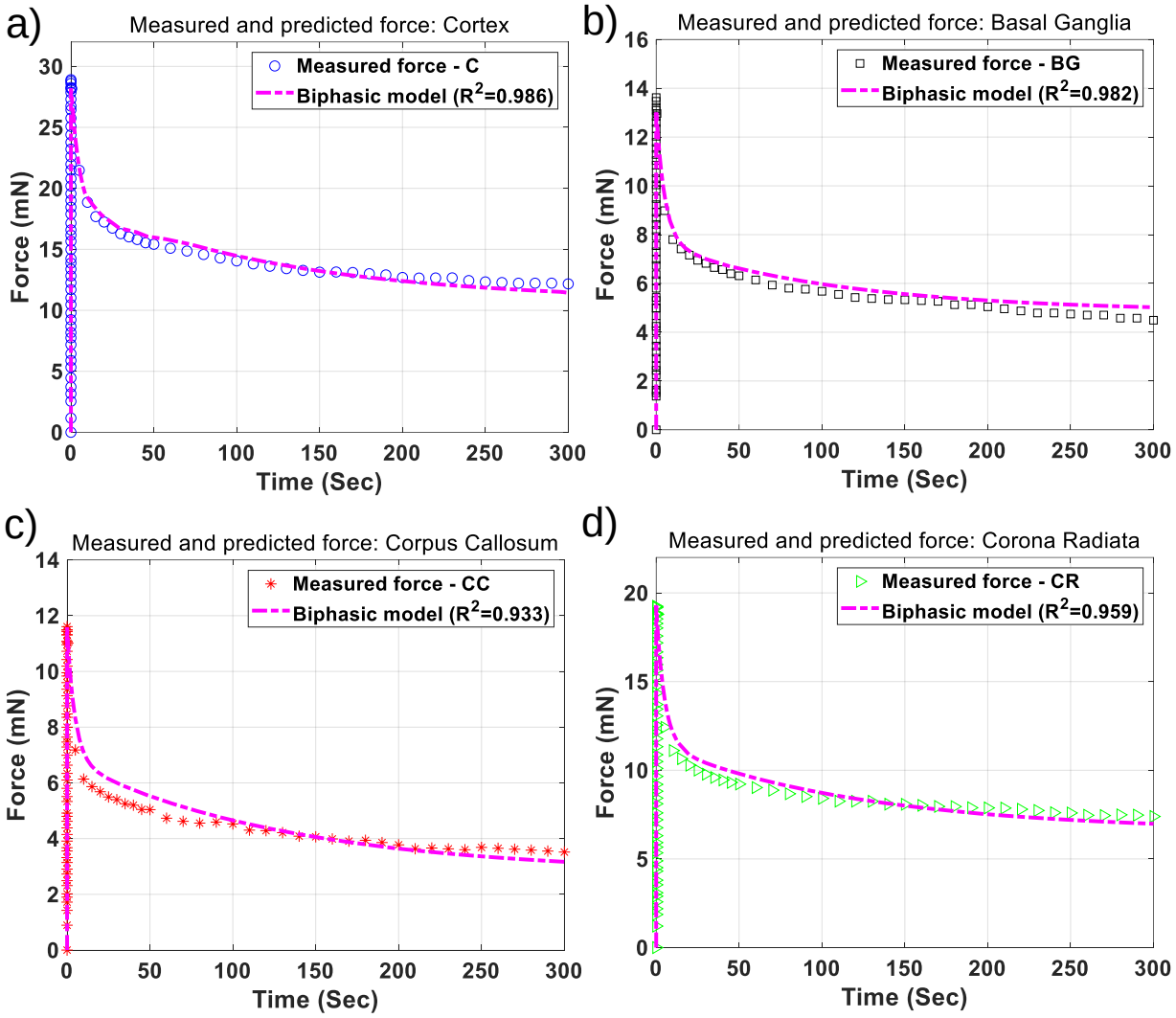

Figure 35. Experimentally measured force of compression relaxation adapted from [191] and the predicted force based on FE simulations using material parameters of poro-hyper-viscoelastic model as shown in Table 1 in four regions of human brain: a) cortex, b) basal ganglia, c) corpus callosum, and d) corona radiata.

Table 11. Summary of determined material parameters for poro-hyper-viscoelastic model, calibrated for whole loading history of compression relaxation experiments using the iterative simulation procedure at four regions of human brain.

Matter	Solid phase								Fluid phase		
	Deviatoric Parameter		Volumetric Parameter	Stability limits at nominal strain	Time Dependent Parameter				k (m/s)	γ (kN/m^3)	e_0
	μ_1 (Pa)	α_1	D_1 (Pa^{-1})		g_1	τ_1 (s^{-1})	g_2	τ_2 (s^{-1})			
Cortex	260	-18.7	$1.6\ 10^{-4}$	$-0.75 < \varepsilon < 1$	0.6	5.8	0.21	115	$1.57\ 10^{-9}$	9.741	0.2
Basal Ganglia	101	-19	$3.99\ 10^{-4}$	$-0.81 < \varepsilon < 1$	0.71	4.6	0.15	108	$1.57\ 10^{-9}$	9.741	0.2
Corona Radiata	114	-24.3	$3.5\ 10^{-4}$	$-0.7 < \varepsilon < 1$	0.74	3.5	0.14	112	$1.57\ 10^{-7}$	9.741	0.2
Corpus Callosum	36	-25.3	$1.12\ 10^{-3}$	$-0.67 < \varepsilon < 1$	0.73	3.5	0.2	118	$1.57\ 10^{-7}$	9.741	0.2

6.3.2. Computational results

The discretized geometry of specimen and applied boundary conditions are shown in Figure 36-a. As is illustrated in Figure 36-b and c, the maximum pore pressure under compression occurred at the top and bottom specimen surfaces, while for the equivalent (von Mises) stress, the maximum, was at the corners of the specimen. The detailed FE results for solid and fluid phase responses under compression, tension, and shear are demonstrated at Figures 36, 37, and 38. In other words, close to contacted surfaces at top and bottom of sample, the interstitial fluid is trapped, and its pressure is increased along with solid matrix deformation. However, because of interaction with zero pressure at the outer surface, the fluid phase poses zero or few pore pressures at free edges.

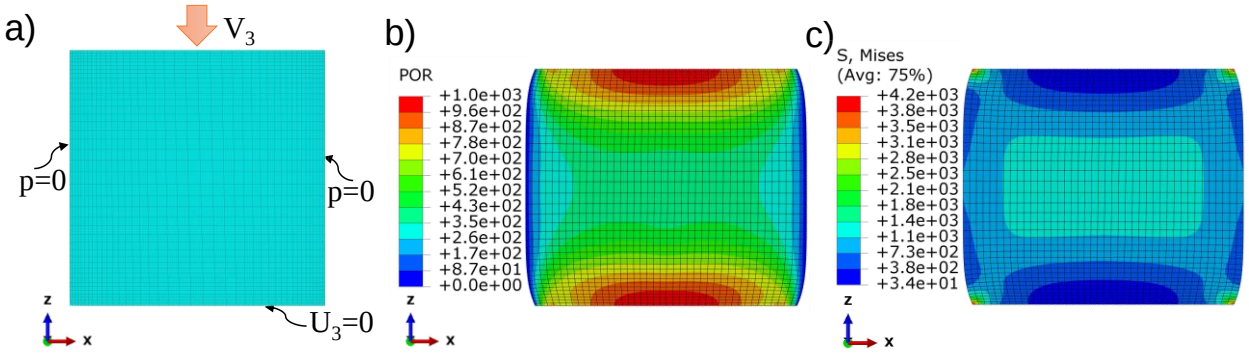

Figure 36. a) The discretized FE Model of brain sample with necessary boundary conditions utilized in computational studies, and plotted contours of: b) pore pressure and c) von Mises stress in solid phase at 10% nominal compressive strain for Cortex sample.

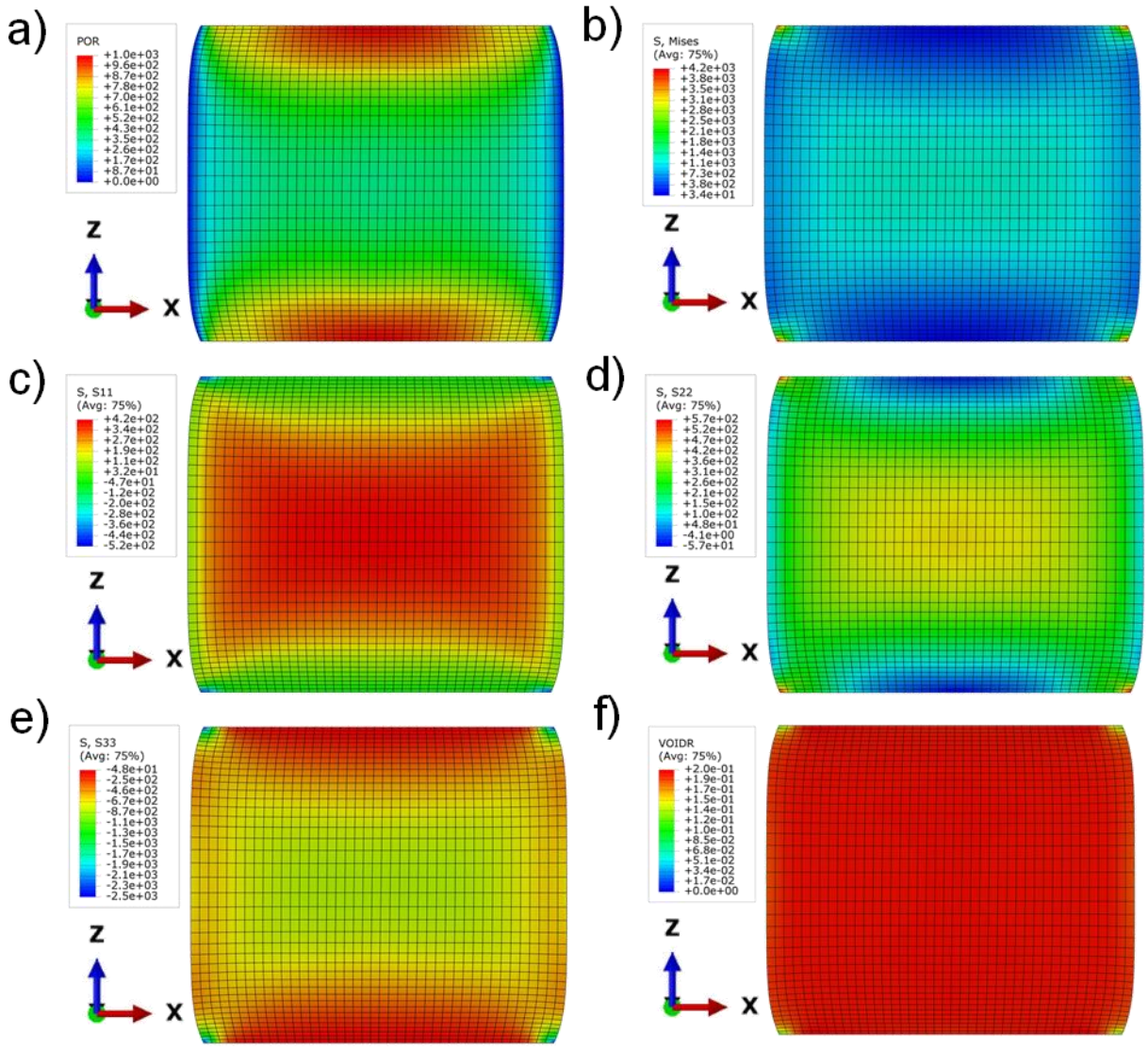

Figure 37. The computational results for biphasic modeling of the brain specimen (Cortex) under 10% nominal compressive strain, provide the distributions of: a) pore pressure of fluid phase; and stresses in solid phase such as b) equivalent (von Mises), and the stress components in: c) “X-X” direction, d) “Y-Y” direction, e) “Z-Z” direction, and f) also the void ratio variation in solid matrix.

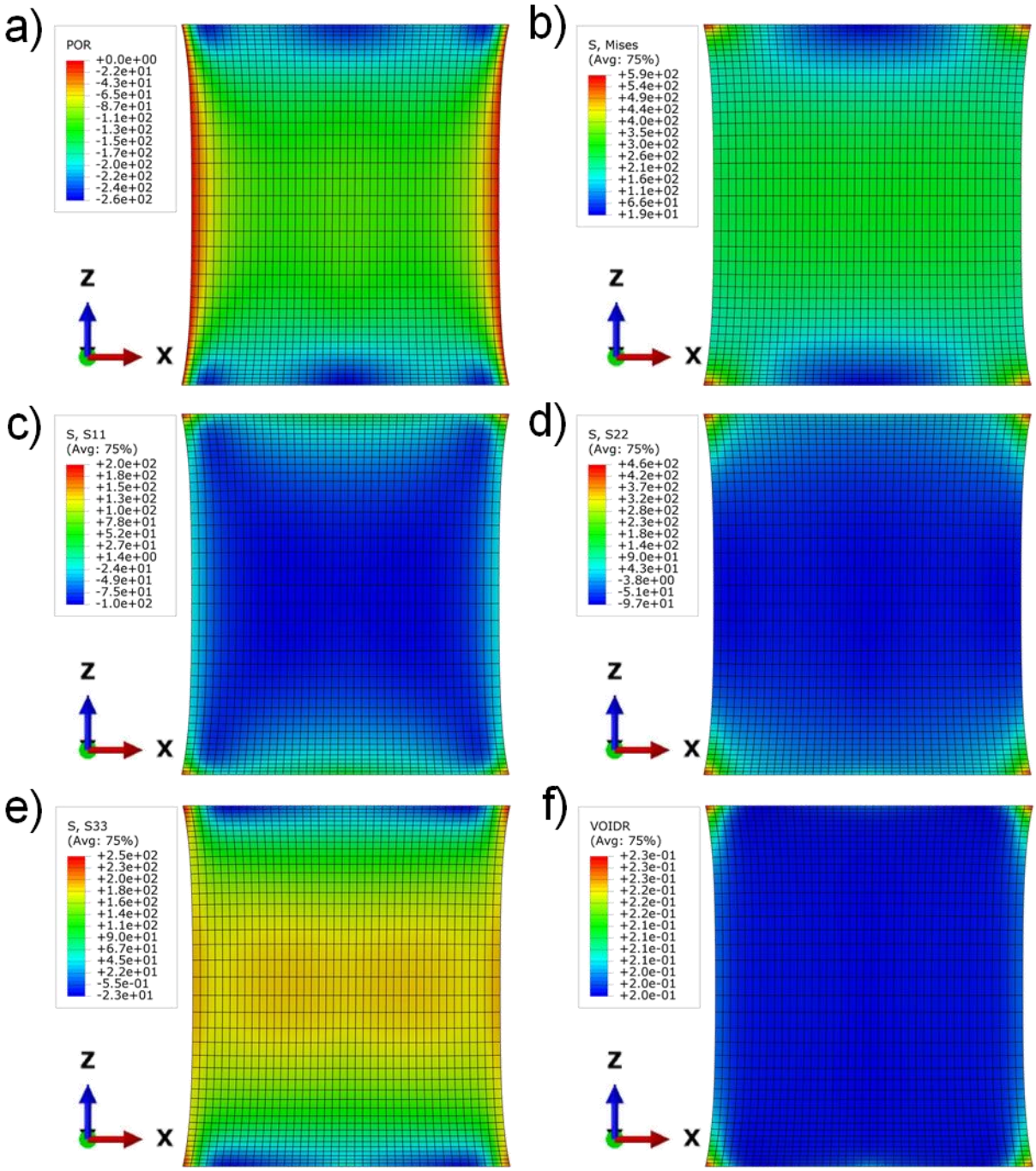

Figure 38. The computational results for biphasic modeling of the brain specimen (Cortex) under 10% nominal tensile strain, provide the distributions of: a) pore pressure of fluid phase; and stresses in solid phase such as b) equivalent (von Mises), and the stress components in: c) “X-X” direction, d) “Y-Y” direction, e) “Z-Z” direction, and f) also the void ratio variation in solid matrix.

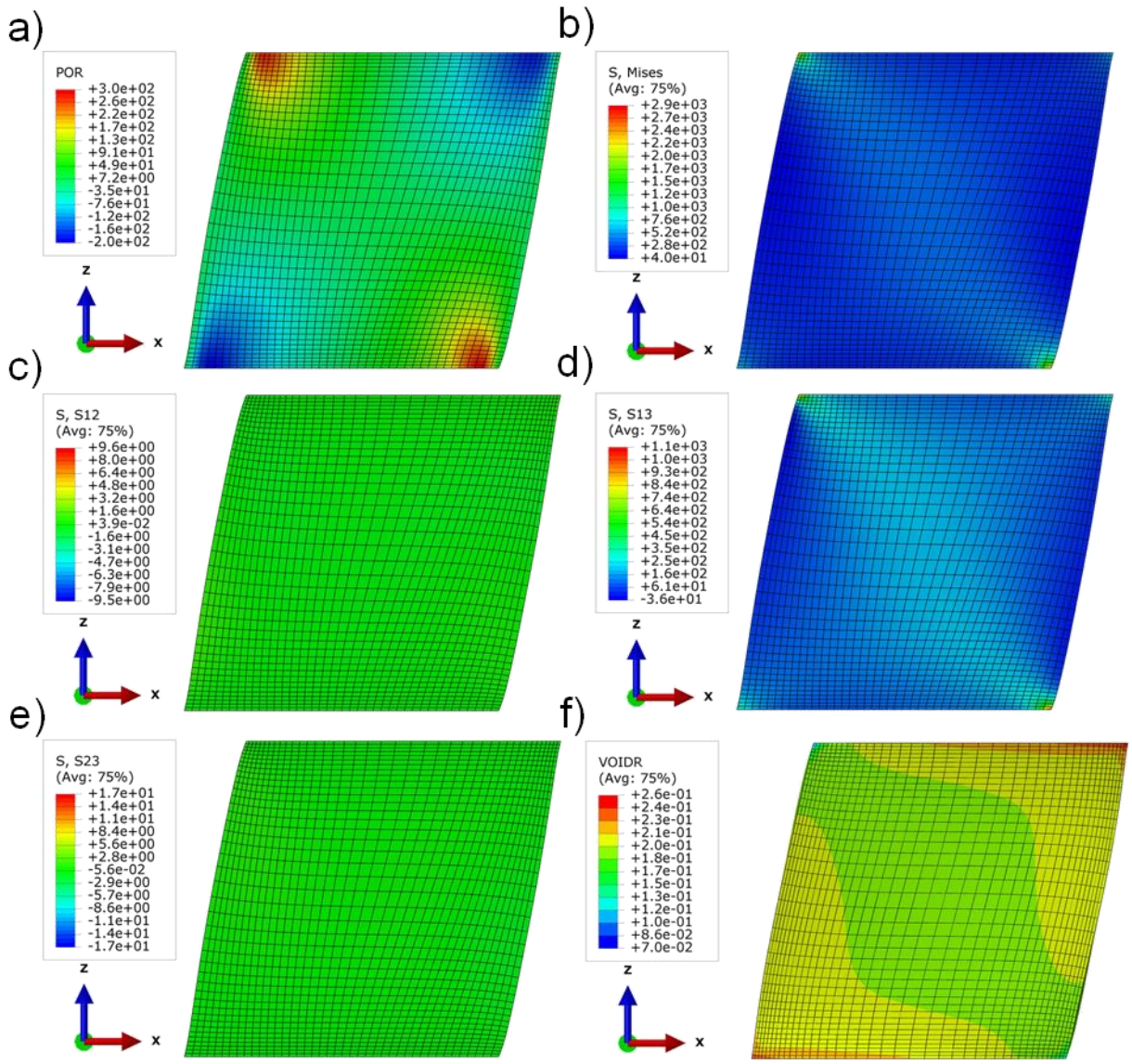

Figure 39. The computational results for biphasic modeling of the brain specimen (Cortex) under 0.2 shear strain, provide the distributions of: a) pore pressure of fluid phase; and stresses in solid phase such as b) equivalent (von Mises), and the stress components in: c) “X-Y” direction, d) “X-Z” direction, e) “Y-Z” direction, and f) also the void ratio variation in solid matrix.

The contribution of fluid phase pressures and stresses in the solid matrix as a result of the compressive and tensile loads at two points (in the middle and outer surface of sample), are depicted in Figure 40 a, b. This figure shows how under the applied load, the solid and fluid responses contributed into the global reaction of this soft porous tissue (see Figures 41, 42, and 43 for whole stress components in solid matrix under compression, tension, and shear). It clearly

indicates for the fluid phase at the middle of brain sample, how the positive and negative pore pressures are respectively developed due to compressive and tensile deformation. Also, Figures 35 and 39 implicitly denote the higher values of pore pressure at the middle of the brain sample are because the incompressible fluid contents were blocked inside the void spaces. However, this phenomenon, noticeably represented in Figure 44, where under compression and tension the predicted void ratio was found to be constant (≈ 20%), inside of this porous media. These findings correspond to the fully saturation assumption for this modeling. The void ratio at the outside of brain changes slightly under tensile (0.28%) and compressive (1.4%) deformation, which means insignificant fluid contents flow out of the brain sample. These FE results can be confirmed by the experimental data since no dehydration and drainage was observed while sample were tested [43]. Also, during the original experiments the samples were kept hydrated, therefore it proves that the fully saturated condition in compression and tension was an appropriate assumption for this study.

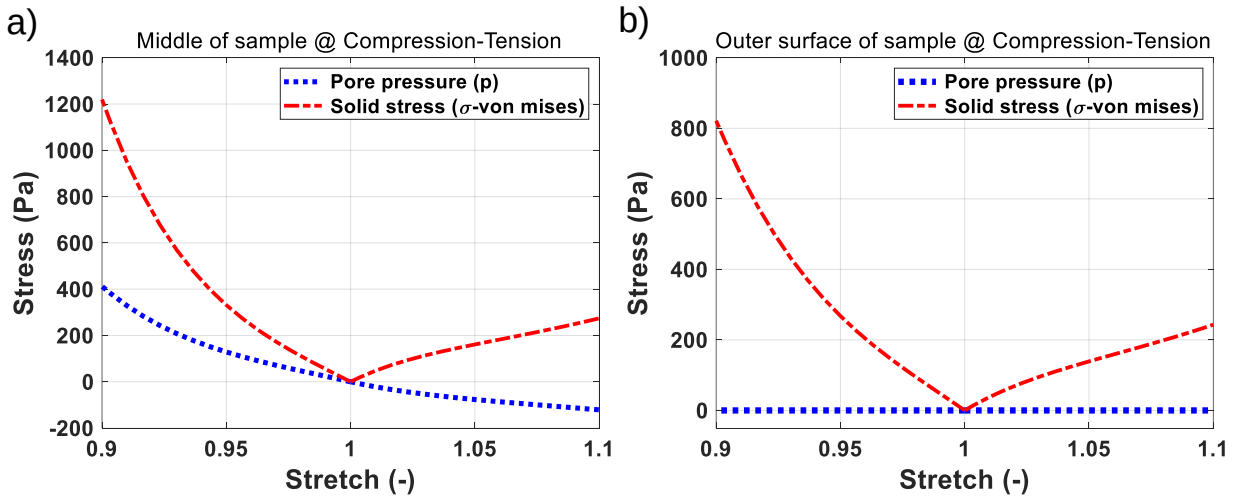

Figure 40. Contribution of pore pressure, p, and solid stress, $\sigma_{\text{von Mises}}$, versus stretch, predicted for: a) middle, and b) outer surace of brain (Cortex) sample under compressive and tensile deformation.

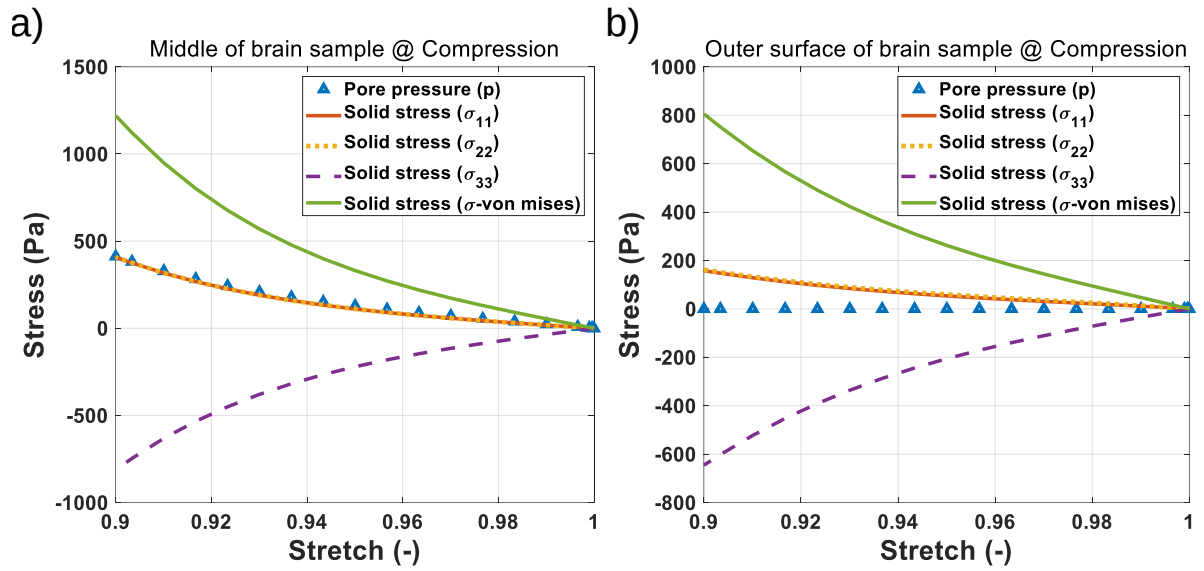

Figure 41. The predicted pore pressure in fluid phase, *p*, and stress components in solid matrix (σ_{11}, σ_{22}, σ_{33} and $\sigma_{\text{von-Mises}}$) versus compressive stretch, using poro-hyper viscoelastic material model for: a) middle, and b) outer surface of brain sample (Cortex).

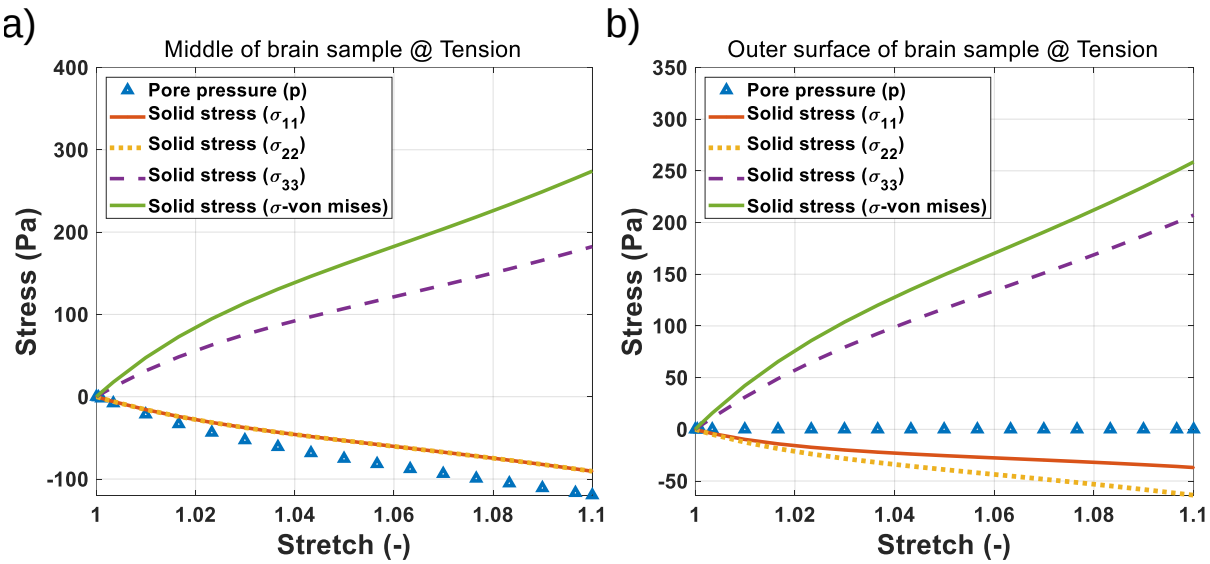

Figure 42. The predicted pore pressure in fluid phase, p, and stress components in solid matrix (σ_{11}, σ_{22}, σ_{33} and $\sigma_{\text{von-Mises}}$) versus tensile stretch, using poro-hyper viscoelastic material model for: a) middle, and b) outer surface of brain sample (Cortex).

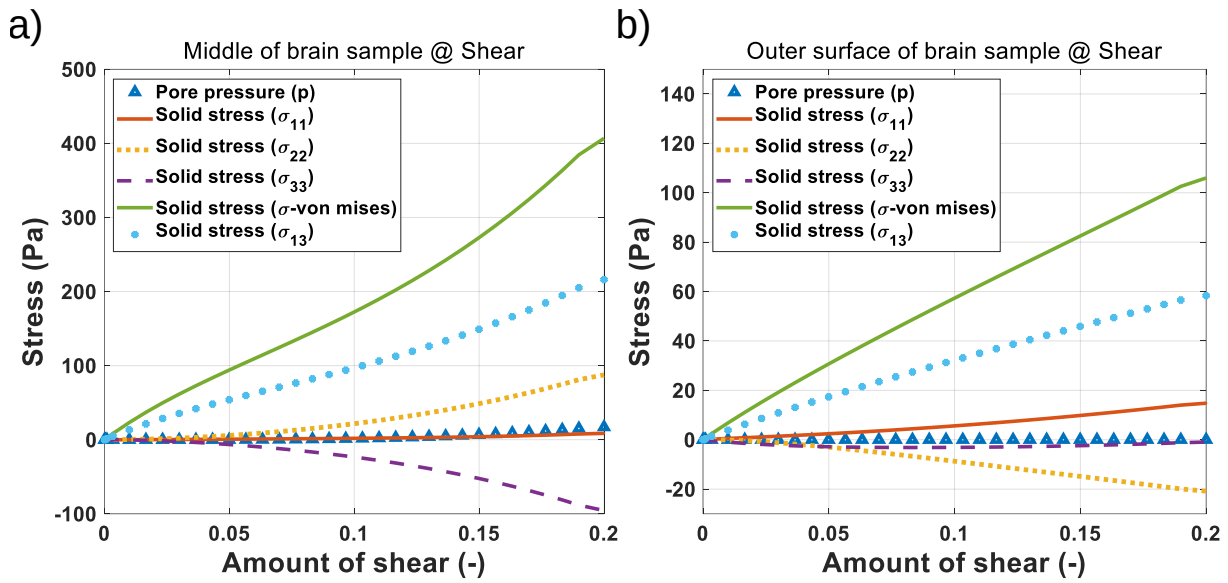

Figure 43. The predicted pore pressure in fluid phase, p, and stress components in solid matrix (σ_{11}, σ_{22}, σ_{33}, σ_{13} and $\sigma_{von\text{-}Mises}$) versus shear strain, using poro-hyper viscoelastic material model for: a) middle, and b) outer surface of brain sample (Cortex).

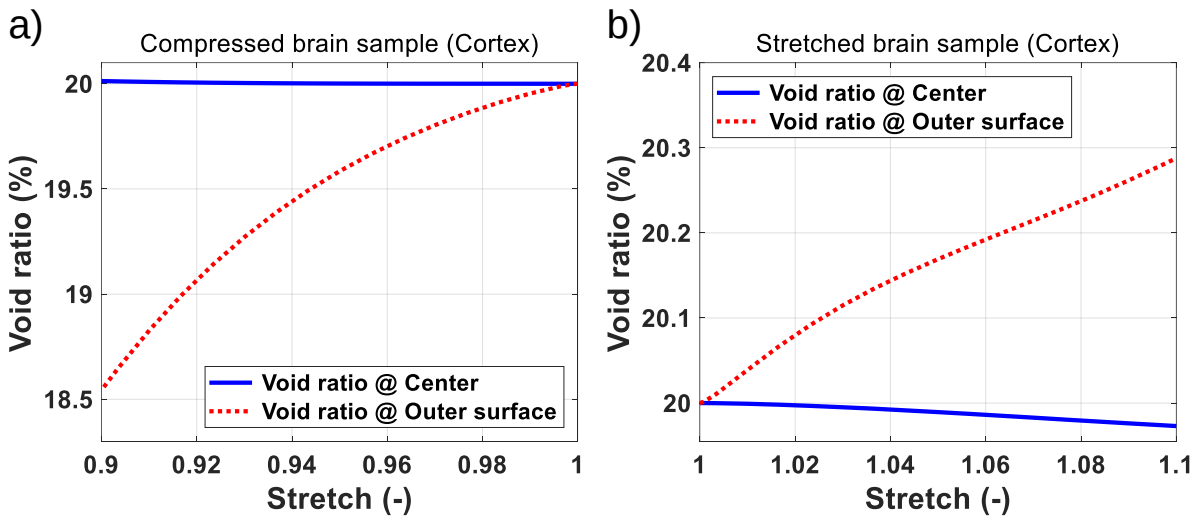

Figure 44. Variation of void ratio (%) at the middle and outer surface of brain specimen (Cortex) versus stretch under a) compressive, and b) tensile deformation.

Moreover, as depicted in Figure 45 a, and b, the void ratio at shear deformation was found to be in different pattern compared to unconfined compression and tension tests. This dissimilar distribution of void ratio was expected as the solid matrix experiences more non-uniform deformation at shear. The highest variations are estimated to happen for top and bottom corners of

this porous media. This finding indicates, for the associated simple shear test, under 0.2 of shear strain, the sample cortex will lose 13% concurrently and will attain more 6% void fractions at specific regions. However, at the same time very slight changes are noticed at the middle (far from the contact surfaces) of the brain samples.

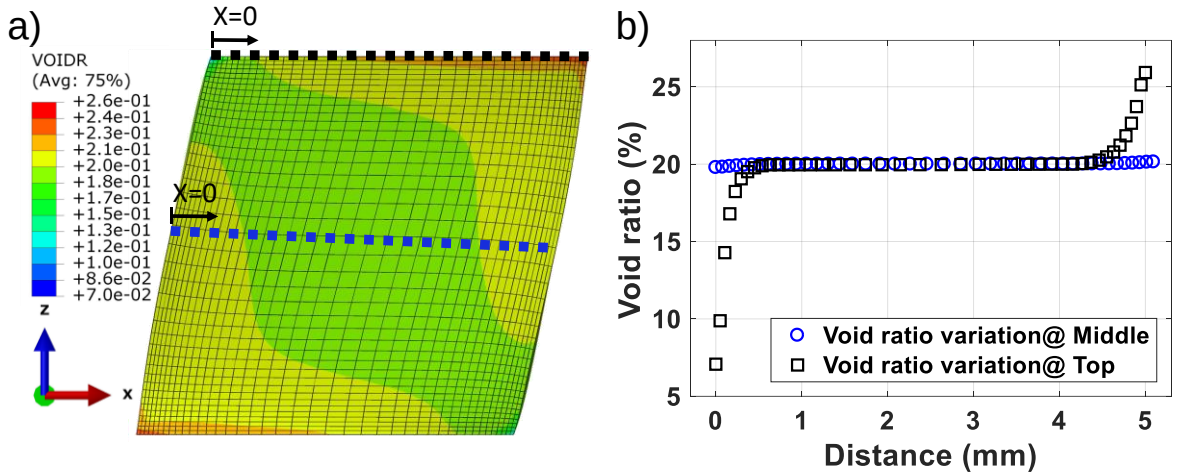

Figure 45. a) Distribution contour of void ratio for the brain sample (Cortex) under 0.2 shear strain, and b) the variation of void ratio (%) plotted of two selected paths at top and middle of the specimen.

Figure 46 a~d represents a model prediction of fluid phase flow for the brain (cortex) sample under 10% compressive deformation. As is depicted in this figure, the liquid contents have symmetrically transferred in “X-X” and “Y-Y” direction, perpendicular to the direction of applied force. Also, in all direction the effective flow velocity in the middle found to be significantly less than a point placed at outer surface of brain sample. Overall, the liquid velocity is not remarkable, confirming the earlier results, under compressive deformation the fluid contents are stuck between porous spaces induced in increasing the hydrostatic pressure. Also, these findings are in agreement with void ratio variations (see Figure 37-f for void ratio distribution in the brain specimen under compressive strain), showing the sample mainly possess a constant fluid volume fraction and barely a very limited liquid leaves the corner of the specimen. The highest estimated fluid flow under compression, was occurred at top and bottom corners of brain sample. The variation of fluid

velocity in the middle of brain sample and for a point at outer corner are illustrated and compared regarding tissue deformation in Figure 47 a and b.

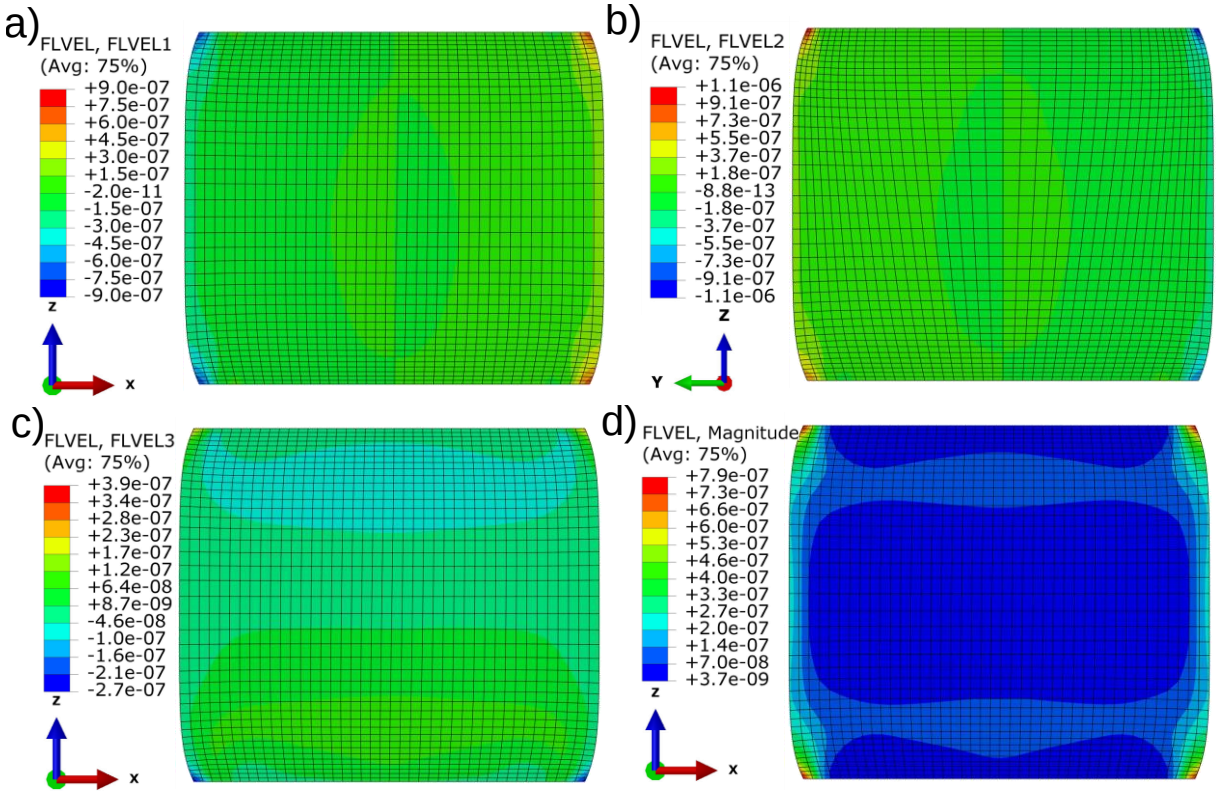

Figure 46. Demonstration of pore fluid effective velocity for brain (Cortex) sample, deformed under 10% compressive strain; present the velocity distribution at: a) "X-X" direction, b) "Y-Y" direction, c) "Z-Z" direction, and d) overall magnitude.

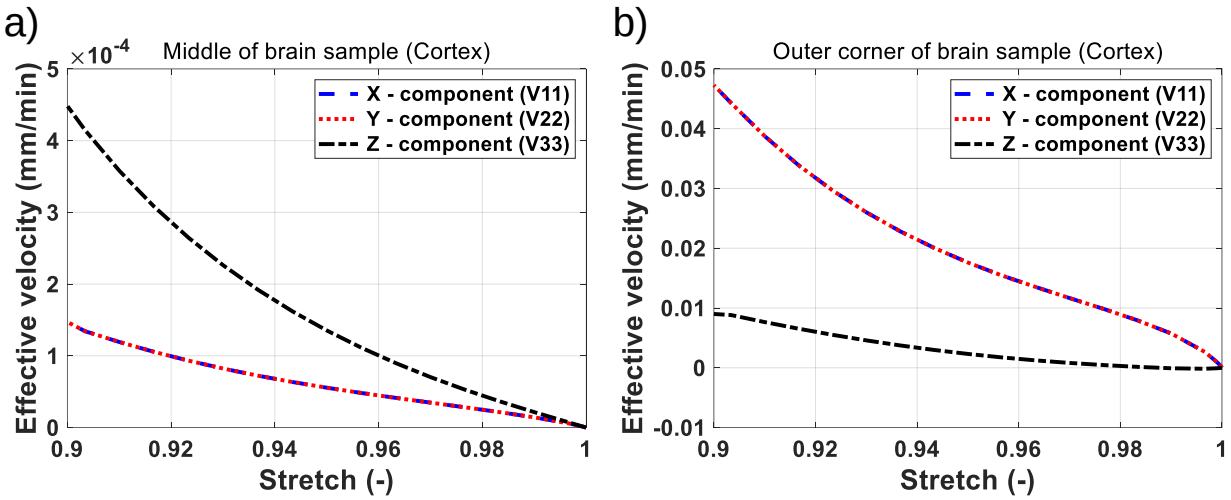

Figure 47. Variation of all velocity components for brain specimen (Cortex) under compression versus stretch for points placed at: d) middle and e) outer corner of sample.

6.4. Discussion

In the literature of biomechanics of brain, the poro-hyper viscoelastic model has not been established for this soft porous tissue yet. There are only some works devoted to studying the brain in a poro-elastic or poro-hyperelastic material model [14, 164]. The obtained constitutive parameters of the poro-hyper viscoelastic model presented in this study were successfully evaluated for different regions of the brain's gray and white mater. Each of instantaneous and relaxation experiments respectively exhibit a particular aspect of short-term and long-term viscoelastic behavior. In neurosurgical applications, we are interested in the instantaneous response of the brain, while the long-term relaxation response has a higher order of importance in drug delivery and brain development studies. Therefore, the material constants provided in Table 1, were calibrated to adequately represent the viscoelastic behavior of this biological tissues at low loading rates.

There is a lack of knowledge to describe why brain tissue is behaves differently for various loading conditions. More works are required to investigate the underlying microstructure of this tissue, the interaction between phases, their deformation pattern under different modes (i.e. compression, tension, and shear), or under different history (i.e. quasi-static, relaxation, and dynamic rates) to better characterize various phenomena such as: TBI, tissue swelling, hydrocephalus, brain development and drug delivery. In work presented here, the regional variation of the brain tissue was taken into account. Although, the effect of anisotropic properties was not explored in the original experimental study, it is recommended the solid matrix be defined as anisotropic material for more meticulous modeling. Also, a constant value was considered for the hydraulic conductivity (permeability), k, during the biphasic modeling of this porous medium. As the solid matrix deforms, the change in pore space induces a corresponding change in the

hydraulic conductivity of the medium. The alternative definition of anisotropic permeability expressed as a function of void ratio and kinematic viscosity of the wetting liquid allows the fully anisotropic modeling of this porous material.

6.5. Conclusion

The constitutive model parameters were calibrated by re-simulating the experimental procedure of the different tests in a developed finite elements model. Through an iterative simulation process, the computed results from the model are fully interpolated to the experimental data for basal ganglia ($R^2 \geq 0.96$), cortex ($R^2 \geq 0.94$), corpus callosum ($R^2 \geq 0.93$), and corona radiata ($R^2 \geq 0.96$). The model parameters are determined for different tissue response under various types of loading-boundary conditions. In addition to representing the complete mechanical response and deformation of solid phase, this biphasic model can demonstrate the flow and diffusion of the liquid through the tissue networks. The model can also express individual contribution of each phase with respect to the general behavior of the tissue. In the proposed model the material compressibility, time-dependency (viscoelasticity) behavior for short and long-term loading conditions have been considered. A reliable material stability for a feasible range of strain have also been checked. The identified material parameters from the model can be used in commercial finite elements packages with no customization. As the parameters are calibrated for low strain rates, it is advised to employ them in the examination of the brain under slow mechanical loadings of moderate time nature.

CHAPTER 7. CONCLUSIONS AND SUGGESTIONS FOR FUTURE WORKS

In this manuscript, in-vitro unconfined compression tests up to 30% nominal strain at intermediate to high-rate of deformations (10 to 1000 mm/sec) were conducted for bovine brain tissue. The significant effects for rate-dependent behavior of this soft biological tissue was observed. It was shown that the tissue demonstrated significant rate-dependency and by increasing the deformation rate, higher mechanical features i.e. the nominal stress and apparent elastic moduli were observed. In another step two different nature constitutive model were introduced to account for the rate-dependent behavior of this soft biologigal tissue. In one effort, a single-phase rate dependent constitutive relation was proposed and simultaneously calibrated with the measured data from three various deformation rates. The excellent correlations between the experimental, theoretical, and computational results has indicated that the proposed model was fully able to characterize brain tissue behavior and be employed in FE simulation.

In another effort, based on the nature of brain and the theory of porous media, a theoretical-computational framework for the biphasic modeling of this soft biological tissue was presented. The proposed biphasic viscoelastic model can demonstrate the flow and diffusion of the liquid through the tissue networks. The model can also express exclusive contribution of each phase concerning the general behavior of the tissue. Both solid and fluid phases of this model exhibited rate-dependent behavior. The very good agreements between the experimental, and computational results have indicated that the proposed model was fully able to characterize and be employed in FE simulation of the brain tissue. After calibrating and verifying the model for the bovine brain tissue, it was employed to determine the human brain tissue properties. Through an iterative simulation process, the computed results from the model are fully interpolated to the experimental

data for basal ganglia ($R^2 \geq 0.96$), cortex ($R^2 \geq 0.94$), corpus callosum ($R^2 \geq 0.93$), and corona radiata ($R^2 \geq 0.96$).

As a suggestion, efforts are required to develop microstructural based constitutive models that investigate the interactions between phases, their deformation pattern under different modes (i.e. compression, tension, and shear), or under different histories (i.e. quasi-static, relaxation, and dynamic rates) to comprehensively characterize various phenomena such as: TBI, tissue swelling, hydrocephalus, drug delivery and possibly brain development. In this current study, a constant value was considered as a simplified measure of the hydraulic conductivity during the entire deformation for this porous medium. While the solid matrix deforms, the distortion in pore space may generate a variation in the hydraulic conductivity [194-201]. For future work, further model refinement is required to address an alternative definition of permeability as a tensor expressed based on the changes in deformation and strain rates. In this thesis, finally we were able to determine the fluid diffusion inside the tissue solid network. The resulting flow of fluid at higher speeds can also disrupt cellular membranes and lead to subsequent damage or injury of the tissue. Under high deformation rates, e.g., as a result of head impact or blast waves, the liquid flows rapidly, resembling tiny waterjets between extracellular spaces, causing shear in the solid skeleton of brain tissue. This is a worthy subject, suggested to be study in future research. Also, studying the plastic deformation and damage-dependent constitutive modeling for brain tissue can be other suggestions for being considered in the further works.

REFERENCES

[1] Tse, K. M., Lim, S. P., Tan, V. B. C., and Lee, H. P., 2014, "A review of head injury and finite element head models," American Journal of Engineering, Technology and Society, 1(5), pp. 28-52.

[2] Bass, C. R., Panzer, M. B., Rafaels, K. A., Wood, G., Shridharani, J., and Capehart, B., 2012, "Brain injuries from blast," Annals of biomedical engineering, 40(1), pp. 185-202.

[3] Holbourn, A., 1943, "Mechanics of head injuries," The Lancet, 242(6267), pp. 438-441.

[4] O'riordain, K., Thomas, P., Phillips, J., and Gilchrist, M., 2003, "Reconstruction of real world head injury accidents resulting from falls using multibody dynamics," Clinical Biomechanics, 18(7), pp. 590-600.

[5] Rueda, M. F., and Gilchrist, M. D., 2009, "Comparative multibody dynamics analysis of falls from playground climbing frames," Forensic science international, 191(1), pp. 52-57.

[6] Faul, M., Xu, L., Wald, M. M., and Coronado, V. G., 2010, "Traumatic brain injury in the United States," Atlanta, GA: Centers for Disease Control and Prevention, National Center for Injury Prevention and Control.

[7] Meaney, D. F., Morrison, B., and Bass, C. D., 2014, "The mechanics of traumatic brain injury: a review of what we know and what we need to know for reducing its societal burden," Journal of biomechanical engineering, 136(2), p. 021008.

[8] Zhang, L., Yang, K. H., Dwarampudi, R., Omori, K., Li, T., Chang, K., Hardy, W. N., Khalil, T. B., and King, A. I., 2001, "Recent advances in brain injury research: a new human head model development and validation," Stapp Car Crash J, 45(11), pp. 369-394.

[9] Raul, J.-S., Baumgartner, D., Willinger, R., and Ludes, B., 2006, "Finite element modelling of human head injuries caused by a fall," International Journal of Legal Medicine, 120(4), pp. 212-218.

[10] Kleiven, S., 2007, "Predictors for traumatic brain injuries evaluated through accident reconstructions," Stapp car crash journal, 51, p. 81.

[11] Ho, J., and Kleiven, S., 2009, "Can sulci protect the brain from traumatic injury?," Journal of Biomechanics, 42(13), pp. 2074-2080.

[12] Ibrahim, N. G., and Margulies, S. S., 2010, "Biomechanics of the toddler head during low-height falls: an anthropomorphic dummy analysis," Journal of Neurosurgery: Pediatrics, 6(1), pp. 57-68.

[13] Giordano, C., Cloots, R., Van Dommelen, J., and Kleiven, S., 2014, "The influence of anisotropy on brain injury prediction," Journal of biomechanics, 47(5), pp. 1052-1059.

[14] Goriely, A., Geers, M. G., Holzapfel, G. A., Jayamohan, J., Jérusalem, A., Sivaloganathan, S., Squier, W., van Dommelen, J. A., Waters, S., and Kuhl, E., 2015, "Mechanics of the brain: perspectives, challenges, and opportunities," Biomechanics and modeling in mechanobiology, 14(5), pp. 931-965.

[15] Viano, D. C., Casson, I. R., Pellman, E. J., Zhang, L., King, A. I., and Yang, K. H., 2005, "Concussion in professional football: brain responses by finite element analysis: part 9," Neurosurgery, 57(5), pp. 891-916.

[16] Miller, K., 2011, Biomechanics of the Brain, Springer Science & Business Media.

[17] Nicolle, S., Lounis, M., and Willinger, R., 2004, "Shear properties of brain tissue over a frequency range relevant for automotive impact situations: new experimental results," SAE Technical Paper.

[18] Brands, D., Peters, G., and Bovendeerd, P., 2004, "Design and numerical implementation of a 3-D non-linear viscoelastic constitutive model for brain tissue during impact," Journal of biomechanics, 37(1), pp. 127-134.

[19] Farid, M. H., Eslaminejad, A., Ramzanpour, M., Ziejewski, M., and Karami, G., "The Strain Rates of the Brain and Skull Under Dynamic Loading," Proc. ASME 2018 International Mechanical Engineering Congress and Exposition, American Society of Mechanical Engineers, pp. V003T004A067-V003T004A067.

[20] Eslaminejad, A., Hosseini Farid, M., Ziejewski, M., and Karami, G., 2018, "Brain tissue constituive material models and the finite element analysis of blast-induced traumatic brain injury," Scientia Iranica, 25, pp. 3141-3150.

[21] Ramzanpour, M., Eslaminejad, A., Hosseini-Farid, M., Ziejewski, M., and Karami, G., 2018, "Comparative study of coup and contrecoup brain injury in impact induced TBI," Biomedical Sciences Instrumentation, 54(1), pp. 76-82.

[22] Farid, M. H., Eslaminejad, A., Ziejewski, M., and Karami, G., "Biomechanical modelling of youngsters head impact by sporting balls," Proc. BRAIN INJURY, TAYLOR & FRANCIS INC 530 WALNUT STREET, STE 850, PHILADELPHIA, PA 19106 USA, pp. 937-937.

[23] Eslaminejad, A., Hosseini Farid, M., Ziejewski, M., and Karami, G., 2018, "Brain Tissue Constitutive Material Models and the Finite Element Analysis of Blast-Induced Traumatic Brain Injury," Scientia Iranica, 25 , pp. 3141-3150.

[24] Dumpuri, P., Thompson, R. C., Dawant, B. M., Cao, A., and Miga, M. I., 2007, "An atlas-based method to compensate for brain shift: Preliminary results," Medical Image Analysis, 11(2), pp. 128-145.

[25] Miller, K., Chinzei, K., Orssengo, G., and Bednarz, P., 2000, "Mechanical properties of brain tissue in-vivo: experiment and computer simulation," Journal of biomechanics, 33(11), pp. 1369-1376.

[26] Wirth, B., and Sobey, I., 2008, "Analytic solution during an infusion test of the linear unsteady poroelastic equations in a spherically symmetric model of the brain," Mathematical medicine and biology: a journal of the IMA, 26(1), pp. 25-61.

[27] Støverud, K. H., Darcis, M., Helmig, R., and Hassanizadeh, S. M., 2012, "Modeling concentration distribution and deformation during convection-enhanced drug delivery into brain tissue," Transport in porous media, 92(1), pp. 119-143.

[28] Linninger, A. A., Somayaji, M. R., Erickson, T., Guo, X., and Penn, R. D., 2008, "Computational methods for predicting drug transport in anisotropic and heterogeneous brain tissue," Journal of biomechanics, 41(10), pp. 2176-2187.

[29] Angeli, S., and Stylianopoulos, T., 2016, "Biphasic modeling of brain tumor biomechanics and response to radiation treatment," Journal of biomechanics, 49(9), pp. 1524-1531.

[30] Guo, L., Vardakis, J. C., Lassila, T., Mitolo, M., Ravikumar, N., Chou, D., Lange, M., Sarrami-Foroushani, A., Tully, B. J., and Taylor, Z. A. J. I. f., 2018, "Subject-specific multi-poroelastic model for exploring the risk factors associated with the early stages of Alzheimer's disease," 8(1), p. 20170019.

[31] Eslaminejad, A., Farid, M. H., Ziejewski, M., Karami, G., and Moghaddam, H. S., "Cerebrospinal fluid (CSF) and vibration of skull in acoustical analysis of the human head to monitor brain ICP," Proc. Brain Injury, Taylor & Francis Inc 530 Walnut Street, ste 850, Philadelphia, PA 19106 USA, pp. 787-787.

[32] Eslaminejad, A., Ramzanpour, M., Hosseini-Farid, M., Ziejewski, M., and Karami, G., 2018, "cerebrospinal fluid-skull interaction analysis for a non-invasive intracranial monitoring technique," Biomedical Sciences Instrumentation 54 (1), pp. 69-75

[33] Eslaminejad, A., Sarvghad-Moghaddam, H., Rezaei, A., Ziejewski, M., and Karami, G., "Comparison of Brain Tissue Material Finite Element Models Based On Threshold for Traumatic Brain Injury," Proc. ASME 2016 International Mechanical Engineering Congress and Exposition, American Society of Mechanical Engineers, pp. V003T004A041-V003T004A041.

[34] Chatelin, S., Constantinesco, A., and Willinger, R., 2010, "Fifty years of brain tissue mechanical testing: from in vitro to in vivo investigations," Biorheology, 47(5-6), pp. 255-276.

[35] Fallenstein, G., Hulce, V. D., and Melvin, J. W., 1969, "Dynamic mechanical properties of human brain tissue," Journal of Biomechanics, 2(3), pp. 217-226.

[36] Galford, J. E., and McElhaney, J. H., 1970, "A viscoelastic study of scalp, brain, and dura," Journal of biomechanics, 3(2), pp. 211-221.

[37] Estes, M., and JH, M., "Response of brain tissue to compressive loading," Proc. Mechanical Engineering, ASME-AMER SOC MECHANICAL ENG 345 E 47TH ST, NEW YORK, NY 10017, pp. 58-&.

[38] Bilston, L. E., Liu, Z., and Phan-Thien, N., 2001, "Large strain behaviour of brain tissue in shear: some experimental data and differential constitutive model," Biorheology, 38(4), pp. 335-345.

[39] Gefen, A., and Margulies, S. S., 2004, "Are in vivo and in situ brain tissues mechanically similar?," Journal of biomechanics, 37(9), pp. 1339-1352.

[40] Franceschini, G., Bigoni, D., Regitnig, P., and Holzapfel, G. A., 2006, "Brain tissue deforms similarly to filled elastomers and follows consolidation theory," Journal of the Mechanics and Physics of Solids, 54(12), pp. 2592-2620.

[41] Chatelin, S., Vappou, J., Roth, S., Raul, J.-S., and Willinger, R., 2012, "Towards child versus adult brain mechanical properties," Journal of the mechanical behavior of biomedical materials, 6, pp. 166-173.

[42] Budday, S., Nay, R., de Rooij, R., Steinmann, P., Wyrobek, T., Ovaert, T. C., and Kuhl, E., 2015, "Mechanical properties of gray and white matter brain tissue by indentation," Journal of the mechanical behavior of biomedical materials, 46, pp. 318-330.

[43] Budday, S., Sommer, G., Birkl, C., Langkammer, C., Haybaeck, J., Kohnert, J., Bauer, M., Paulsen, F., Steinmann, P., and Kuhl, E., 2017, "Mechanical characterization of human brain tissue," Acta biomaterialia, 48, pp. 319-340.

[44] Prange, M. T., and Margulies, S. S., 2002, "Regional, directional, and age-dependent properties of the brain undergoing large deformation," Journal of biomechanical engineering, 124(2), pp. 244-252.

[45] Elkin, B. S., Ilankovan, A., and Morrison, B., 2010, "Age-dependent regional mechanical properties of the rat hippocampus and cortex," Journal of biomechanical engineering, 132(1), p. 011010.

[46] Elkin, B. S., Ilankova, A., and Morrison, B., 2011, "Dynamic, regional mechanical properties of the porcine brain: indentation in the coronal plane," Journal of biomechanical engineering, 133(7), p. 071009.

[47] Zhang, J., Yoganandan, N., Pintar, F. A., Guan, Y., Shender, B., Paskoff, G., and Laud, P., 2011, "Effects of tissue preservation temperature on high strain-rate material properties of brain," Journal of Biomechanics, 44(3), pp. 391-396.

[48] Anderson, A. T., Van Houten, E. E., McGarry, M. D., Paulsen, K. D., Holtrop, J. L., Sutton, B. P., Georgiadis, J. G., and Johnson, C. L., 2016, "Observation of direction-dependent mechanical properties in the human brain with multi-excitation MR elastography," journal of the mechanical behavior of biomedical materials, 59, pp. 538-546.

[49] Shojaeiarani, J., Bajwa, D., Rehovsky, C., Bajwa, S., and Vahidi, G., 2019, "Deterioration in the Physico-Mechanical and Thermal Properties of Biopolymers Due to Reprocessing," Polymers, 11(1), p. 58.

[50] Panahi, A. K., Mianajiy, H., Miandoabchi, E., and Fareed, M. H., 2013, "Optimization of the Powder Injection Molding Process Parameters Using the Sequential Simplex Algorithm and Sensitivity Analysis," Journal of Manufacturing Science and Engineering, 135(1), p. 011006.

[51] Miller, K., and Chinzei, K., 1997, "Constitutive modeling of brain tissue: experiment and theory," Journal of Biomechanics, 30, pp. 1115-1121.

[52] Kohandel, M., Sivaloganathan, S., Tenti, G., and Drake, J. M., 2006, "The constitutive properties of the brain parenchyma Part 1. Strain energy approach," Medical Engineering & Physics, 28, pp. 449-454.

[53] de Rooij, R., and Kuhl, E., 2016, "Constitutive modeling of brain tissue: current perspectives," Applied Mechanics Reviews, 68(1), p. 010801.

[54] El Sayed, T., Mota, A., Fraternali, F., and Ortiz, M., 2008, "A variational constitutive model for soft biological tissues," Journal of biomechanics, 41(7), pp. 1458-1466.

[55] Meyers, M. A., and Chawla, K. K., 2009, Mechanical behavior of materials, Cambridge University Press Cambridge.

[56] Miller, K., and Chinzei, K., 2002, "Mechanical properties of brain tissue in tension," Journal of biomechanics, 35(4), pp. 483-490.

[57] Zhao, H., Yin, Z., Li, K., Liao, Z., Xiang, H., and Zhu, F., 2016, "Mechanical characterization of immature porcine brainstem in tension at dynamic strain rates," Medical science monitor basic research, 22, p. 6.

[58] Rashid, B., Destrade, M., and Gilchrist, M. D., 2014, "Mechanical characterization of brain tissue in tension at dynamic strain rates," Journal of the mechanical behavior of biomedical materials, 33, pp. 43-54.

[59] Rashid, B., Destrade, M., and Gilchrist, M. D., 2012, "Mechanical characterization of brain tissue in compression at dynamic strain rates," Journal of the Mechanical Behavior of Biomedical Materials, 10, pp. 23-38.

[60] Cheng, S., and Bilston, L. E., 2007, "Unconfined compression of white matter," Journal of biomechanics, 40(1), pp. 117-124.

[61] Laksari, K., Shafieian, M., and Darvish, K., 2012, "Constitutive model for brain tissue under finite compression," Journal of Biomechanics, 45, pp. 642-646.

[62] Farid, M. H., Eslaminejad, A., Ziejewski, M., and Karami, G., "A Study on the Effects of Strain Rates on Characteristics of Brain Tissue," Proc. ASME 2017 International Mechanical Engineering Congress and Exposition, American Society of Mechanical Engineers, pp. V003T004A003-V003T004A003.

[63] Shuck, L., and Advani, S., 1972, "Rheological response of human brain tissue in shear," Journal of basic engineering, 94(4), pp. 905-911.

[64] Darvish, K., and Crandall, J., 2001, "Nonlinear viscoelastic effects in oscillatory shear deformation of brain tissue," Medical engineering & physics, 23(9), pp. 633-645.

[65] Okamoto, R. J., Feng, Y., Genin, G. M., and Bayly, P. V., "Anisotropic Behavior of White Matter in Shear and Implications for Transversely Isotropic Models," Proc. ASME 2013 Summer Bioengineering Conference, American Society of Mechanical Engineers, pp. V01AT10A002-V001AT010A002.

[66] Destrade, M., Gilchrist, M., Murphy, J. G., Rashid, B., and Saccomandi, G., 2015, "Extreme softness of brain matter in simple shear," International Journal of Non-Linear Mechanics, 75, pp. 54-58.

[67] Bilston, L. E., 2011, Neural tissue biomechanics, Springer Science & Business Media.

[68] Mihai, L. A., Budday, S., Holzapfel, G. A., Kuhl, E., and Goriely, A., 2017, "A family of hyperelastic models for human brain tissue," Journal of the Mechanics and Physics of Solids, 106, pp. 60-79.

[69] Forte, A. E., Gentleman, S. M., and Dini, D., 2017, "On the characterization of the heterogeneous mechanical response of human brain tissue," Biomechanics and modeling in mechanobiology, 16(3), pp. 907-920.

[70] Alain Goriely, S. B., Ellen Kuhl, 2015, Neuromechanics: From Neurons to Brain, Advances in Applied Mechanics.

[71] Bilston, L. E., Liu, Z., and Phan-Thien, N., 1997, "Linear viscoelastic properties of bovine brain tissue in shear," Biorheology, 34(6), pp. 377-385.

[72] Willinger, R. m., Taleb, L., and Kopp, C., 1995, "Modal and temporal analysis of head mathematical models," Journal of neurotrauma, 12(4), pp. 743-754.

[73] Willinger, R., Kang, H.-S., and Diaw, B., 1999, "Three-dimensional human head finite-element model validation against two experimental impacts," Annals of biomedical engineering, 27(3), pp. 403-410.

[74] Morrison III, B., Cater, H. L., Wang, C. C., and Thomas, F. C., 2003, "A tissue level tolerance criterion for living brain developed with an in vitro model of traumatic mechanical loading," Stapp Car Crash Journal, 47, p. 93.

[75] Velardi, F., Fraternali, F., and Angelillo, M., 2006, "Anisotropic constitutive equations and experimental tensile behavior of brain tissue," Biomechanics and modeling in mechanobiology, 5(1), pp. 53-61.

[76] Nolan, D., Gower, A., Destrade, M., Ogden, R., and McGarry, J., 2014, "A robust anisotropic hyperelastic formulation for the modelling of soft tissue," Journal of the mechanical behavior of biomedical materials, 39, pp. 48-60.

[77] Sahoo, D., Deck, C., and Willinger, R., 2014, "Development and validation of an advanced anisotropic visco-hyperelastic human brain FE model," journal of the mechanical behavior of biomedical materials, 33, pp. 24-42.

[78] Karami, G., Grundman, N., Abolfathi, N., Naik, A., and Ziejewski, M., 2009, "A micromechanical hyperelastic modeling of brain white matter under large deformation," Journal of the mechanical behavior of biomedical materials, 2(3), pp. 243-254.

[79] Kaster, T., Sack, I., and Samani, A., 2011, "Measurement of the hyperelastic properties of ex vivo brain tissue slices," Journal of biomechanics, 44(6), pp. 1158-1163.

[80] Moran, R., Smith, J. H., and García, J. J., 2014, "Fitted hyperelastic parameters for Human brain tissue from reported tension, compression, and shear tests," Journal of biomechanics, 47(15), pp. 3762-3766.

[81] Mihai, L. A., Chin, L., Janmey, P. A., and Goriely, A., 2015, "A comparison of hyperelastic constitutive models applicable to brain and fat tissues," Journal of The Royal Society Interface, 12(110), p. 20150486.

[82] Wex, C., Arndt, S., Stoll, A., Bruns, C., and Kupriyanova, Y., 2015, "Isotropic incompressible hyperelastic models for modelling the mechanical behaviour of biological tissues: a review," Biomedical Engineering/Biomedizinische Technik, 60(6), pp. 577-592.

[83] Mihai, L. A., Budday, S., Holzapfel, G. A., Kuhl, E., and Goriely, A., 2017, "A family of hyperelastic models for human brain tissue," Journal of the Mechanics and Physics of Solids.

[84] Zhang, L., Yang, K. H., and King, A. I., 2004, "A proposed injury threshold for mild traumatic brain injury," Transactions-American Society of Mechanical Engineers Journal of Biomechanical Engineering, 126(2), pp. 226-236.

[85] Viano, D. C., and Lovsund, P., 1999, "Biomechanics of brain and spinal-cord injury: Analysis of neuropathologic and neurophysiology experiments," Traffic Injury Prevention, 1(1), pp. 35-43.

[86] Rashid, B., Destrade, M., and Gilchrist, M. D., 2013, "Mechanical characterization of brain tissue in simple shear at dynamic strain rates," Journal of the mechanical behavior of biomedical materials, 28, pp. 71-85.

[87] Hosseini-Farid, M., Ramzanpour, M., Eslaminejad, A., Ziejewski, M., and Karami, G., 2018, "Computational Simulation of Brain Injury by Golf Ball Impacts in Adult and Children," Biomedical Sciences Instrumentation, 54(1), pp. 369-376.

[88] Eslaminejad, A., Hosseini-Farid, M., Ramzanpour, M., Ziejewski, M., and Karami, G., "Determination of Mechanical Properties of Human Skull With Modal Analysis," Proc. ASME 2018 International Mechanical Engineering Congress and Exposition, American Society of Mechanical Engineers, pp. V003T004A097-V003T004A097.

[89] Eslaminejad, A., Ziejewski, M., and Karami, G., 2019, "An experimental–numerical modal analysis for the study of shell-fluid interactions in a clamped hemispherical shell," Applied Acoustics, 152, pp. 110-117.

[90] Hosseini-Farid, M., Eslaminejad, A., Ziejewski, M., and Karami, G., "Finite Element Simulation of Head Impacted by Ball for Adult and Youth," Proc. 12th World Congress on Brain Injury.

[91] Hosseini-Farid, M., Rezaei, A., Eslaminejad, A., Ramzanpour, M., Ziejewski, M., and Karami, G., 2019, "Instantaneous and Equilibrium Responses of the Brain Tissue by Stress Relaxation and Quasi-Linear Viscoelasticity Theory," Scientia Iranica, http://dx.doi.org/10.24200/SCI.2019.21314.

[92] Rezaei, A., Sarvghad-Moghaddam, H., Eslaminejad, A., Ziejewski, M., and Karami, G., "Skull Deformation Has No Impact on the Variation of Brain Intracranial Pressure," Proc. ASME 2016 International Mechanical Engineering Congress and Exposition, American Society of Mechanical Engineers, pp. V003T004A042-V003T004A042.

[93] Eslaminejad, A., Ziejewski, M., and Karami, G., 2019, "Vibrational Properties of a Hemispherical Shell with Its Inner Fluid Pressure: An Inverse Method for Noninvasive Intracranial Pressure Monitoring," Journal of Vibration and Acoustics, 141(4), p. 041002.

[94] Hosseini-Farid, M., Ramzanpour, M., Ziejewski, M., and Karami, G., 2018, "Estimating the Brain Strain Rates During Traumatic Brain Injury," Biomedical Sciences Instrumentation, 54(1), pp. 361-368.

[95] Ning, X., Zhu, Q., Lanir, Y., and Margulies, S. S., 2006, "A transversely isotropic viscoelastic constitutive equation for brainstem undergoing finite deformation," Journal of biomechanical engineering, 128(6), pp. 925-933.

[96] Arbogast, K. B., and Margulies, S. S., 1999, "A fiber-reinforced composite model of the viscoelastic behavior of the brainstem in shear," Journal of biomechanics, 32(8), pp. 865-870.

[97] McElhaney, J. H., Fogle, J. L., Melvin, J. W., Haynes, R. R., Roberts, V. L., and Alem, N. M., 1970, "Mechanical properties of cranial bone," Journal of biomechanics, 3(5), pp. 495-511.

[98] Motherway, J. A., Verschueren, P., Van der Perre, G., Vander Sloten, J., and Gilchrist, M. D., 2009, "The mechanical properties of cranial bone: the effect of loading rate and cranial sampling position," Journal of biomechanics, 42(13), pp. 2129-2135.

[99] Persson, C., Evans, S., Marsh, R., Summers, J. L., and Hall, R. M., 2010, "Poisson's ratio and strain rate dependency of the constitutive behavior of spinal dura mater," Annals of biomedical engineering, 38(3), pp. 975-983.

[100] Maikos, J. T., Elias, R. A., and Shreiber, D. I., 2008, "Mechanical properties of dura mater from the rat brain and spinal cord," Journal of neurotrauma, 25(1), pp. 38-51.

[101] De Kegel, D., Vastmans, J., Fehervary, H., Depreitere, B., Vander Sloten, J., and Famaey, N., 2018, "Biomechanical characterization of human dura mater," Journal of the mechanical behavior of biomedical materials, 79, pp. 122-134.

[102] Wood, J. L., 1971, "Dynamic response of human cranial bone," Journal of biomechanics, 4(1), pp. IN1-IN3.

[103] Ghajari, M., Hellyer, P. J., and Sharp, D. J., 2017, "Computational modelling of traumatic brain injury predicts the location of chronic traumatic encephalopathy pathology," Brain, 140(2), pp. 333-343.

[104] Patton, D. A., McIntosh, A. S., Kleiven, S., and Frechede, B., 2012, "Injury data from unhelmeted football head impacts evaluated against critical strain tolerance curves," Proceedings of the Institution of Mechanical Engineers, Part P: Journal of Sports Engineering and Technology, 226(3-4), pp. 177-184.

[105] Rezaei, A., Salimi Jazi, M., Karami, G., and Ziejewski, M., 2014, "A computational study on brain tissue under blast: primary and tertiary blast injuries," International journal for numerical methods in biomedical engineering, 30(8), pp. 781-795.

[106] Horgan, T., and Gilchrist, M. D., 2003, "The creation of three-dimensional finite element models for simulating head impact biomechanics," International Journal of Crashworthiness, 8(4), pp. 353-366.

[107] Nahum, A. M., Smith, R., and Ward, C. C., 1977, "Intracranial pressure dynamics during head impact," No. 0148-7191, SAE Technical Paper.

[108] Lee, H. P., and Wang, F., 2010, "Assessment of head injury of children due to golf ball impact," Computer methods in biomechanics and biomedical engineering, 13(5), pp. 523-535.

[109] Ridenour, M. V., 1998, "Golf clubs: hidden home hazard for children," Perceptual and motor skills, 86(3), pp. 747-753.

[110] Bait, M. E., 1993, "Golfing injuries," Sports Medicine, 16(1), pp. 64-71.

[111] Salimi Jazi, M., Rezaei, A., Karami, G., and Azarmi, F., 2014, "Biomechanical parameters of the brain under blast loads with and without helmets," International Journal of Experimental and Computational Biomechanics, 2(3), pp. 223-244.

[112] Rezaei, A., Salimi Jazi, M., and Karami, G., 2014, "Computational modeling of human head under blast in confined and open spaces: primary blast injury," International journal for numerical methods in biomedical engineering, 30(1), pp. 69-82.

[113] Salimi Jazi, M., Rezaei, A., Karami, G., Azarmi, F., and Ziejewski, M., 2014, "A computational study of influence of helmet padding materials on the human brain under ballistic impacts," Computer methods in biomechanics and biomedical engineering, 17(12), pp. 1368-1382.

[114] Dobratz, B., and Crawford, P., 1981, "Properties of Chemical Explosives & Explosives Stimulants, LLNL Explosive Handbook," Lawrence Livermore National Laboratory, University of California Report UCRL-52997.

[115] Miller, K., and Chinzei, K., 1997, "Constitutive modelling of brain tissue: experiment and theory," Journal of biomechanics, 30(11), pp. 1115-1121.

[116] Jahani, B., Salimi Jazi, M., Azarmi, F., and Croll, A., 2018, "Effect of volume fraction of reinforcement phase on mechanical behavior of ultra-high-temperature composite consisting of iron matrix and TiB2 particulates," Journal of Composite Materials, 52(5), pp. 609-620.

[117] Pervin, F., and Chen, W. W., 2009, "Dynamic mechanical response of bovine gray matter and white matter brain tissues under compression," Journal of Biomechanics, 42(6), pp. 731-735.

[118] Anderson, P. S., 2018, "Making a point: shared mechanics underlying the diversity of biological puncture," Journal of Experimental Biology, 221(22), p. jeb187294.

[119] Jahani, B., 2016, "Development of an Advanced Composite Material Consisting of Iron Matrix Reinforced with Ultra High Temperature Ceramic Particulate (TiB2) with Optimum Properties," North Dakota State University.

[120] Saboori, P., and Walker, G., 2019, "Brain injury and impact characteristics," Annals of biomedical engineering, pp. 1-11.

[121] Ratajczak, M., Ptak, M., Chybowski, L., Gawdzińska, K., and Będziński, R., 2019, "Material and Structural Modeling Aspects of Brain Tissue Deformation under Dynamic Loads," Materials, 12(2), p. 271.

[122] Mendis, K. K., Stalnaker, R. K., and Advani, S. H., 1995, "A constitutive relationship for large deformation finite element modeling of brain tissue," Journal of Biomechanical Engineering, 117, pp. 279-285.

[123] Miller, K., 1999, "Constitutive model of brain tissue suitable for finite element analysis of surgical procedures," Journal of biomechanics, 32(5), pp. 531-537.

[124] Farahmand, F., and Ahmadian, M., 2018, "A novel procedure for micromechanical characterization of white matter constituents at various strain rates," Scientia Iranica, p. http://dx.doi.org/10.24200/SCI.22018.50940.21928.

[125] Prevost, T. P., Balakrishnan, A., Suresh, S., and Socrate, S., 2011, "Biomechanics of brain tissue," Acta Biomaterialia, 7(1), pp. 83-95.

[126] Haldar, K., and Pal, C., 2018, "Rate dependent anisotropic constitutive modeling of brain tissue undergoing large deformation," Journal of the mechanical behavior of biomedical materials, 81, pp. 178-194.

[127] Bergstrom, J. S., 2015, Mechanics of solid polymers: theory and computational modeling, William Andrew.

[128] Ogden, R. W., 1997, Non-linear elastic deformations, Courier Corporation.

[129] Ogden, R. W., "Large deformation isotropic elasticity–on the correlation of theory and experiment for incompressible rubberlike solids," Proc. Proc. R. Soc. Lond. A, The Royal Society, pp. 565-584.

[130] Ogden, R., 1986, "Recent advances in the phenomenological theory of rubber elasticity," Rubber Chemistry and Technology, 59(3), pp. 361-383.

[131] Quintavalla, S., and Johnson, S., 2004, "Extension of the Bergstrom-Boyce model to high strain rates," Rubber Chemistry and Technology, 77(5), pp. 972-981.

[132] Boyce, M. C., Weber, G., and Parks, D. M., 1989, "On the kinematics of finite strain plasticity," Journal of the Mechanics and Physics of Solids, 37(5), pp. 647-665.

[133] Hurtado, J., Lapczyk, I., and Govindarajan, S., 2013, "Parallel rheological framework to model non-linear viscoelasticity, permanent set, and Mullins effect in elastomers," Constitutive Models for Rubber VIII, 95, pp. 95-100.

[134] Lee, E. H., 1969, "Elastic-plastic deformation at finite strains," Journal of applied mechanics, 36(1), pp. 1-6.

[135] Dafalias, Y., 1986, "Erratum:“The Plastic Spin”(Journal of Applied Mechanics, 1985, 52, pp. 865–871)," Journal of Applied Mechanics, 53(2), pp. 290-290.

[136] Jahani, B., Brooks, A., and Azarmi, F., 2018, "Development of antibacterial surfaces via thermal spray coating techniques," Biomed. Sci. Instrum, 54(1).

[137] Jaishankar, A., and McKinley, G. H., 2013, "Power-law rheology in the bulk and at the interface: quasi-properties and fractional constitutive equations," Proceedings of the Royal Society A: Mathematical, Physical and Engineering Sciences, 469(2149), p. 20120284.

[138] Dalrymple, T., Hurtado, J., Lapczyk, I., and Ahmadi, H., 2015, "Parallel Rheological Framework to model the amplitude dependence of the dynamic stiffness in carbon-black filled rubber," Constitutive Models for Rubber IX, p. 189.

[139] Ghoreishy, M. H. R., and Sourki, F. A., 2018, "Development of a new combined numerical/experimental approach for the modeling of the nonlinear hyper-viscoelastic behavior of highly carbon black filled rubber compound," Polymer Testing, 70, pp. 135-143.

[140] Bergström, J., and Boyce, M., 2001, "Constitutive modeling of the time-dependent and cyclic loading of elastomers and application to soft biological tissues," Mechanics of materials, 33(9), pp. 523-530.

[141] Pamidi, M., and Advani, S., 1978, "Nonlinear constitutive relations for human brain tissue," Journal of Biomechanical Engineering, 100(1), pp. 44-48.

[142] Hrapko, M., van Dommelen, J. A. W., Peters, G. W. M., and Wismans, J. S. H. M., 2006, "The mechanical behaviour of brain tissue: large strain response and constitutive modeling," Biorheology, 43, pp. 623-636.

[143] Hrapko, M., Van Dommelen, J., Peters, G., and Wismans, J., 2009, "On the consequences of non linear constitutive modelling of brain tissue for injury prediction with numerical head models," International journal of crashworthiness, 14(3), pp. 245-257.

[144] El Sayed, T., Mota, A., Fraternali, F., and Ortiz, M., 2008, "Biomechanics of traumatic brain injury," Computer Methods in Applied Mechanics and Engineering, 197(51-52), pp. 4692-4701.

[145] Tamura, A., Hayashi, S., Watanabe, I., Nagayama, K., and Matsumoto, T., 2007, "Mechanical characterization of brain tissue in high-rate compression," Journal of biomechanical science and engineering, 2(3), pp. 115-126.

[146] Donnelly, B., and Medige, J., 1997, "Shear properties of human brain tissue," Journal of biomechanical engineering, 119(4), pp. 423-432.

[147] Barry, S., and Aldis, G., 1990, "Comparison of models for flow induced deformation of soft biological tissue," Journal of biomechanics, 23(7), pp. 647-654.

[148] Kyriacou, S. K., Mohamed, A., Miller, K., and Neff, S., 2002, "Brain mechanics for neurosurgery: modeling issues," Biomechanics and modeling in mechanobiology, 1(2), pp. 151-164.

[149] Howell, B., and McIntyre, C. C., 2017, "Role of soft-tissue heterogeneity in computational models of deep brain stimulation," Brain stimulation, 10(1), pp. 46-50.

[150] Tallinen, T., Chung, J. Y., Rousseau, F., Girard, N., Lefèvre, J., and Mahadevan, L., 2016, "On the growth and form of cortical convolutions," Nature Physics, 12, p. 588.

[151] MacManus, D. B., Pierrat, B., Murphy, J. G., and Gilchrist, M. D., 2017, "Region and species dependent mechanical properties of adolescent and young adult brain tissue," Scientific reports, 7(1), p. 13729.

[152] Holland, M. A., Miller, K. E., and Kuhl, E., 2015, "Emerging brain morphologies from axonal elongation," Annals of biomedical engineering, 43(7), pp. 1640-1653.

[153] Javid, S., Rezaei, A., and Karami, G., 2014, "A micromechanical procedure for viscoelastic characterization of the axons and ECM of the brainstem," Journal of the Mechanical Behavior of Biomedical Materials, 30, pp. 290-299.

[154] Elliott, N., Bertram, C., Martin, B. A., and Brodbelt, A., 2013, "Syringomyelia: a review of the biomechanics," Journal of Fluids and Structures, 40, pp. 1-24.

[155] Ehlers, W., and Wagner, A., 2018, "Multiscale Aspects in the Multiphasic Modelling of Human Brain Tissue," Biomedical Technology, Springer, pp. 3-13.

[156] Pountney, T. E., 2007, Physiotherapy for children, Elsevier Health Sciences.

[157] Haslach Jr, H. W., Leahy, L. N., Riley, P., Gullapalli, R., Xu, S., and Hsieh, A. H., 2014, "Solid–extracellular fluid interaction and damage in the mechanical response of rat brain tissue under confined compression," journal of the mechanical behavior of biomedical materials, 29, pp. 138-150.

[158] De Boer, R., 2012, Theory of porous media: highlights in historical development and current state, Springer Science & Business Media.

[159] Stracuzzi, A., Mazza, E., and Ehret, A., 2018, "Chemomechanical models for soft tissues based on the reconciliation of porous media and swelling polymer theories," ZAMM-Journal of Applied Mathematics and Mechanics/Zeitschrift für Angewandte Mathematik und Mechanik, 98(12), pp. 2135-2154.

[160] Wang, R., and Sarntinoranont, M., 2019, "Biphasic analysis of rat brain slices under creep indentation shows nonlinear tension-compression behavior," Journal of the mechanical behavior of biomedical materials, 89, pp. 1-8.

[161] Verkman, A., 2013, "Diffusion in the extracellular space in brain and tumors," Physical biology, 10(4), p. 045003.

[162] Tully, B., and Ventikos, Y., 2011, "Cerebral water transport using multiple-network poroelastic theory: application to normal pressure hydrocephalus," Journal of Fluid Mechanics, 667, pp. 188-215.

[163] Schrot, R. J., and Muizelaar, J. P., 2002, "Mannitol in acute traumatic brain injury," The Lancet, 359(9318), pp. 1633-1634.

[164] Eisenträger, A., and Sobey, I., 2012, "Finite element simulation of a poroelastic model of the CSF system in the human brain during an infusion test," Oxford University, UK.

[165] Li, X., von Holst, H., and Kleiven, S., 2013, "Influences of brain tissue poroelastic constants on intracranial pressure (ICP) during constant-rate infusion," Computer methods in biomechanics and biomedical engineering, 16(12), pp. 1330-1343.

[166] García, J. J., and Smith, J. H., 2009, "A biphasic hyperelastic model for the analysis of fluid and mass transport in brain tissue," Annals of biomedical engineering, 37(2), p. 375.

[167] Wagner, A., and Ehlers, W., 2014, "On the multi-component modelling of human brain tissue to survey clinical interventions," PAMM, 14(1), pp. 125-126.

[168] Miga, M. I., Paulsen, K. D., Hoopes, P. J., Kennedy, F. E., Hartov, A., and Roberts, D. W., 2000, "In vivo modeling of interstitial pressure in the brain under surgical load using finite elements," Journal of biomechanical engineering, 122(4), pp. 354-363.

[169] Roose, T., Netti, P. A., Munn, L. L., Boucher, Y., and Jain, R. K., 2003, "Solid stress generated by spheroid growth estimated using a linear poroelasticity model☆," Microvascular research, 66(3), pp. 204-212.

[170] Helmig, R., 1997, Multiphase flow and transport processes in the subsurface: a contribution to the modeling of hydrosystems, Springer-Verlag.

[171] Pattison, A. J., McGarry, M., Weaver, J. B., and Paulsen, K. D., 2014, "Spatially-resolved hydraulic conductivity estimation via poroelastic magnetic resonance elastography," IEEE transactions on medical imaging, 33(6), pp. 1373-1380.

[172] Mow, V. C., Kuei, S., Lai, W. M., and Armstrong, C. G., 1980, "Biphasic creep and stress relaxation of articular cartilage in compression: theory and experiments," Journal of biomechanical engineering, 102(1), pp. 73-84.

[173] Ateshian, G. A., 2017, "Mixture theory for modeling biological tissues: illustrations from articular cartilage," Biomechanics: Trends in Modeling and Simulation, Springer, pp. 1-51.

[174] Holzapfel, G. A., and Ogden, R. W., 2017, Biomechanics: trends in modeling and simulation, Springer.

[175] Nagashima, T., Tamaki, N., Matsumoto, S., Horwitz, B., and Seguchi, Y., 1987, "Biomechanics of hydrocephalus: a new theoretical model," Neurosurgery, 21(6), pp. 898-904.

[176] Kaczmarek, M., Subramaniam, R. P., and Neff, S. R., 1997, "The hydromechanics of hydrocephalus: steady-state solutions for cylindrical geometry," Bulletin of mathematical biology, 59(2), pp. 295-323.

[177] Shojaeiarani, J., Hosseini-Farid, M., and Bajwa, D., 2019, "Modeling and Experimental Verification of Nonlinear Behavior of Cellulose Nanocrystals Reinforced Poly (Lactic Acid) Composites," Mechanics of Materials, 135, pp. 77-87.

[178] Voyiadjis, G. Z., and Samadi-Dooki, A., 2018, "Hyperelastic modeling of the human brain tissue: Effects of no-slip boundary condition and compressibility on the uniaxial deformation," Journal of the mechanical behavior of biomedical materials, 83, pp. 63-78.

[179] Shojaeiarani, J., Bajwa, D., and Shirzadifar, A., 2019, "A review on cellulose nanocrystals as promising biocompounds for the synthesis of nanocomposite hydrogels," Carbohydrate polymers.

[180] Shojaeiarani, J., Bajwa, D. S., and Bajwa, S. G., 2019, "Properties of Densified Solid Biofuels in Relation to Chemical Composition, Moisture Content, and Bulk Density of the Biomass," BioResources, 14(2), pp. 4996-5015.

[181] Shojaeiarani, J., Bajwa, D. S., Stark, N. M., and Bajwa, S. G., 2019, "Rheological properties of cellulose nanocrystals engineered polylactic acid nanocomposites," Composites Part B: Engineering, 161, pp. 483-489.

[182] Madireddy, S., Sista, B., and Vemaganti, K., 2016, "Bayesian calibration of hyperelastic constitutive models of soft tissue," Journal of the mechanical behavior of biomedical materials, 59, pp. 108-127.

[183] Shojaeiarani, J., Bajwa, D. S., and Hartman, K., 2019, "Mechanical Techniques for Enhanced Dispersion of Cellulose Nanocrystals in Polymer Matrices," Sustainable Polymer Composites and Nanocomposites, Springer, pp. 437-449.

[184] Syková, E., and Nicholson, C., 2008, "Diffusion in brain extracellular space," Physiological reviews, 88(4), pp. 1277-1340.

[185] Haslach Jr, H. W., Leahy, L. N., and Hsieh, A. H., 2015, "Transient solid–fluid interactions in rat brain tissue under combined translational shear and fixed compression," Journal of the mechanical behavior of biomedical materials, 48, pp. 12-27.

[186] Ehlers, W., and Wagner, A., 2015, "Multi-component modelling of human brain tissue: a contribution to the constitutive and computational description of deformation, flow and diffusion processes with application to the invasive drug-delivery problem," Computer methods in biomechanics and biomedical engineering, 18(8), pp. 861-879.

[187] Tavner, A., Roy, T. D., Hor, K., Majimbi, M., Joldes, G., Wittek, A., Bunt, S., and Miller, K., 2016, "On the appropriateness of modelling brain parenchyma as a biphasic continuum," Journal of the mechanical behavior of biomedical materials, 61, pp. 511-518.

[188] McGarry, M., Johnson, C., Sutton, B., Georgiadis, J., Van Houten, E., Pattison, A., Weaver, J., and Paulsen, K., 2015, "Suitability of poroelastic and viscoelastic mechanical models for high and low frequency MR elastography," Medical physics, 42(2), pp. 947-957.

[189] Smillie, A., Sobey, I., and Molnar, Z., 2005, "A hydroelastic model of hydrocephalus," Journal of Fluid Mechanics, 539, pp. 417-443.

[190] Budday, S., Sommer, G., Holzapfel, G., Steinmann, P., and Kuhl, E., 2017, "Viscoelastic parameter identification of human brain tissue," Journal of the mechanical behavior of biomedical materials, 74, pp. 463-476.

[191] Budday, S., Sommer, G., Haybaeck, J., Steinmann, P., Holzapfel, G., and Kuhl, E., 2017, "Rheological characterization of human brain tissue," Acta biomaterialia, 60, pp. 315-329.

[192] Pawlikowski, M., 2014, "Non-linear approach in visco-hyperelastic constitutive modelling of polyurethane nanocomposite," Mechanics of Time-Dependent Materials, 18(1), pp. 1-20.

[193] Hosseini-Farid, M., Ramzanpour, M., Ziejewski, M., and Karami , G., 2019, "A compressible hyper-viscoelastic material constitutive model for human brain tissue and the

identification of its parameters," International Journal of Non-Linear Mechanics, 116, pp. 147-154.

[194] Rashki, M., Azarkish, H., Rostamian, M., and Bahrpeyma, A., 2019, "Classification correction of polynomial response surface methods for accurate reliability estimation," Structural Safety, 81, p. 101869.

[195] Abbasnia, R., Hosseinpour, F., Rostamian, M., and Ziaadiny, H., 2013, "Cyclic and monotonic behavior of FRP confined concrete rectangular prisms with different aspect ratios," Construction and Building Materials, 40, pp. 118-125.

[196] Rostamian, M., Hosseinpour, F., and Abdelnaby, A. E., "Effect of Seismic Retrofitting on the Behavior of RC Bridge Columns Subjected to Main Shock-Aftershock Sequences," Proc. Structures Congress 2017.

[197] Shayanfar, M., Rostamian, M., Ghanooni-Bagha, M., Tajban, A., and Nemati, S., 2018, "Evaluating the plasticity of concrete beam-column connections reinforced with FRP composite rebars," Engineering Solid Mechanics, 6(4), pp. 331-340.

[198] Omranian, E., Abdelnaby, A., Abdollahzadeh, G., Rostamian, M., and Hosseinpour, F., "Fragility Curve Development for the Seismic Vulnerability Assessment of Retrofitted RC Bridges under Mainshock-Aftershock Seismic Sequences," Proc. Proceedings of the structures congress.

[199] Rostamian, M., Abbasnia, R., Zakeri, J., and Amiri, G. G., 2011, "Investigation of stress-strain behavior of FRP confined concrete columns under compressive loading," Iran University of Science and Technology.

[200] Arab, H. G., Rashki, M., Rostamian, M., Ghavidel, A., Shahraki, H., and Keshtegar, B., 2018, "Refined first-order reliability method using cross-entropy optimization method," Engineering with Computers, pp. 1-13.

[201] Abdelnaby, A. E., and Rostamian, M., 2016, "Reliability Analysis of Steel Frames Under Earthquake Loading Using Meta-Models."